MAXIMIZING TERAHERTZ PULSE AMPLITUDE FROM LOW TEMPERATURE GALLIUM ARSENIDE PHOTO CONDUCTIVE SEMICONDUCTOR SWITCH

A Dissertation

Presented to

The Faculty of the Graduate School

University of Missouri-Columbia

In Partial Fulfillment

Of the Requirements for the Degree

Master of Science

By

SAMPAD RAY

Dr. Naz E. Islam, Master's Thesis Advisor

July 2011

The undersigned, appointed by the Dean of the Graduate School, University of Missouri Columbia, have examined the dissertation entitled

MAXIMIZING TERAHERTZ PULSE AMPLITUDE FROM LOW TEMPERATURE GALLIUM ARSENIDE PHOTO CONDUCTIVE SEMICONDUCTOR SWITCH

Presented by Sampad Ray
Candidate for the degree of Master of Science
And hereby certify that in their opinion it is worthy of acceptance

____
Professor Naz E. Islam

____
Professor Mahmoud Almasri

____
Professor John Fresen

ACKNOWLEDGEMENTS

The author would like to show his profound appreciation to the HiPER Lab Research Group of University of Missouri, Columbia. In addition, the author would hereby like to whole-heartedly thank his advisor, Dr. Naz Islam for providing excellent guidance throughout the course of this work. Speaking of guidance, the path up the exponential curve to greater knowledge is not an easy one to negotiate. The idea that motivates this work comes from Dr. Islam and his PCSS and Electromagnetic compatibility concept. The author greatly acknowledges Dr. Naz E. Islam for his ideas, creative suggestions and the device concept from which the model in this work was originally formulated. The author also highly merits Dr. Mahmoud Almasri and Dr. John Fresen for their through consideration of this document. The author would also like to express his deepest and most sincere gratitude towards his committee. To his colleagues, graduate students Mr. Yunki Lee, Mr. Zan Lu and Lt. Commander. Tantong Somask (Thailand Navy), the author would like to express his thanks for their help in setting up the lab and help solve problem with the Silvaco and CST Microwave simulation. To the author is thankful to his good friend Mr. Daniel Alden Smith for proof reading this thesis.

The author dedicates this work to his late mother Late Mrs. Archana Ray, father Mr. Ajit Kumar Ray and sister Mrs. Sanhita Chaudhury. The author likes to take special mention of his philosopher and guide Mr. Mihir Bhattacharya for his constant motivation. Without their love, support and sacrifices this work could not have been accomplished. The author thanks his parents for having a dream and assisting in achieving it.

TABLE OF CONTENTS

ACKNOWLEDGEMENTS ii
List of Figures v
List of Tables viii
ABSTRACT ix
CHAPTER 1 1
Introduction 1
Chapter 2 5
Literature Survey: GaAs PCSS and Microstrip Patch Antennas 5
Chapter 3 12
Background: PCSS and Antenna physics 12
3.1 Basic Semiconductor Equation Equations 12
3.2 Drift – Diffusion model: 13
3.3 Current Injections in Perfect Insulator: 15
3.4 Theory of Current Injection in Solids: 17
3.4.1 The trap free insulator with thermal free carriers: 17
3.4.2 Insulator with traps: 19
3.4.3 Shallow Traps: 21
3.4.4 Deep Traps: 23
3.6 Two carrier injection 25
3.7 Photoconductive Semiconductor Switch (PCSS) Theory 27
3.8 Basic Antenna Parameter 30
3.8.1 Radiation Pattern of an Antenna: 30
3.8.2 Lobes in Radiation Pattern: 32
3.8.3 Radiation Intensity: 33
3.8.4 Beam Width and Beam Efficiency: 35
3.8.5 Directivity: 36
3.8.6 Gain: 37
3.8.8 Bandwidth: 37
Chapter 4 38
Simulation of GaAs PCSS and Antenna 38
PART I Substrate Simulation Setup 38

4.1 Silvaco Simulation Suite: 38
4.2 Simulation Mesh Parameters: 42
4.3 Traps and Defects: 43
4.4 Recombination Model with Trap implementation: 46
4.5 Mobility Models: 47
4.6 CST Microwave Studio Simulation Setup: 50
4.7 Simulation Parameters used for this research: 50
4.8 Construction of the PCSS in Devedit: 50
4.9 Explanation of the code and the simulation parameters: 51
4.10 Setup for Patch Microstrip Antenna Design: 52
Chapter 5 59
Results and Discussion: 59
Generating a Current Source Antenna and Radiation Analysis 59
5.1 CURRENT SOURCE FOR ANTENNA: SILVACO PCSS SIMULATIONS 59
MICROWAVE STUDIO SIMULATIONS: Antenna Analysis 76
5.2 The Results for the Antenna Simulation 76
Chapter 6 93
6.1 Conclusion: 93
6.2 Discussion and Future work: 95
References: 96
Appendix: 99
Code for simulation of the photoconductive emitter 99

LIST OF FIGURES

Figure 1.1:	Basic concept of Antenna and how PCSS can work as an antenna…….	2
Figure 3.1:	IV Characteristic of a Shallow Trap……………………………………	23
Figure 3.2:	IV Characteristic of a Deep Level Trap………………………………...	25
Figure 3.3:	Schematic diagram showing midgap impurity levels in a semiconductor. The N_{tn} denotes the electron traps, N_{tp} denotes the hole traps and N_R denotes the recombination centers…………………..	26
Figure 3.4:	Illustration of a Photoconductive Semiconductor Switch (PCSS)……...	28
Figure 3.5:	The figure in the left shows the flat band diagram of LT-GaAs showing defect levels provide fast trapping of photo excited electrons and the figure to the right shows the THz generation using LT-GaAs PCSS…..	29
Figure 3.6:	The left diagram shows the antenna field pattern with the coordinate system, the right diagram shows the Antenna power pattern in polar coordinates (linear scale)……………………………………………….	31
Figure 3.7:	Lobes in radiation pattern………………………………………………	32
Figure 3.8:	The spherical coordinates in relation to the area (dA) of solid angle $d\Omega = sin\theta \; d\theta \; d\phi$…………………………………………………………	33
Figure 3.9:	Cross section of a symmetrical power pattern of an antenna showing equivalent solid angle for a cone-shaped triangular pattern……………	35
Figure 4.1:	The Atlas Inputs and Outputs…………………………………………...	40
Figure 4.2:	Mesh configuration of the designed PCSS……………………………..	43
Figure 4.3:	The acceptor and donor trap energy level in reference to conduction and valence band edges…………………………………………………	44
Figure 4.4:	Shows the design of the dual patch ACMSA with a rectangular aperture and its dimensions……………………………………………..	54
Figure 4.5:	Shows the design of the dual patch ACMSA with a circular aperture and its dimensions……………………………………………………	54
Figure 4.6:	Shows the design of the dual triangular patch ACMSA with a circular aperture and its dimensions……………………………………………..	55
Figure 4.7:	Shows the design of the dual semicircular patch ACMSA with a circular aperture and its dimensions…………………………………….	55
Figure 4.8:	Shows the units fixed for the simulation experiments………………….	56
Figure 4.9:	Showing the units chosen for the simulations…………………………..	56
Figure 4.10:	Showing the Background conditions used for the simulation of the antenna……………………………………………………………….....	57
Figure 4.11:	Showing the Frequency Range Settings………………..........................	57
Figure 4.12:	The input pulse fed to the antenna…………………………..................	58
Figure 5.1	Shows the I-V characteristics generated through bias increments (250 Volts, 500 Volts, 1100 Volts, and then finally to 1750 Volts)…………	60
Figure 5.2:	Shows the charge concentration in the LT PCSS at (a) 250 V, (b) 500 V, (c) 1100 V and (d) 1750V………………………………………..	62
Figure 5.3:	Showing the conduction current density at (a) 250 V, (b) 500V, (c) 1100 V and (d) 1750 V respectively throughout the LT GaAs PCSS….	63
Figure 5.4:	Showing the current flow lines at (a) 250 V, (b) 500V, (c) 1100 V and	

	(d) 1750 V respectively throughout the LT GaAs PCSS……………….	64
Figure 5.5:	Showing the Electric field across the LT-GaAs PCSS at (a) 250 V, (b) 500V, (c) 1100 V and (d) 1750 V respectively…………………………	65
Figure 5.6:	Showing the Donor Trap Ionized Density along the PCSS at (a) 250 V, (b) 500V, (c) 1100 V and (d) 1750 V respectively……………………..	66
Figure 5.7:	Shows the recombination rate at (a) 250 V, (b) 500V, (c) 1100 V and (d) 1750 V respectively throughout the LT-GaAs PCSS……………….	67
Figure 5.8:	The beam illuminated on the PCSS……………………………………	68
Figure 5.9:	The conduction current density of the LT-GaAs PCSS while the same is illuminated with a 50 MW/sq cm beam of wavelength 0.78 micrometers………………………………………………………………..	69
Figure 5.10:	Shows the donor trap density of the LT-GaAs PCSS while the same is illuminated with a 50 MW/sq cm beam of wavelength 0.78 micrometers………………………………………………………………..	70
Figure 5.11:	Shows the electric field across the LT-GaAs PCSS while the same is illuminated with a 50 MW/sq cm beam of wavelength 0.78 micrometers………………………………………………………………..	70
Figure 5.12:	Shows the current flow lines across the LT-GaAs PCSS while the same is illuminated with a 50 MW/sq cm beam of wavelength 0.78 micrometers………………………………………………………………..	71
Figure 5.13:	Showing the Photo generation rate across the LT-GaAs PCSS while the same is illuminated with a 50 MW/sq cm beam of wavelength 0.78 micrometers………………………………………………………………..	71
Figure 5.14:	Showing the Impact generation rate across the LT-GaAs PCSS while the same is illuminated with a 50 MW/sq cm beam of wavelength 0.78 micrometers………………………………………………………………..	72
Figure 5.15:	The current through the PCSS Vs the Transient time when the LT GaAs PCSS is subjected to 350 femtoseconds laser pulse……………..	73
Figure 5.16:	Available photocurrent generated throughout the experiment…………	73
Figure 5.17:	The rise time of the electrical pulse generated from the LT GaAs when subjected to 350 femtoseconds laser beam……………………………..	74
Figure 5.18a:	The pulse width of the generated pulse from the Photoconductive emitter when subjected to 0.78 micrometers wavelength laser beam under the bias voltage of 1100 V………………………………………	75
Figure 5.18b:	The Frequency domain signal of the generated photo current from PCSS………………………………………………………………………	76
Figure 5.19:	The S11 magnitude (dB) Vs the frequency (THz) for a dual patch rectangular ACMSA………………………………………………………..	77
Figure 5.20:	The Farfield Pattern for the dual patch rectangular ACMSA…………	78
Figure 5.21:	The Farfield directivity of the antenna…………………………………	79
Figure 5.22:	Farfield Gain for the antenna………………………………………..	80
Figure 5.23:	The Farfield Electric field for the antenna……………………………..	80
Figure 5.24:	The S11 magnitude (dB) Vs the Frequency (THz) response of the dual rectangular patch rectangular ACMS…………………………………	81
Figure 5.25:	Farfield plot for a rectangular Dipole Rectangular Aperture Coupled	

MSA…………………………………………………………………… 81
Figure 5.26: The Farfield directivity of the beam radiated from the ACMSA……… 82
Figure 5.27: The Farfield Gain for the ACMSA at 2.53 THz……………………… 83
Figure 5.28: The Electric field of the ACMSA at 2.53 THz………………………… 83
Figure 5.29: S11 Parameter in dB Vs the Frequency for a rectangular Dipole Circular Aperture Coupled MSA………………………………… 84
Figure 5.30: Farfield plot for a rectangular Dipole Circular Aperture Coupled MSA. 84
Figure 5.31: Directivity plot for a rectangular Dipole Circular Aperture Coupled MSA…………………………………………………………………. 85
Figure 5.32: Gain plot for a rectangular Dipole Circular Aperture Coupled MSA….. 86
Figure 5.33: E-field plot for a rectangular Dipole Circular Aperture Coupled MSA. 86
Figure 5.34: The S11 parameter in dB for dual triangular patches circular ACMSA. 87
Figure 5.35: The Farfield Pattern for the triangular patch dipole circular ACMSA at 6.4311 THz……………………………………………………………... 87
Figure 5.36: The directivity of triangular patch circular ACMSA at 6.4311 THz…... 88
Figure 5.37: The farfield gain of the triangular patch circular ACMSA at 6.4311 THz………………………………………………………………….. 88
Figure 5.38: The Electric field for the triangular patch circular ACMSA at 6.4311 THz………………………………………………………………….. 89
Figure 5.39: The S11 (dB) vs. frequency (THz) for the semicircular patch circular ACMSA…………………………………………………………….. 90
Figure 5.40: The farfield pattern of the semicircular patch circular ACMSA at 6.4311 THz……………………………………………………………... 90
Figure 5.41: The farfield directivity for the semicircular patch circular ACMSA at 6.4311 THz……………………………………………………………... 91
Figure 5.42: The farfield gain for the semicircular patch circular ACMSA at 6.4311 THz………………………………………………………………….. 92
Figure 5.43: Electric field for the semicircular patch circular ACMSA at 6.4311 THz……………………………………………………………… 92

LIST OF TABLES

Table 2.1: Free electron lifetime and mobility in LT GaAs for different growth temperatures……………………………………………………………… 6
Table 4.1: The Substrate condition of the GaAs used for antenna design………... 53
Table 4.2: The patch material parameters used for antenna design…………….…. 53

ABSTRACT

An antenna radiates when a time rate of change of signal arrives at the structure from a generator, after travelling through a transmitting medium. THz radiation in a photoconductive semiconductor switches (PCSS) follows the same principles. Here the signal is produced by the photoconductive action, which travels through the bulk to the metallic contacts. In the simulation analysis, therefore, one needs to analyze the substrate with semiconductor code to characterize the generated pulse and then use Maxwell's equation solver for the antenna (contact) analysis. This is because of the unavailability of a comprehensive simulation code that can solve both Maxwell's and semiconductor equations in tandem. In this study, two different commercially available simulation codes were used to optimize the THZ radiation from a GaAs PCSS.

Results show that the 50 X 50 μm PCSS material produces a central frequency of 1.75 Terahertz, and a pulse amplitude of approximately 0.22 A at an optimum bias voltage of 1100 Volts. The PCSS was illuminated for 350 fs with a 0.78 μm beam, 50 Mw/cm^2 in intensity. The FWHM of the generated pulse 0.4 ps, and the rise time is 0.275 ps.

In the antenna analysis, results show that the rectangular patch antenna had a maximum return loss (S11) of approximately -30 dB and had multiple resonant frequencies. The maximum S11 was achieved at 5.6845 THz. The directivity of the main

lobe was found out to be 6.2 dB with an angular width of 36.9 degrees. The main lobe was directed at 148 degrees. The side lobes were found out to be -6.8 dB.

CHAPTER 1
Introduction

The current through a thin conductor can be written as [1]:

$$I = \rho_l v \quad (1.1)$$

Differentiating the equation 1.1 with respect to t, the equation stands as:

$$\frac{dI}{dt} = \rho_l \frac{dv}{dt} \quad (1.2)$$

$$\frac{dI}{dt} = \rho_l a \quad (1.3)$$

Where, I = the current through the conductor or the transmission line.

ρ_l = the charge density in the conductor or transmission line of length l

v = the velocity of the charge

a = the acceleration of the charge.

Equation no. 1.3 defines the basic conditions for radiation. A rate change in the current in a conductor or an acceleration or deceleration of the charges flowing in the conductor results in EM radiation. Thus technically speaking every conducting structure can radiate. An antenna is preferred structure due the fact that it can radiate in a specified direction and the radiating power can be manipulating by changing the structures shape etc., with specific gain and radiation pattern. An antenna has basically three components, they are:

- A source: This generates the signal to be transmitted.

- A Transmission Line: The transmission line carries or feed the signal from the source to the antenna.
- And the radiating antenna: This converts the signal form electrical pulse to electromagnetic waves and radiates the same to the space and vice versa.

A photoconductive semiconductor switch (PCSS) is an integral part of pulsed power electrical and electronic systems. Recently PCSSs, specifically GaAs based PCSSs, both low temperature (LT) grown and the semi-insulating (SI) type have been used in the generation of THz radiation. Radiation occurs when the carriers generated in the substrate are accelerated towards the contacts, which results in radiation (Figure 1.1). The contacts or the antenna in this case may be different types and thus the contact shapes may vary.

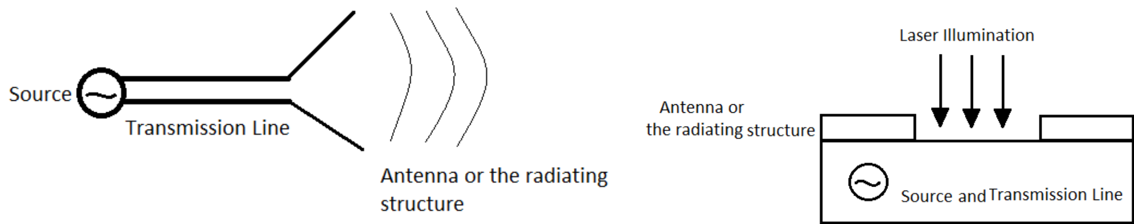

Figure 1.1: Basic concept of Antenna and how PCSS can work as an antenna

The objective of this research is to characterize both the PCSS and the antenna and to establish a link between the pulse shape and the radiation pattern of the antenna. Also, there is a need to establish a link between the THz radiation and the substrate conditions that leads to THz generation. Specifically the carrier parameters such as mobility, recombination rate, photo generation rate and impact ionization, conduction current density and E-field needs to be characterized. For the antenna the objective is to design a shape for optimum directivity, gain and power.

The first part of this research effort is directed towards the development of a photoconductive semiconductor switch that can satisfy the design criterion of optimum THz radiation. The photoconductive property enables the optical generation of an ultrafast electric pulse and subsequently emitted or radiated by the integrated devices realized in microstrip and coplanar technology. Due to the generation of very fast output pulses which is usually less than 100 picoseconds, the emitter device or the patch antenna can operate in Terahertz regime.

In this research it has been reported that a PCSS with a LT-GaAs substrate can also be used as the substrate for the antenna. As shown in the above given Figure1.1, the LT-GaAs substrate acts as the source and transmission line of the antenna. The metallic contacts acts as the radiating patches for the antenna. This research uses the above given concept to design the antenna and simulate the same for the best results. For the simulation there is no particular software that can simulate the generation of the photoconductive current in the PCSS and at the same time can also simulate the radiating pattern for the device. For this research two commercially available simulation suits have been used to simulate the device. The first part of the research focuses on the generation of the photoconductive current which is later used as the input signal to the antenna. The second part of the research is that several microstrip antennas with different parameters and geometry were being designed to investigate the radiation pattern, the gain, and the directivity of the radiating structures.

The rest of the thesis is divided as follows:

- Chapter 2 presents the literature survey, where the performance of a working GaAs PCSS is summarized with a brief introduction of semi insulating materials.

Various parameters of a patch antenna and work about the same are also discussed in this chapter. Different kind of patch antennas using this kind of technology is also being reported.

- A brief survey of antenna analysis is also presented in this chapter.
- Chapter 3 briefly explains the fundamental operation and the parametric evaluation of a PCSS along with the different types of available PCSS and the theory based on much earlier work by Zutavern and Rosen et al [2]explaining the fundamentals of current injection in solids. The advantages of using GaAs materials are also discussed here. It also explains the importance of material characterization using different approaches and preliminary switch simulation data that includes the effect of Fermi level on material response.
- Chapter 3: presents the experimental setup and the transient response for a very high bias and its use in electromagnetic radiation. This provides insight in predicting high voltage switch behavior of the PCSS, far field pattern, directivity, gain, and etc of the antenna.
- This is followed by result in Chapter 5, and conclusions and a discussion of future work in Chapter 6.

The appendix will have the simulation code that is being used to design and simulate the PCSS.

CHAPTER 2

Literature Survey: GaAs PCSS and Microstrip Patch Antennas

Interest is photoconductive switches developed in the 70' when there was a need for fast, high power compact switches to be used in space vehicles. Some of the advantages of these switches, besides small size and low cost include low impedance, low jitters and fast switching action. A number of researches have contributed to the development of PNSS technology. G. M. Loubriel [2] worked on the longevity of high gain GaAs photoconductive semiconductor switches (PCSS) for pulsed power applications. He extended the lifetime of the PCSS to well over 10 million pulses. He has done so by reducing the density of carriers at the semiconductor to metal interface. He reduced the density in the vertical and lateral directions. Zutavern [3] developed fiber optically controlled PCSS for high voltage switches in pulsed power application. H. P. Hjalmarson [4] explained the lock-on phenomenon of the high-power optically triggers PCSS with respect to impact ionization. The photoconductive phenomenon and the generation of THz frequency can be achieved using a PCSS. The THz frequency generation depends on the material and the parameters of the PCSS. Among the material characteristics the presence of arsenic anti-sites and the Gallium vacancies are significantly responsible for the production of THz frequency. These defects in the GaAs are responsible for producing the traps in the semiconductor material. When the PCSS is subjected to very high bias voltage, it enables the electrons to move from valence band to

the conduction band. Due to these presences of traps and the very low carrier life time in the range of 10^{-16} seconds enables the carriers fall into the trap and not be a part of the conduction current. However, as long as the carriers remain in the trap sites, they may still participate in the screening of the electric field in a PCSS. The electrical influence due to these thermally generated carriers is lost as soon as the electron and holes recombine. Gregor Segschneider [5], reported that for low temperature GaAs, the decay of conductivity and the carrier density slows down with rising excitation density. It can be observed from the experiments conducted by Nemec et al. [6] that the mobility of the carriers decreases with the increase in annealing temperatures, which results in an increase of the carrier life time [6].

$T_g(^{\bullet}C)$	$LT_{\tau_c}\,(fs)$	$\mu\,(cm^2/V.\mathrm{sec})$
250	660 ± 50	2250 ± 100
225	450 ± 50	2350 ± 100
200	375 ± 50	3000 ± 100
175	280 ± 50	...

Table 2.1: Free electron lifetime and mobility in LT GaAs for different growth temperatures [6].

Dr. Naz Islam et al. did a considerable research work in achieving a higher hold-off voltage in the PCSS. One of the major reasons for premature breakdown is accredited to the change in the material properties while the device is operational at very high bias voltages. Moreover, the inhomogeneous nature of the device material affects the switching conditions of the PCSS beyond a certain voltage. There is a n^+ layer near the cathode region. The spacing between the Anode edge and the n^+ layer is 0.25 cm. From the graph in the above given Figure 2.1 it can be inferred that the traps are filled prior to

the breakdown voltage which is at 34 kV. This phenomenon affects the switching of the device beyond a certain voltage. The trap filled regions are initially formed near the cathode and slowly approaches towards the anode region as the bias voltage increases, which in turn interferes with the conduction mechanism in the switch. Thus the most common way of improving the device hold-off characteristics is by drifting the formation of the trap filled regions to a higher bias voltage. It is achieved by using the mechanisms that would suppress the injection of electrons until a higher voltage bias which in this case is 34 kV is reached. Dr. Islam showed that with a n^{+} region near the cathode showed significant improvements in the operating voltage of an opposed contact DDSA type switch. The reason for these marked improvements in the operating voltage is attributed to the interaction between the GaAs substrate and the n^{+} doped region adjacent to it. More details are given in the reference papers [7-9]. This region acts a diode which adds the cut-off voltage for the diode to the hold-off voltage thus increasing its overall voltage carrying capability. The n^{+} region is doped with the doping profile if $1\, X\, 10^{18}\ /cm^{3}$ over an area of 20 μm by 200 μm. This region has basically two very important effects on the conduction mechanism of the switch, they are:

1) This region shifts the high E field region from the contact to a region near to the diffused n^{+} layer.
2) This region helps to lower the high E field near the contact.

This n^{+} - SI GaAs also inhibits electron injection until a higher voltage bias is reached.

N. E. Yu [10] reports the generation of tunable and narrow-band of frequency approximately l~3 THz, by using periodically poled materials. This is achieved by using femtosecond laser pulses on a periodically poled lithium niobate (PPLN) and periodically

poled stoichiometric lithium tantalate (PPSLT) crystal. Xu Ming [11] reported the generation of THz with photoconductive dipole antenna based on semi-insulating GaAs. They were able to generate THz waveform with about 1 picosecond width. They also reported a frequency spectrum of the THz radiation range over 1 THz and their peaks are roughly at 0.3 THz. N. E. Yu[12] demonstrated THz generations in periodically poled lithium niobate and lithium Tantalate crystals. The THz generated was in the range of 1-2 THz. They also reported the generation of different backward and forward THz radiation in periodically poled structures via difference frequency generation within the ultra broad pump laser. The THz pulse which is being generated can be controlled by the quasi-phase matching structures. Xu Jingzhao [13] reported that a coating of Si_3N_4 on GaAs antenna enhances the THz wave generation by enhancing the breakdown voltage. He also reported that breakdown field can be increased by additionally coating the antenna by a Silicon gel. He also stated that the THz radiated power can be increased by an order of one when the GaAs antenna has multiple transparent dielectrics coating and sealing. Dae Sin Kim reported enhanced THz emission by spatially non uniform optical illumination by the combined effects of large trap enhanced fields near the anode in a semi-insulating photoconductor. They also distinguished the self consistently the screening contribution to the THz radiation associated with the Coulomb and radiation field. To analyze this they used the three dimensional Maxwell equation in the solver. The reported that by reduction of the impact of the screening effects an enhanced THz radiation can be obtained. The screening effects are main underlying factor for the saturation of the THz radiation power, R. A. Lewis [14] reported that ultra-short near field radar pulses are capable of generating THz radiation. Lu Bic [15] reports the construction of the

photoconductive antenna producing THz radiation. The photoconductive emitters were made of LT-GaAs layer annealed at different temperatures. The photoconductive emitter was subjected to a femto-second Yb: KGW laser .The photoconductive emitter produced a spectral bandwidth of 3 THz and its dynamical range exceeded 50 dB. Park San-Gyu reported the construction of a large aperture biased photoconductive emitters that can generate narrow-band, high power THz radiation. The photoconductive emitters avoid saturation when the fluence excitation is very high. There is a very strong dependence of the THz generation on the carrier lifetime. As the carrier lifetime decreases, the higher is the magnitude of THz radiation. As the carriers are generated in the semiconductor it falls into the trap and recombines very quickly thus having participated in the conduction mechanism for a very short period of time. Thus we can see a pulse width of nearly .35 femtoseconds to 100 femtoseconds. M. Jarrahi [16] demonstrated the generation of a narrow band THz radiation by superposing the time delayed wide-band radiation by forming an array of sub-picosecond photoconductive antennas. They employed optical pulses from Ti: Sapphire mode-locked laser to generate the THz radiation. The laser provided a pulse of width 160 femtoseconds with 780 mW of average power and 76 MHz of repetition rate. The wavelength of the lock mode laser was 850 nm. This beam with the above given parameters generates a very high density of carriers in the LT-GaAs emitter. The wavelength of the laser thus needs to less than 0.89 micrometers. This generation of high density of carriers produces high electric field near the contacts of the electrodes where they are captured. Thus it can be inferred that for better radiation from the antenna high electric field near the contacts is very essential. Moreover, for better radiation it also required to keep the metallic contacts on the same plane.

Turan Q Tran et al. [17] worked on reconfigurable radiation patterns in an antenna. He reported that multimode microstrip patch antenna has the capability to offer reconfigurable radiation patterns. Circular microstrip patch antennas is used to generate different modes of radiation on a substrate material [18]. He reported the use of a combination of coaxial probes to generate higher order modes. To isolate the modes on the patch circular slits had to be created in the patch.

It is being reported by K. R. Jha [19], that a photonic substrate can be used to enhance the gain and the radiation efficiency of the microstrip antenna. It is being also reported that antenna he designed can operate at 600 GHz and the gain and radiation efficiency of the antenna is about 13dB and 83.02%, respectively. The antenna also resonates at 575 GHz and 741 GHz. He also reported that by periodic implantation of air gaps in the dielectric slab of the host photonic substrate it is possible to radiate in Terahertz regime [20]. He also reported that the antenna can radiate at 600 GHz and has a return loss of nearly -70 dB. J. Cunningham reported the application of on-chip integrated terahertz system [21]. He reported that a photoconductive material was used to generate the Terahertz radiation guided through a planar waveguide. The radiated wave was detected coherently by photoconductive detection. With the advent of this technology it is possible to investigate images in smaller sample volumes. S. G. Kong et al. [22]reported that Terahertz spectroscopy demonstrates the potential for explosive detection through unique absorption spectra pattern. The Terahertz waves show good penetration through many dielectric materials that are visually opaque. Pickwell-MacPherson et al. [23] were able to detect between diseased and healthy tissue in ex vivo studies using Terahertz Spectroscopy. They calculated the optical terahertz properties of breast tissues using

terahertz time domain spectroscopy. This method uniquely identifies between the healthy tissues and the carcinogenic tissues. Liangliang Zhan [24] reported polarization sensitive terahertz detection method which can measure both orthogonal components of the terahertz electric field. Polarized terahertz transmission spectroscopy shows that birefringence can result in transmission minima. M. Natftaly [25] reports the use of Terahertz Time Domain Spectroscopy for determining the properties of nonpolar amorphous materials. V. N. Truchin et al. [26], reported the radiation phenomenon in non-equilibrium e-h plasma excited in the photo-conductive gap of terahertz radiating antenna by an ultra-short laser pulse. It is being reported that the revealed properties of generated terahertz pulse crucially dependent on the physics of dissipation mechanisms or the compensation mechanism of the substrate used, the ratio of terahertz radiation formation length and sample size, current configurations and relative traveling velocities of e-h plasma bunch and terahertz radiation pulse generated by the photoconductive substrate. It is also reported by Truchin that semiconductor slab also radiates in backward direction. This is due to the material parameters of the substrate which also enables the radiation of twin Terahertz electromagnetic pulses.

Thus it can be summarized that it is possible to generate THz radiation from a LT-GaAs substrate. It is also possible to radiate the THz generated signal or the electrical pulse through the metallic contacts on the device. Thus the generation of THz and subsequently radiating the same is of prime importance.

CHAPTER 3
Background: PCSS and Antenna physics

In order to understand the conductivity mechanisms of a semi insulating (SI) materials used in PCSSs, we need to first understand current transport in semiconductors and in semi-insulating semiconductors as well. Charge transport in semi-conductors are detailed in text books [21], so will be described very briefly here which will be followed by discussions on the mechanisms of current injection in semi-insulators. In the latter part of this chapter includes a brief discussion of important antenna parameters.

3.1 Basic Semiconductor Equation Equations

Charge transport in semiconductors are governed by the physics associated with the movement or accumulation of carriers (electrons and holes) as they move through diffusion or under the influence of an electric that field due to potential from charge accumulation or bias on the terminals. The variation in electrostatic potentials to the carrier density is governed by the Poisson's equation given as [27],

$$div(\varepsilon \nabla \psi) = -\rho \qquad (3.1)$$

Where, ψ = the electrostatic potential, ε = the local permittivity of the semiconductor substrate, ρ = the local space charge density,

The local space charge density is the combination of the donations from all mobile and fixed charges which includes electrons, hole and ionized impurities.

The electric field $\vec{E}$ is determined from the potential using the equation,

$$\vec{E} = -\nabla\psi \tag{3.2}$$

The continuity equations for electrons and holes are given as,

$$\frac{\partial n}{\partial t} = \frac{1}{q}\, div\overrightarrow{J_n} + G_n - R_n \tag{3.3}$$

$$\frac{\partial p}{\partial t} = \frac{1}{q}\, div\overrightarrow{J_p} + G_p - R_p \tag{3.4}$$

Where, n, p = the electron and hole concentration respectively, $\overrightarrow{J_n}$ = the electron current densities, $\overrightarrow{J_n}$ = the hole current densities, G_n = the electron generation rate, G_n = the hole generation rate, R_p = the recombination rate of holes, R_n = the recombination rate of the electrons, q = the charge of an electron.

3.2 Drift – Diffusion model:

The Drift – Diffusion [27] model is the simplest model for charge transport in semiconductors, which expresses the current densities in the terms of Fermi Level, as shown here:

$$\overrightarrow{J_n} = -q\mu_n n\nabla\phi_n \tag{3.5}$$

$$\overrightarrow{J_p} = -q\mu_p n\nabla\phi_p \tag{3.6}$$

Where, μ_n = the electron mobility,

μ_n = the hole mobility,

ϕ_n = the electron quasi-Fermi level,

ϕ_p = the hole quasi-Fermi Level.

The quasi-Fermi Levels occur as a result of bias across the device when current injections occur, It is a dependent function of carrier concentration and potential as shown below,

$$n = n_{ie} \exp\left[\frac{q(\psi - \phi_n)}{kT_L}\right] \tag{3.7}$$

$$\phi_n = \psi - \frac{kT_L}{q} \ln\left(\frac{n}{n_{ie}}\right) \tag{3.8}$$

$$p = n_{ie} \exp\left[\frac{-q(\psi - \phi_p)}{kT_L}\right] \tag{3.9}$$

$$\phi_p = \psi - \frac{kT_L}{q} \ln\left(\frac{p}{n_{ie}}\right) \tag{3.10}$$

Where, n_{ie} = the effective intrinsic concentration, T_L = the lattice temperature.

By substituting these equations into the current density expressions, the following adapted current relationships are obtained:

$$\overrightarrow{J_n} = qD_n \nabla n - qn\mu_n \nabla\psi - \mu_n n(kT_L \nabla(\ln n_{ie})) \tag{3.11}$$

$$\overrightarrow{J_n} = qn\mu_n \overrightarrow{E_n} - qD_n \nabla n \tag{3.12}$$

$$\overrightarrow{J_p} = -qD_p \nabla p - p\mu_p \nabla\psi - \mu_p p(kT_L \nabla(\ln n_{ie})) \tag{3.13}$$

$$\overrightarrow{J_p} = p\mu_p \overrightarrow{E_p} - qD_p \nabla p \tag{3.14}$$

Where, D_n = the electron diffusivity, D_p = the hole diffusivity.

The last terms of equations (3.11) and (3.13) accounts for the gradient in the effective intrinsic carrier concentration.

3.3 Current Injections in Perfect Insulator:

In order to understand the physics of charge transport in semi-insulating materials such as the GaAs PCSS, a background to charge conduction in perfect insulators is necessary. A perfect insulator is a material which exhibits no current flow even at very high bias. A perfect insulator is devoid of any traps with negligible concentration of free carriers at thermal equilibrium. Since the process of diffusion is a more prominent activity near the electrodes or the contacts thus it is possible to neglect the diffusive current though the bulk material. Thus neglecting these current does not affect the bulk properties in the insulator. The equation for the current density as:

$$J = \rho v = \frac{Q}{t} \tag{3.15}$$

Where, J = current density, ρ = the average injected free charge concentration,

v = the average drift velocity of the free electrons,

Q = the total injected free charge per unit area between the cathode and the anode,

t = the transit time of a free electron between the cathode and the anode.

The parameters, v and t, and ρ and Q are related by the equations (3.16) and (3.17) given below:

$$t = \frac{L}{v} \tag{3.16}$$

$$Q = \rho L \tag{3.17}$$

Where, L = the distance between the anode and cathode.

From electrostatics we know that the total charge Q_0 per unit area on the plate of a parallel plate condenser is proportional to the voltage V across the condenser and is given by the below equation:

$$Q_0 = C_0 V \tag{3.18}$$

$$C_0 = \frac{\epsilon}{L} \tag{3.19}$$

Where, Q_0 = the total charge per unit area, C_0 = the capacitance of the parallel plate capacitor, V = the voltage applied across the parallel plate capacitor, ε = the static dielectric constant of the medium between the plates, L = the spacing between the plates. Now, substituting for Q from equation (3.17) into (3.15), we get

$$J = \frac{C_0 V}{t} \tag{3.20}$$

And substituting for C_0 from (3.15) into (3.16), we get:

$$J = \frac{\epsilon}{L} \cdot \frac{V}{t} \tag{3.21}$$

Now, substituting the value of "t" from (3.12) we get

$$J = \frac{\epsilon}{L} \cdot \frac{V}{\frac{L}{v}} = \frac{\epsilon v V}{L^2} \tag{3.22}$$

The drift velocity of the electrons in the conduction band of the solid is marked by the frequent collisions with the electrons or carriers generated by the thermal vibrations, the impurities and structural defects in the semiconductor material. For low fields, the electron drift velocity is proportional to the applied electric field across the switch, thus it can be written that:

$$v = \mu E = \mu \left(\frac{V}{L}\right) \tag{3.23}$$

$$t = \frac{L^2}{\mu v} \tag{3.24}$$

Where, μ = the drift mobility of free electrons, E = the average electric field intensity.

From (3.20) and (3.21) we get,

$$J \cong \epsilon\mu\left(\frac{V^2}{L^3}\right) \tag{3.25}$$

This particular phenomenon is the border line form for current voltage characteristics.

<u>3.4 Theory of Current Injection in Solids:</u>

M. A. Lampert discusses the technique called Space Charge Limited Current Injection in Solids in details. Injection currents due to the excess generated carriers in an insulator are a powerful probe in the study of insulators. Here, the excess generated carriers in the insulator are being used to extract information about the various types of defect states in the forbidden gap. The current voltage (I-V) characteristics are being used to determine the defect state in the semiconductor or the insulator material. It is also being used to determine the location of the defect sites with respect to the band edges. The topic Current Injection into an insulator is used to understand the theory of current injection into the semiconductor material. It also emphasizes and develops the theory on the introduction of defect states in the material. We will also look into the effects of two types of carrier injection into the semiconductor material.

<u>3.4.1 The trap free insulator with thermal free carriers:</u>

This section includes a little bit more complexity by introducing the concept of thermally free carriers with has the concentration of n_0, in the discussion of the insulators. Further studies have shown that there is a possibility of the existence of the

thermally free carriers such as electrons in the vicinity of the conduction band. There is this other possibility that the source of this electron is the set of donors lying very shallow in the band gap. These set of donors have a very small binding energy thus they are not effective as electron trap level. In this particular site, it can be highly assumed that the electrons are completely ionized at the room temperature.

At low applied voltage, it follows the Ohm's Law and the current density equation stands as:

$$J = en_0\mu\left(\frac{V}{L}\right) \tag{3.26}$$

We know that the injected charge is directly proportional to the voltage applied, thus as we increase the applied voltage the concentration of the injected charge also increases. Once the injected electron concentration (n_i) becomes nearly equal or comparable to the thermally generated free carrier concentration (n_0), the insulator starts deviating from the Ohm's law and starts following the trap free square law. The space charge limited current injection takes place at this cross over voltage.

The crossover voltage from Ohm's law to the trap free square law is given by:

$$V_X = \frac{en_0L^2}{\epsilon} = Q = C \tag{3.27}$$

Where, V_X = the crossover voltage from Ohm's Law to trap free square law.

On further manipulation of the above equation (3.27), the following forms of the equation are achieved:

$$t_X \cong t_\Omega \tag{3.28}$$

$$t_X = \left(\frac{L^2}{\mu V_X}\right) \tag{3.29}$$

$$t_\Omega = \left(\frac{\epsilon}{en_0\mu}\right) \tag{3.30}$$

Where, t_X = the electron transit time between the cathode and the anode at cross over voltage V_X.

t_Ω = the Ohmic or dielectric relaxation time.

Thus the above given equations (3.28), (3.29) and (3.30) claims that the injected excess electrons will dominate the thermally generated electrons. This will occur when the transit time for the excess electrons is too short for their charge to be relaxed by the thermal carriers.

3.4.2 Insulator with traps:

When an insulator is subjected to low voltages the current passing through the insulator is greatly reduces due to the existence of electron traps in the insulator material. Due to the presence of these electron traps in the insulator, this captures the injected electrons thus immobilizing the electrons to take part in the conduction process. However, the amount of excess charge that can be supported by an insulator at an applied voltage remains constant whether the charge is trapped or free.

Thus for a parallel plate condenser it is stated that at a given voltage, the amount of charge that can be stored on the plates of a parallel plate condenser is independent of the condition of weather the charge is free or immobilized in the surface states. Thus the equation no. 3.13 is rewritten as [28]:

$$Q = (\rho + \rho_t)L = C_0 V = \left(\frac{\epsilon}{L}\right) V \tag{3.31}$$

Where, ρ_t = the average injected trapped charge concentration.

The appropriate form of current voltage characteristics can be obtained by considering the relationship between the trapped and free electron concentrations in the semiconductor material. Thus, for non-degenerate semiconductors, the free electron concentration at thermal equilibrium can be determined by the equation no. 3.26 given below:

$$n_0 = N_c \exp\left[\frac{(F_0 - E_c)}{kT}\right] \tag{3.32}$$

Where, n_0 = the free electron concentration at thermal equilibrium.

F_0 = the thermodynamic Fermi Level.

N_c = the effective density of states in the conduction band.

E_c = the lowest energy level of the conduction band.

k = the Boltzmann's Constant.

T = the temperature in Kelvin.

Thus we can derive the concentration of the filled traps ($n_{t,0}$), which is given by the equation:

$$n_{t,0} = \frac{N_t}{1 + \left(\frac{1}{g}\right) \exp\left[\frac{(E_t - F_0)}{kT}\right]} \tag{3.33}$$

Where, N_t = concentration of the traps.

g = degeneracy factor for the traps.

The major disadvantage for the above given equation no. 3.27 is that, it does not consider the change in trap cross section with respect to the applied fields. The basic assumption for this equation is that the trap cross section remains constant throughout. Now, considering the fact that the semiconductor crystal is in thermal equilibrium, then

the balance between the free and the trapped electrons can be determined. Thus modifying the equation by considering the fact that the free electron concentration (n); can be achieved under the injection of free carriers rather than considering the free electron concentration at true thermal equilibrium (n_0). The corresponding Fermi level at which the free electron concentration can be achieved is called the Quasi Fermi Level. Thus we can write the below given equations:

$$n = n_i + n_0 = N_c \exp\left[\frac{(F - E_c)}{kT}\right] \tag{3.34}$$

$$n_t = n_{t,i} + n_{t,0} = \frac{N_t}{1 + \left(\frac{1}{g}\right)\exp\left[\frac{(E_t - F)}{kT}\right]} \tag{3.35}$$

Where, n_i = the average excess injected free electron concentration.

$n_{t,i}$ = the injected, excess trap electron concentration.

E_t = the energy level of the trap.

$n_{t,0}$ = the trap electron concentration at thermal equilibrium.

F = the Quasi Fermi Level.

n_t = the trap electron concentration.

3.4.3 Shallow Traps:

When the Quasi Fermi Level F lies below the electron trap energy level (E_t), then the electron trap at energy level (E_t) is said to be a shallow trap. Thus as per the definition we can write the below given equations:

$$\frac{E_t - F}{kT} > 1 \tag{3.36}$$

$$\frac{n}{n_t} = \frac{N_c}{gN_t}\exp\left(\frac{E_t - E_c}{kT}\right) = \theta \tag{3.37}$$

Where, θ = constant and is independent of the injection level, as long as the trap remains shallow

N_t = the shallow trap concentration.

It is being observed that the shallow trap concentration (N_t), considerably affects the space charge limited injection current if $\theta \ll 1$.

Thus equation no. 3.25 can be rewritten as:

$$Q = \rho_t L = \frac{\rho L}{\theta} = \left(\frac{\epsilon}{L}\right) V \tag{3.38}$$

Thus from the equation no. 3.11, 3.22 and 3.32 we can write that:

$$J = \theta \epsilon \mu \left(\frac{V^2}{L^3}\right) \tag{3.39}$$

Thus this particular equation has the effect of changing the slope of the current voltage characteristics.

The Fermi Level F keeps on rising with the increase in injection of the carriers, when the Fermi Level F is below the trap level which is in the case for the shallow traps. At some voltage V the Fermi Level will cross the trap level (E_t). This crossover of the Fermi Level will change the slope of the current voltage (IV) characteristics. This crossover of Fermi Level will enable the trap levels to be filled completely, and thus the injected charge will directly account for the increased current flow within the semiconductor. The voltage at which this crossover takes place is known as V_{TFL} and this phenomenon is called as the Trap Filling Limited (TFL) Law.

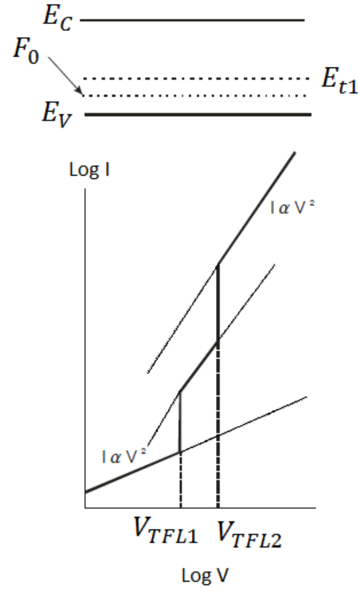

Figure 3.1: IV Characteristic of a Shallow Trap [16].

Thus from the equation no. 3.22 and 3.33, at the voltage crossover for a shallow trap case, we can rewrite the equation as:

$$V_X = \left(\frac{en_0L^2}{\theta\epsilon}\right) \tag{3.40}$$

Where e = the charge of an electron in Coulombs.

3.4.4 Deep Traps:

When the Quasi Fermi Level F lies below the electron trap energy level (E_t), then the electron trap at energy level (E_t) is said to be a deep trap. The deep tarp follows the particular condition given below in the equation:

$$\frac{E_t - F}{kT} < 1 \tag{3.41}$$

Considering thermal equilibrium, the number of traps occupied by holes is given by the equation:

$$p_{t,0} = N_t - n_{t,0} \cong \frac{N_t}{g} \exp\left(\frac{E_t - F_0}{kT}\right) \tag{3.42}$$

Where, $p_{t,0}$ = the trap density occupied by holes at thermal equilibrium.

As we discussed in the previous section about the shallow traps, it has been seen that until the thermally free carrier concentration (n_0), is higher than the injected free electron charge concentration (n_i), it is possible to apply Ohm's law for the current voltage characteristics. Once the injected free electron concentration increases and becomes comparable to the thermally free electron concentration, there will be an upward shift of the Quasi Fermi Level from the initial Fermi Level. Now as the concentration of the injected electron increases, the free electron concentration now stands as:

$$n = n_i + n_0 \tag{3.43}$$

Thus it can see from the above equation that the free electron concentration nearly doubles at the crossover point. Thus the Quasi Fermi Level shifts its location precisely by 0.7 kT. This motion is enough for the electrons for filling up the deep traps. The crossover voltage is then given by the below given equation:

$$V_X \cong \frac{Q_{TFL}}{C_0} \cong \frac{ep_{t,o}L^2}{\epsilon} \tag{3.44}$$

Where the subscript TFL = the Trap Filled Limited.

The behavior of the deep level tap is shown in the below given Figure 3.11:

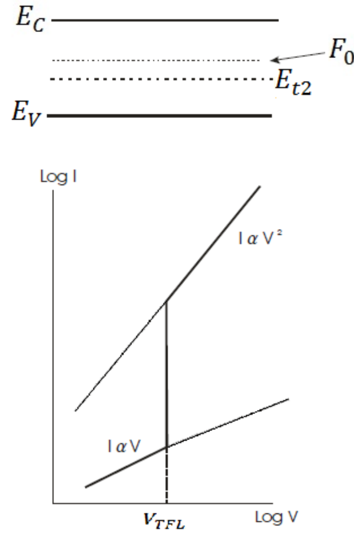

Figure 3.2: IV Characteristic of a Deep Level Trap [28].

In both the cases the IV Characteristics starts with obeying the Ohm's Law characteristics as shown in the equation no. 3.44. For the case of Deep Level Traps, the crossover voltage (V_X), is achieved when the thermally free carrier concentration (n_0), is equal to the injected free electron charge concentration (n_i). Then the IV characteristics coincide with the Trap Free Square Law as mentioned in equation no. 3.34.

For the case of the Shallow Traps, the current in the semiconductor follows the Square Law given in the equation no. 3.33, after it starts off with the Ohm's Law. Once the Fermi Level crosses the E_{t2} energy level, the V_{TFL2} characteristics merge with the Trap Free Square Law.

3.6 Two carrier injection

It is possible to achieve double injection of carriers in the semiconductor or insulator by designing the semiconductor device in such a way that the one of the contact to the semiconductor or insulator will inject holes in to the material and the other contact will inject electrons into the semiconductor or insulator material. Now, if the holes and

the electrons are injected at the same time, they can neutralize each other, but on the other hand the magnitude of the current by two carrier injection will be much higher than that of the single carrier current. But the downside of the two carrier injection is that the presence of both carriers of both polarities, which leads to a phenomenon called recombination. The carriers recombine in the semiconductor material before they complete their respective transit between the cathode and the anode [28].

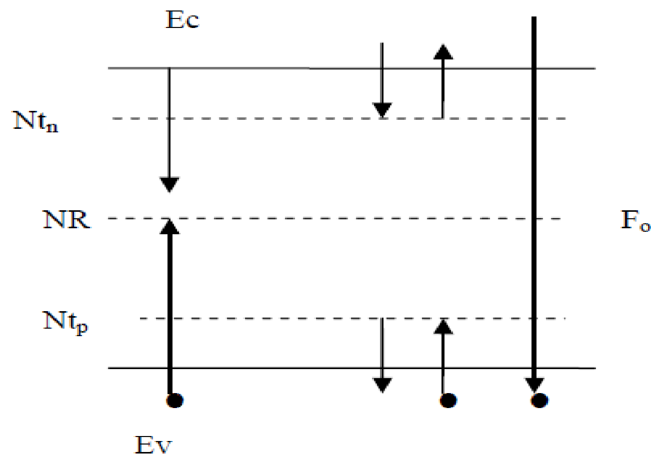

Figure 3.3: Schematic diagram showing midgap impurity levels in a semiconductor. The N_{tn} denotes the electron traps, N_{tp} denotes the hole traps and N_R denotes the recombination centers [8].

The recombination is basically a two step process which happens through a localized recombination center (N_R) as shown in the above given Figure 3.12. The first part of the process involves the capture of the electrons by the center and then it goes on to capture the hole. This process may also happen in opposite order i.e. the hole captured by the center first and then the electron is being captured. Due to the Kinetic Equilibrium requirement, at steady state the capture of electrons and the capture of holes by the corresponding recombination center are equal in nature. In the above given Figure 3.12 it can seen in the localized electron and hole traps. There could be a possibility of tri-

molecular recombination process which is also known as the Auger Recombination Process. The Auger Recombination usually happens at a relatively higher concentration than the usual one; the concentration usually is in the order of nearly $10^{18}\ /cm^3$. Thus for normally doped semiconductors the current analysis for Auger Recombination process is usually neglected. To determine the limitation of the current flow in an insulator, one must consider the two major factors which determines the same, they are:

(a) Recombination, or

(b) Charge Neutralization, or

(c) The effect of both the above factors.

To have a detailed understanding of the current flow in an insulator, the double injection of carriers in an insulator has to be studied.

3.7 Photoconductive Semiconductor Switch (PCSS) Theory

The mechanics of photoconductivity in SI material is as follows:

Basically the optically controlled semiconductor or photoconductive semiconductor (PCSS) switch connects a source to a load [29]. The PCSS consists of electrical contacts separated by normally semi-insulating or intrinsic semiconductors as shown in the right of the above Figure 3.4. As shown in the left of the Figure 3.4, the length of the semiconductor switch is given by h_s. The thickness of the semiconductor slab is given by t_s. The thickness t_s of the semiconductor switch is usually governed by the absorption depth, which is given by d_o and the practical fabrication requirements. The required operating voltage or the dielectric strength of the semiconductor determines the length of the switch or the distance between the electrical contacts, h_s, or electrodes. Parameters like the desired system inductance, the required current density, or the desired thermal resistance from the switch to the surrounding medium determines the width of

the semiconductor slab, w_s. The current density plays a very important factor in determining the width, w_s, of the switch such that there is no filamentary conduction, where a very small area carries a very large amount of current. As a result of which there might be formation of mesoplasma which can permanently damage the switch. The planer, insulating, photoconductive medium is changed into a conductor by illuminating the face of the switch with a uniform optical intensity source between the contacts. The photoconductive switch resistance is controlled by the uniform optical illumination between the contacts as shown in the below Figure 3.4.

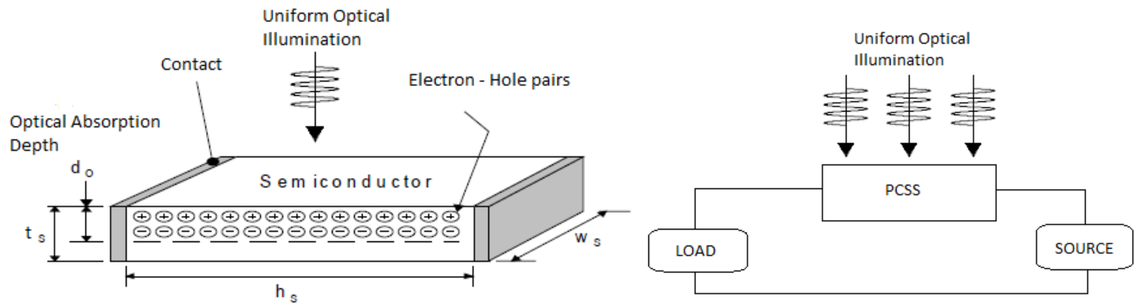

Figure 3.4: Illustration of a Photoconductive Semiconductor Switch (PCSS) [29].

This research is primarily focused on generation of Terahertz frequency using Gallium Arsenide PCSS. Modern research shows that the optical down-conversion is the most successful commercial and widely used technique for THz generation using Low temperature grown GaAs (LT-GaAs). The technique is widely known as Terahertz Time-Domain Spectroscopy (THz-TDS) [30]. This technique works by optical pulse excitation of a photoconductive switch. Where, a femto-second laser pulse illuminates a gap between two electrodes (which can also be used as an antenna) printed on a semiconductor substrate as shown in the below given Figure 3.5. The laser pulse creates electrons and holes which are then accelerated by the very high applied bias between the electrodes, this transient photocurrent, which is coupled to an antenna, contains frequency

components that reflect the pulse duration, hence generating an electromagnetic wave containing THz components.

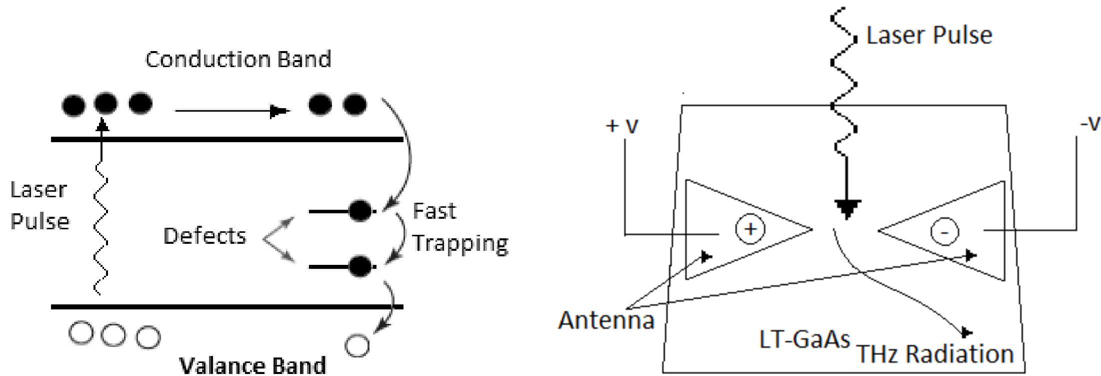

Figure 3.5: The figure in the left shows the flat band diagram of LT-GaAs showing defect levels provide fast trapping of photo excited electrons and the figure to the right shows the THz generation using LT-GaAs PCSS [31].

The primary reason for using LT-GaAs for generation of Terahertz is the material properties that are required for ultrafast photoconductive application. LT-GaAs has a unique combination of physical properties like it has very short carrier lifetime which can be less than 4 picoseconds, it has a very high resistivity, high electron mobility and high breakdown field which is usually in the range of $4 \text{ X } 10^5$ V/cm. The low temperature growth of GaAs which is usually done in the temperature range of 190-350 ℃, permits excess arsenic to be incorporated as point defects in the GaAs crystal known as arsenic antisite which represents the majority of the defects, arsenic interstitial and gallium vacancies. The ionized antisite defects which acts as deep donors, approximately at 0.7 eV bellow the conduction band provide fast trapping for electrons from the conduction band to mid-gap states. The LT-GaAs may have carrier life time as short as 90 femtoseconds which enables the fast trapping of electrons by arsenic antisite defects. This fast trapping and detrapping of electrons enhances the electron-hole recombination

leading to a substantial decrease in the electron lifetime, thus making the LT-GaAs suitable for high power THz generation.

3.8 Basic Antenna Parameter

The second part of this research is about embedding the PCSS in a device such that it acts as an antenna which can transmit and receive electromagnetic radiation in the Terahertz regime. An Antenna is a structure or a device that is allied with the region of transition between a guided wave and a free-space wave or vice versa. As per the property of antenna it can both transmit and radiate in all required direction. While an antenna is transmitting, the energy from the transmission line is radiated into space by the antenna and whereas during reception the energy from the incident EM wave is gathered by the antenna and sent down the transmission line [32]. Antenna is basically a transformation device converting electromagnetic photons into circuit elements, and it can also convert the energy from the circuit into photons radiated into the space. There are different types of antennas such as Wire antennas, Horn antennas, Bow-Tie antennas, Aperture antennas, Microstrip Antenna, Array of antennas, Reflector Antennas and many more.

3.8.1 Radiation Pattern of an Antenna:

The field strength of an antenna at any given point in space depends on its distance from the antenna and the angular coordinates of the point. The region close to the antenna will have a dominant reactive component and a radiating component. The reactive component reduces with the distance from the antenna. This region is called reactive near-field region. This research stresses more on the radiating component. The region with dominant radiating component can be further divided in two regions, namely

radiating near-field region and radiating far-field region. In the near-field region the angular distribution of the Electro Magnetic energy depends on the distance from the antenna. However, for the far-field region the radiating energy is completely independent of the distance from the antenna. Thus the Radiation Pattern is the directional or angular dependence of the strength of the electromagnetic waves from the antenna.

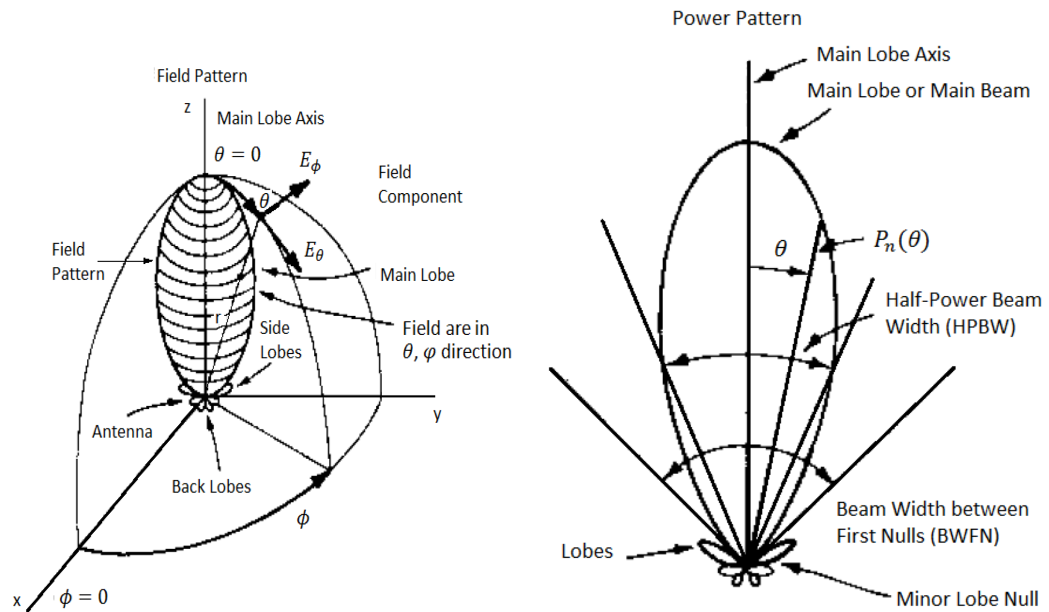

Figure 3.6: The left diagram shows the antenna field pattern with the coordinate system, the right diagram shows the Antenna power pattern in polar coordinates (linear scale) [32].

3.8.2 Lobes in Radiation Pattern:

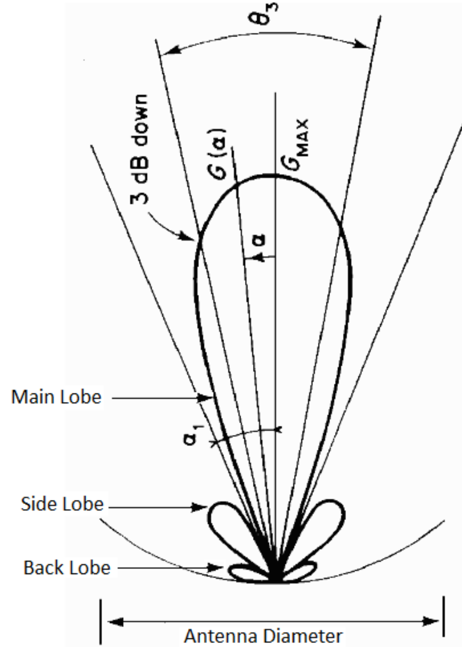

Figure 3.7: Lobes in radiation pattern [32].

It has been observed that the radiation pattern of an antenna has basically three types of lobes. These lobes are also referred to as beams and are formed due to the radiation from the antenna. The variations in these lobes are formed due to the selection of different parameters while designing the antenna like the length of the antenna, the feeding mechanism for the antenna, etc.

The main lobe is the major lobe of a radiation pattern; it is the region where the power of the radiation is the highest. For an isotropic antenna, the main lobes can be found on both sides of the reference coordinates. Referring to the above Figure 3.14, it can be observed a field pattern where r is proportional to the field intensity at a certain distance from the antenna in the direction of θ and ϕ. The field pattern has its main lobe maximum in the z direction ($\theta = 0$). Where, r is the distance between the origins of the radiation pattern to a point on the surface of the solid angle intended by the beam.

The side lobe and the back lobes are also referred to as the minor lobes. These are the beams that are away from the main beam. They are the power is being radiated in the undesired direction. However, the side lobe level is a very important parameter of the antenna radiation pattern. The space between the side lobes and the back lobes are called the nulls which are in the direction of zero or minimum radiation.

3.8.3 Radiation Intensity:

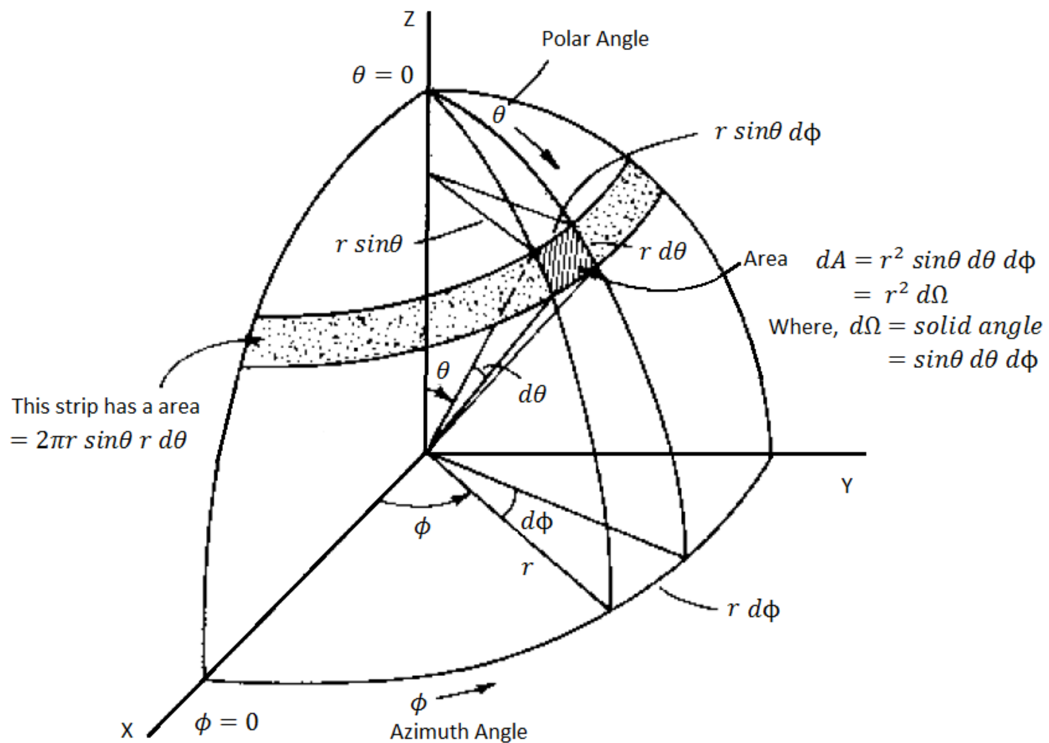

Figure 3.8: The spherical coordinates in relation to the area (dA) of solid angle $d\Omega = sin\theta\ d\theta\ d\phi$ [32].

Power radiated from the antenna per unit solid angle is called the radiation intensity. It is represented with the symbol U and the unit used is watts per steradian or watts per square degree.

Referring to the above Figure 3.8, it can be seen that an area A on the surface of the sphere as seen from the center of the sphere subtends a solid angle Ω. The total solid

angle subtended by the sphere is 4Π steradian or square radians. Thus the incremental area dA of the surface of the sphere is given by:

$$dA = (r\, sin\theta\ d\phi)(r\ d\theta) = r^2 \sin\theta\ \ d\theta\ d\phi = r^2 d\Omega \tag{3.45}$$

Where, $d\Omega$ = solid angle subtended by the area dA.

Thus the beam area or beam solid angle (Ω_A) for an antenna is given by the integral of the normalized power pattern over a sphere, which is given by:

$$\Omega_A = \int_0^{2\pi} \int_0^{\pi} P_n(\theta, \phi) d\Omega \tag{3.46}$$

Where, $P_n(\theta, \phi)$= the normalized power radiated from the antenna.

The normalized power pattern can also be expressed as the ratio of radiation intensity to its maximum value. Thus the equation stands as:

$$P_n(\theta, \phi) = \frac{U(\theta, \phi)}{U(\theta, \phi)_{max}} \tag{3.47}$$

Where, $U(\theta, \phi)$ = the radiation intensity at a particular point on the beam.

$U(\theta, \phi)_{max}$ = the maximum radiation intensity.

3.8.4 Beam Width and Beam Efficiency:

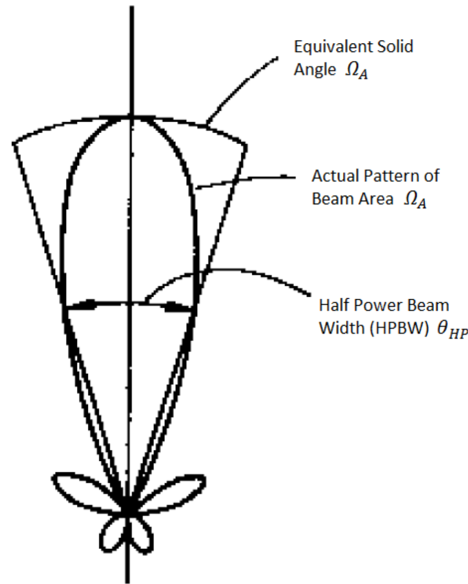

Figure 3.9: Cross section of a symmetrical power pattern of an antenna showing equivalent solid angle for a cone-shaped triangular pattern [32].

The solid angle which is subtended by the beam at the origin can also be described approximately in terms of angles subtended by the half power points of the main lobe in two principle planes and is given by the equation:

$$\Omega_A \cong \theta_{HP}\phi_{HP} \tag{3.48}$$

Where, θ_{HP} and ϕ_{HP} = the half power beam widths (HPBW) located in the two principal planes, minor lobes i.e. the side and the back lobes being neglected.

First-Null Beam Width (FNBW) is the angular separation between the first nulls of the pattern.

Beam efficiency is a function of the beam area (Ω_A). The total beam area (Ω_A) or beam solid angle consists of the main beam area or solid angle (Ω_M) plus the minor lobe area or solid angle (Ω_m). Thus the equation can be written as:

$$\Omega_A = \Omega_M + \Omega_m \tag{3.49}$$

The ratio of the main beam area (Ω_M) to the total beam area (Ω_A) is called the main beam efficiency (ε_M), therefore the equation stands as [32]:

$$\varepsilon_M = \frac{\Omega_M}{\Omega_A} = main\ beam\ efficiency \tag{3.50}$$

The ratio of the minor beam area (Ω_m) to the total beam area (Ω_A) is called the stray factor, therefore the equation stands as:

$$\varepsilon_m = \frac{\Omega_m}{\Omega_A} = stray\ factor \tag{3.51}$$

Thus we can say that:

$$\varepsilon_M + \varepsilon_m = 1 \tag{3.52}$$

3.8.5 Directivity:

The Directivity D of an antenna is given by the ratio of the maximum radiation intensity to the average radiation intensity. The directive gain of an antenna signifies the concentration of the radiated power in a particular direction. It may be also regarded as the ability of the antenna to direct radiated power in a given direction. The equation for directivity s given by [32]:

$$D = \frac{U(\theta, \phi)_{max}}{U_{avg}} \tag{3.53}$$

Where U_{avg} = the average radiation intensity at any given point on the beam.

$$D = \frac{4\pi}{\Omega_A} \tag{3.54}$$

Thus we can see that smaller the beam solid angle, the greater is the directivity of the antenna.

3.8.6 Gain:

Assuming the antenna to be a lossless isotropic source, the gain G of an antenna depends both on the antenna's directivity and efficiency. Thus the equation stands as:

$$G = kD \tag{3.55}$$

Where, k = the efficiency factor of the antenna, where, $0 \leq k \leq 1$ and is dimensionless. This efficiency is only related to the ohmic losses in the antenna [32]. While the antenna is transmitting, the losses involve power fed to the antenna which is not being radiated by the antenna, but instead heats the antenna structure. Mathematically, the Gain of an antenna is the ratio between intensity in a given direction to the average radiation intensity when the power is radiated isotropically.

$$G = \frac{U(\theta, \emptyset)}{U(\theta, \emptyset)_{avg,isotropic\ radiation}} \tag{3.56}$$

3.8.8 Bandwidth:

The range of frequencies around which the antenna operates, i.e. the design frequency or the resonant frequency for which the antenna parameters such impedance, radiation pattern, beam width, polarization, side lobe level, gain, and beam direction are within the acceptable range is referred to as the bandwidth of the antenna [32].

In the research discussed chapter 4 and 5 simulation results from LT GaAs and photoconductive emitter will be analyzed in terms of the parameters discussed in this chapter.

CHAPTER 4

Simulation of GaAs PCSS and Antenna

(Use of SILVACO and MICROWAVE STUDIO Codes)

The simulation study is divided into two parts. First the substrate conditions of the GaAs PCSS are analyzed through the SILVACO simulation suite. The pulse generated from this exercise is utilized in the MICROWAVE STUDIO code to study the radiation characteristics of the contacts, which essentially is a dipole antenna. Other contact or antenna types are also studied. The antenna, made from copper on the top of the substrate, is aperture fed from the bottom and the input signal essentially represents the pulse generated by the PCSS during each on-state transient. The far field pattern, the gain and the directivity of the antenna is then analyzed in the second part of the simulation. This chapter essentially deals with the simulation setup using the codes, while the simulation results and analysis is done in chapter 5.

PART I Substrate Simulation Setup

4.1 Silvaco Simulation Suite:

The Silvaco software comes with a device editor called the Devedit, which was used to fabricate the PCSS. The Atlas is also a major part of Silvaco which was used to simulate the device. Basically the two and three dimensional structures can be simulated with the Atlas and the Devedit modules of the Silvaco ™ code. The Atlas module in conjunction to the Blaze module was used to determine the characteristics of the switch.

The Blaze module was used since it has the means to analyze group III-V materials. ATLAS predicts the electrical behavior of specified semiconductor structures and provides insight into the internal physical mechanisms associated with device operation.

Silvaco is a commercially available comprehensive software tool that can perform semiconductor device simulations and circuit simulations. This software included numerous models and parameters that are used to define a specific situation to obtain optimal results. The code is written on a program module called Deckbuild. First we design the device on Devedit. Devedit is GUI (Graphical user Interface) based module, where the device can be created using it's in build functionalities. After you have determined the doping level, contacts or electrodes on the device, we create the mesh in the Devedit. Then we import the design made in Devedit to Deckbuild and start appending the code as per the situation. The Atlas module is the main interface, which interacts with the Devedit process modules in the Deckbuild module. Atlas is usually a Physically-based device simulator which predicts the electrical characteristics that are associated with specified physical structure of a device and the bias conditions that is subject to the device operation. This is achieved by approximating the operation of a device onto a two or three dimensional grid, consisting of a number of grid points called nodes. By applying a set of differential equations, derived from Maxwell's laws, onto this grid you can simulate the transport of carriers through a structure. These three modules can be used to with other interactive tools which provide for two and three – dimensional semiconductor device simulations like Thin Film Transistor (TFT), Quantum devices, Hetero structures and Power devices. There is also another way of fabricating of the device using the Athena module which is used for Process simulation. The resulting

meshes that are usually formed in the Athena Process simulation can be reused for device simulation using the Atlas module. Furthermore, in a mixed mode environment a particular device that has been created using Athena, Devedit can be used in a circuit, and the effects of any changes in the device parameters on the overall circuit can be analyzed. In addition to the Drift-diffusion model, users can perform other kinds of study such as non-local effects on velocity overshoot, reduced energy dependent impact ionization, and etc. Finally, the code also has a provision to incorporate user defined functions through a C- interpreter. Further details about the software can be found in Atlas User Manual.

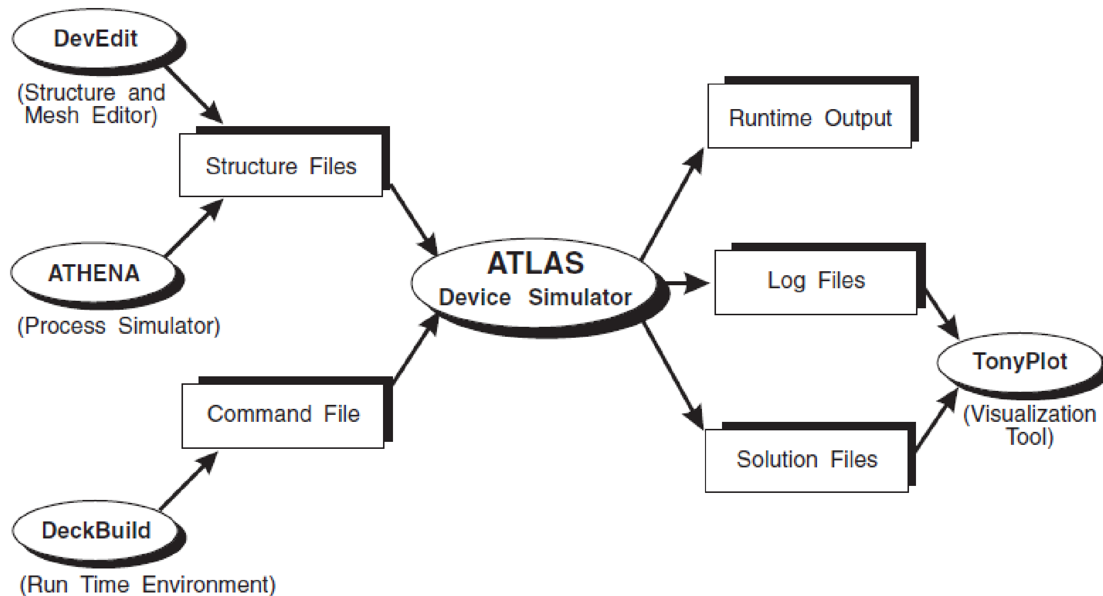

Figure 4.1: The Atlas Inputs and Outputs [27].

It is known and studied that the resistivity of the semiconductor materials such as Gallium Arsenide (GaAs) or Silicon (Si) or Silicon Carbide (SiC) can be altered by illuminating the surface of the material with laser or light from any optoelectronic source whose photon energy is greater than the semiconductor band-gap energy. The photon energy which is being absorbed by the semiconductor material generates electron hole pairs with efficiency nearly equal to unity. This phenomenon is commonly known as

photoconductivity[33]. This photoconductive property of semiconductor material has been enormously used in various kinds of applications, majorly in high-speed photo-detectors [34] and high-speed sampling gates [35] with sub-millimeter dimensions, and high power switches [36]. However, based on the response of the semiconductor material to majority carrier injection, semiconductor materials can be classified as relaxation type and lifetime type. The relaxation type semiconductors display the kind of behavior in which the Debye Length is much greater than the Diffusion length i.e. $L_D >> L_O$, the majority carrier injection leads to a majority carrier depletion [33]. While in the case of lifetime type semiconductors where the Diffusion length is much greater than the Debye length i.e. $L_O >> L_D$, thus in this case, the majority carrier injection leads to majority carrier augmentation [33]. The behavior and the working principle of a photoconductive switch are basically dominated and are further complicated by the presence of trap sites. The existence of the trap sites modifies the space charge and the electric field distribution in the material, it also provides an alternative recombination – generation mechanism affecting the lifetime of the carriers, thus affecting the overall material behavior. It has been studied and shown by Henisch and coworkers that due to the existence of large density trap sites the depletion of majority carriers is greatly reduced upon injection of minority carriers, thus the material behavior changes to lifetime type instead of the relaxation type. The lifetime type semiconductors are of high resistivity, whereas the compensated type materials are used for photoconductive semiconductor_switches (PCSS's), infrared detectors and the like etc [37]. Therefore, a further detailed and meticulous study of this type of material is required in order to understand and predict the correct response of the PCSS. This chapter starts with the lattice structure of the Gallium

Arsenide (GaAs) crystal, followed by the working principle of a PCSS device and the different types of it available in the modern world. Then we explain the effect of the location of trap level on the material response. The theory of current injection in solids topic is also being discusses here.

4.2 Simulation Mesh Parameters:

After the device was created, the mesh was build. The mesh is made finer twice in both X- direction and in Y-direction to avoid the convergence problem. The mesh is being made finer at the contacts or electrodes since most of the generated carriers will be captured by the electrodes which are subjected to very high bias voltages. The middle portion of the device also has a refined mesh since most of the carrier generation and recombination happens at this place. The mesh is one of the most critical parameters for obtaining the correct simulation results. However, a tradeoff has to be made between the accuracy and the numerical efficiency. The major reasons for making a finer mesh at the above mentioned regions are given hereby:

- High Electric fields exist at the electrodes.
- Recombination mechanism goes on near the electrodes.
- The middle portion is the area where very high impact ionization is observed.
- Trapping and detrapping of the carriers are observed in the middle region of the device.

The creation and refinement of the mesh was done taking consideration of three major factors, they were:

- Ensure high mesh density in the high field areas.
- Avoid obtuse angle triangles in the current path or high field areas.

- Avoid abrupt discontinuities in the mesh density.

The mesh can also defined in Atlas using Deckbuild. A very fine or refine the mesh can be made by using the inbuilt algorithm given by Deckbuild. The designed device had nearly 8,500 mesh points and takes approximately about 40 minutes in an Intel Core 2 Duo processor to run a device simulation.

The mesh for our 50 µm X 50 µm PCSS is shown in the below given Figure.

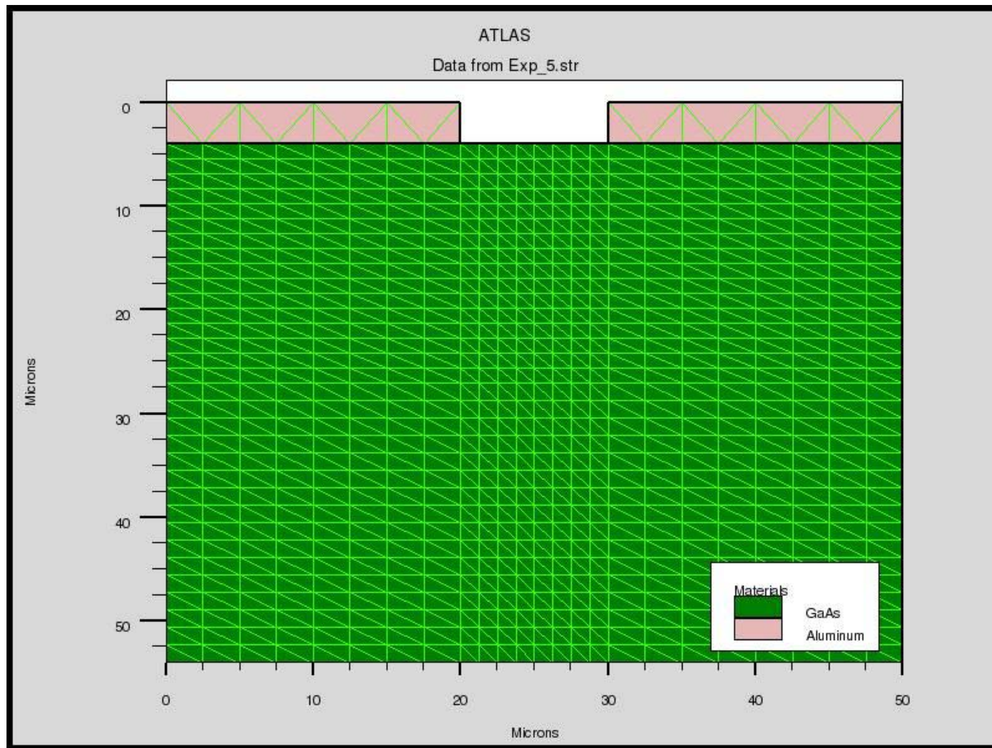

Figure 4.2: Mesh configuration of the designed PCSS.

4.3 Traps and Defects:

The semiconductor materials are bound to have crystal flaws due to the presence of dangling bonds at interfaces or impurities in the substrate while fabrication. These defect centers are also known as Traps. The presence of these traps in the semiconductor surface determines the electrical properties of the semiconductor device. The trap centers have their presence felt in the forbidden gap. They exchange charge with the conduction

and the valence band through emission and capture of electrons. The Trap center determines the density of space charge in a bulk semiconductor. There are basically two types of traps:

a) Donor Trap: can either positive or neutral. A donor-like trap is positively charged or ionized when empty and neutral when filled with an electron. A filled donor-type trap emits an electron or captures a hole.

b) Acceptor Trap: can either be negative or neutral. An acceptor-like trap is negatively charged when ionized and neutral when filled with an electron. A filled acceptor-like trap emits an electron or captures a hole.

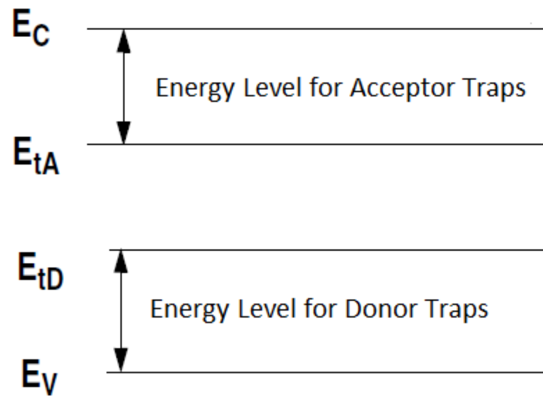

Figure 4.3: The acceptor and donor trap energy level in reference to conduction and valence band edges [27].

From Poisson's equation we can find the total charge in the semiconductor due to the presence of Traps. Thus the equation stands as:

$$Q_T = q(N_{tD}^{+} - N_{tA}^{-}) \tag{4.17}$$

$$N_{tD}^{+} = Density\ X\ F_{tD} \tag{4.18}$$

$$N_{tA}^{-} = Density\ X\ F_{tA} \tag{4.19}$$

Where, Q_T = the total charge value.

N_{tD}^{+} = the ionized donor-like trap.

N_{tA}^{-} = the ionized acceptor-like trap.

F_{tD} = the probability donor trap ionization.

F_{tA} = the probability acceptor trap ionization.

The total charge for multiple traps for multiple energy levels is give by:

$$N_{tD}^{+} = \sum_{\alpha=1}^{k} N_{tD\alpha}^{+} \quad (4.20)$$

$$N_{tA}^{-} = \sum_{\beta=1}^{m} N_{tA\beta}^{-} \quad (4.21)$$

Where k = the number of donor traps.

m = the number of acceptor traps.

The probability of ionization for the acceptor and donor like traps are given hereby:

$$F_{tA} = \frac{v_n\sigma_n + e_{pA}}{v_n\sigma_n + v_p\sigma_p + e_{nA} + e_{pA}} \quad (4.22)$$

$$F_{tA} = \frac{v_p\sigma_p + e_{nD}}{v_n\sigma_n + v_p\sigma_p + e_{nD} + e_{pD}} \quad (4.23)$$

Where, σ_n = the electron capture cross section.

σ_p = the hole capture cross section.

v_n = the thermal velocity of the electrons.

v_p = the thermal velocity of the holes.

e_{nA} = the electron emission rate for acceptor like traps.

e_{pA} = the hole emission rate for acceptor like traps.

e_{pD} = the hole emission rate for donor like traps.

e_{nD} = the electron emission rate for acceptor like traps.

The electron and the hole emission rates for acceptor like traps are given hereby:

$$e_{nA} = g v_n \sigma_n n_i \exp\left(\frac{E_t - E_i}{kT_L}\right) \tag{4.24}$$

$$e_{pA} = \frac{1}{g} v_p \sigma_p n_i \exp\left(\frac{E_i - E_t}{kT_L}\right) \tag{4.25}$$

The electron and the hole emission rates for donor like traps are given hereby:

$$e_{pD} = \frac{1}{g} v_n \sigma_n n_i \exp\left(\frac{E_t - E_i}{kT_L}\right) \tag{4.26}$$

$$e_{nD} = g v_p \sigma_p n_i \exp\left(\frac{E_i - E_t}{kT_L}\right) \tag{4.27}$$

Where, g = the degeneracy factor of the trap center.

E_i = the intrinsic Fermi Level.

E_t = the trap energy level.

4.4 Recombination Model with Trap implementation:

The standard SRH recombination is given by the below given equation:

$$R = \sum_{\alpha=1}^{l} R_{D_\alpha} + \sum_{\beta=1}^{m} R_{A_\beta} \tag{4.28}$$

Where l = the number of acceptor like trap.

m = the number of donor like trap.

For donor and acceptor like traps, the function R is given by:

$$R_{D_\alpha} = \frac{pn - n_{ie}^2}{\tau_n \left[p + g n_{ie} \exp\left(\frac{E_i - E_t}{kT_L}\right)\right] + \tau_p \left[n + \frac{1}{g} n_{ie} \exp\left(\frac{E_t - E_i}{kT_L}\right)\right]} \tag{4.29}$$

$$R_{A_\beta} = \frac{pn - n_{ie}^2}{\tau_n \left[p + \frac{1}{g} n_{ie} \exp\left(\frac{E_i - E_t}{kT_L}\right)\right] + \tau_p \left[n + g n_{ie} \exp\left(\frac{E_t - E_i}{kT_L}\right)\right]} \tag{4.30}$$

Where, τ_n = the electron lifetime.

τ_p = the hole lifetime.

The electron and the hole life time is a function of the electron and hole capture cross sections respectively, and is given by:

$$\tau_n = \frac{1}{v_n \sigma_n density} \tag{4.31}$$

$$\tau_p = \frac{1}{v_p \sigma_p density} \tag{4.32}$$

The thermal velocities are determined by the electron and the hole effective masses, and is given by:

$$v_n = \left(\frac{3kT}{m_n m_0}\right)^{\frac{1}{2}} \tag{4.33}$$

$$v_p = \left(\frac{3kT}{m_p m_0}\right)^{\frac{1}{2}} \tag{4.34}$$

Where, m_n = the electron effective mass.

m_p = the hole effective mass.

T = the lattice temperature.

4.5 Mobility Models:

Electrons and holes are accelerated by electric fields, but lose momentum as a result of various scattering processes. Mobility modeling is normally divided into:

(i) low-field behavior,

(ii) high field behavior,

(iii) bulk semiconductor regions and

(iv) Inversion layers.

The mobility models that were used for these experiments were:

1) Concentration Mobility (CONMOB): This model is used for the analysis of the mobility of electrons and holes in the semiconductor substrate. Since have worked with concentration ranging from $1X10^{15}/cm^3$ to $1\,X10^{16}/cm^3$, thus this model makes it effective to calculate the mobility values for the carriers.

2) Parallel Electric Field –Dependent Mobility Model (FLDMOB): When the electric field magnitude becomes significant, the carriers are accelerated in an electric field. The velocity of the carriers begins to saturate. This effect is being determined by the reduction of the effective mobility. We know that the magnitude of the drift velocity is the product of the mobility and the electric field component in the direction of the current flow. Thus the mobility of electrons and hole are given by:

$$\mu_n(E) = \mu_{n0}\left(\frac{1}{1+\left(\frac{\mu_{n0}E}{v_{sat,n}}\right)^{BETAN}}\right)^{\frac{1}{BETAN}} \tag{4.35}$$

$$\mu_p(E) = \mu_{n0}\left(\frac{1}{1+\left(\frac{\mu_{p0}E}{v_{sat,p}}\right)^{BETAP}}\right)^{\frac{1}{BETAP}} \tag{4.36}$$

Where, E = the parallel electric field.

μ_{n0} = the low-field electric mobility.

μ_{p0} = the low-field hole mobility.

$v_{sat,n}$ = the electron saturation velocity.

$v_{sat,p}$ = the hole saturation velocity.

$BETAP$, $BETAN$ = user defined parameters for mobility model.

The value of these $BETAP$, $BETAN$ can be determined by using the Canali Model.

3) SRH Model: The Shockley-Read-Hall model recombination model is as follows:

$$R_{SRH} = \frac{pn - n_{ie}^2}{\tau_{p0}\left[n + n_{ie}\, exp\left(\frac{ETRAP}{kT_L}\right)\right] + \tau_{n0}\left[n + n_{ie}\, exp\left(\frac{-ETRAP}{kT_L}\right)\right]} \quad (4.37)$$

Where, ETRAP = the difference between the trap energy level and the intrinsic Fermi level.

4) Auger: Auger recombination occurs through a three particle transition whereby a mobile carrier is either captured or emitted. Thus the equation stands as:

$$R_{Auger} = AUGN(pn^2 - nn_{ie}^2) + AUGP(np^2 - pn_{ie}^2) \quad (4.38)$$

Where, $AUGN$ and $AUGP$ = the parameters defined by the user in the material statement.

5) Band to Band Tunneling: If a very high electric is present within the device, then there occurs a phenomenon called local band bending through which the electrons are allowed to tunnel by using the internal field emission from the valence band to the conduction band. The equation for Band to band tunneling is given hereby:

$$G_{BBT} = BB.A\ E^{BB.GAMMA} \exp\left(-\frac{BB.B}{E}\right) \quad (4.39)$$

Where, BB.A, BB.B and BB.GAMMA = user defined parameters.

The model parameters values were set as per the Klassen Model, where the values for the user defined parameters are given by:

$$BB.A = 4.00\ X\ 10^{14}\ cm^{-1}V^{-5/2}sec^{-1} \quad (4.40)$$

$$BB.B = 1.97\ V/cm \quad (4.41)$$

$$BB.GAMMA = 2.0 \tag{4.42}$$

4.6 CST Microwave Studio Simulation Setup:

The Second Part of this research is to design the antennas in CST Microwave Studio and analyze the same. CST Microwave Studio (CST MWS) is a specialized tool for the 3D EM simulation of high frequency components. CST MWS enables the fast and accurate analysis of high frequency (HF) devices such as antennas, filters, couplers, planar and multi-layer structures. CST MWS quickly gives you an insight into the EM behavior of your high frequency designs. It also offers great flexibility in tackling a wide application range through the variety of available solver technologies. The Time Domain solver and the Frequency Domain solver of CST MWS have immense applications for various kinds of HF EM devices. CST uses Finite Integration Technique (FIT) as the transient solvers. The FIT based transient solvers apparently increases the accuracy of the simulation results.

4.7 Simulation Parameters used for this research:

An input file was created with the device structure. This input file contains a sequence of statements that are executed by the Deckbuild. Doping a particular device is perhaps the most important process that is required to simulate the semiconductor device.

4.8 Construction of the PCSS in Devedit:

- First resize the 10 µm X 10 µm default work area to a 60 µm X 60 µm.
- A GaAs PCSS is being designed which is 50 µm X 50 µm in size.
- The two aluminum contacts were made on top of the PCSS. The contacts were made at the far ends on the top surface of the PCSS switch. The size of the electrodes was 5 µm X 20 µm in size.
- Build the mesh for simulation purpose. The mesh parameters was:

  - The base mesh height was 10 microns.
  - The base mesh width was 10 microns.
  - The maximum ratio was chosen to be 100.
- Then we save the file as a structure file (*.str) and a command file (*.in).
- We open Devedit and import the command file that we have saved in the earlier step.
- We start appending the code with the proper parameters.

4.9 Explanation of the code and the simulation parameters:

The code to simulate the LT GaAs PCSS starts from the statement "go atlas". The go atlas statement basically tells the Deckbuild to start the simulation of the ATLAS module. The ATLAS module reads the parameters and executes the code with the predefined parameters. The sequence of the simulation process is explained below step by step:

- Uniformly dope the GaAs PCSS with p-type impurities with a peak concentration of $2.98\, X\, 10^{15}\ /cm^3$.
- Introduce traps in the GaAs to make it a relaxation type of semiconductor.
- Add donor type impurities to the substrate which will act as traps in the semiconductor and its energy level at 0.732 eV, and the density of the trap is fixed at $3.01\, X\, 10^{15}\ /cm^3$. This value gives the GaAs its semi insulating nature and is referred from the work done by Dr. Naz Islam [38].
- The degeneracy rate (g) is considered to be 2 and the electron and hole carrier lifetime is considered as $6X\, 10^{-16}\ secs$ and $1.5\, X\, 10^{-18}\ secs$ respectively.

- The beam is defined to shining from the center of the switch and the position is perpendicular to the switch. The beam wavelength is chosen to be .78 μm.
- Considered the concentration mobility model (CONMOB) for high concentration of the carriers, Parallel Electric Field –Dependent Mobility Model (FLDMOB) for the PCSS will be operating in a very high electric field of nearly 1100 V, Shockley-Read-Hall (SRH) recombination model, auger model and band to band tunneling model with Klassen parameters.
- Considered the Selberherr's (SELB) impact ionization model for calculating the generation of excess carriers.
- Use the Newton method for the numerical analysis of the device parameters.
- Solve the initial condition and then move on to check the material properties of the device simulated. If the material shows semi-insulating properties then move on to hit the switch with the laser beams and analyze its photoconductive property.
- Design the antenna with the LT GaAs substrate and analyze its performance.

4.10 Setup for Patch Microstrip Antenna Design:

The aperture coupled microstrip antennas with dual patches on the top surface was designed. The aperture on the ground plane is rectangular and circular in nature. The ground plane is located between the top and the bottom substrate. The substrate dimension is chosen to be 50 X 50 micrometers, which is exactly identical with PCSS switch. The substrate material is LT GaAs who has a permittivity of 12.94. No LT-GaAs is a non dispersive material whose permittivity is same throughout the simulation and

also during the photocurrent generation. The LT GaAs substrate conditions are given hereby:

Material	Gallium Arsenide (Lossy)	Permeability μ	1
Type	Low Temperature	El.tnad	0.006
Permittivity ε	12.94	Thermal Conductivity	54 W/K/m
Young's modulus	85 kN/mm^2	Poisson's Ratio	0.31

Table 4.1: The Substrate condition of the GaAs used for antenna design

The material used for the patch is copper.

The material properties of Copper are given hereby:

Material	Copper (Hard Drawn)	Permeability μ	1
Type	Lossy Metal	El.cond.	5.96 X 10^7 S/m
Rho	8930 kg/m^3	Thermal Conductivity	401 W/K/m
Young's modulus	120 kN/mm^2	Poisson's Ratio	0.33

Table 4.2: The patch material parameters used for antenna design

The detailed designed of the antenna and its parameters are given below:

Length of the substrate = 50 μm

Width of the substrate = 50 μm

Thickness of the substrate = 0.5 μm

Width of the patch = 20 μm

Length of the patch = 50 μm

Thickness of the patch = 0.07 μm

The distance between the top and the bottom patch = 10 μm

The length of ground plane = 50 μm

The width of the ground plane = 50 μm

The thickness of the ground plane = 0.07 μm

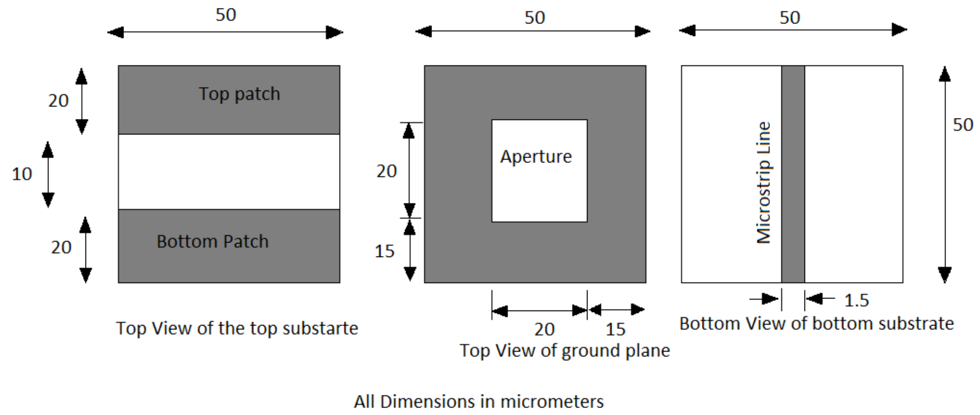

Figure 4.4: Shows the design of the dual patch ACMSA with a rectangular aperture and its dimensions.

The shape was changed from rectangular circular apertures to see the variation in the radiation pattern. The circle has a diameter of 5 micrometers whole center coincided with the center of the patch.

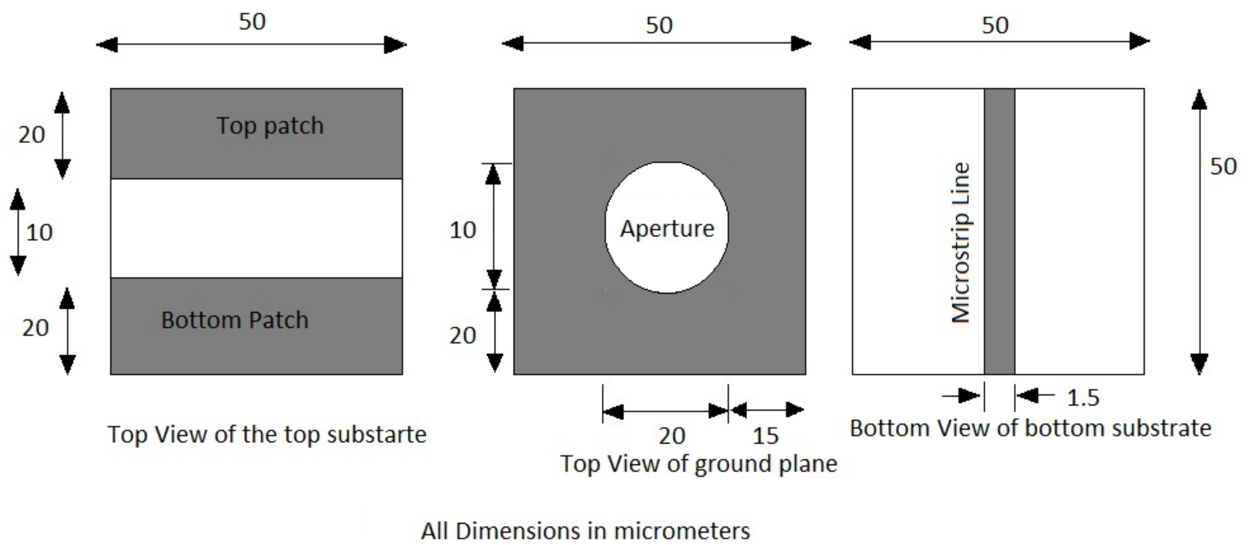

Figure 4.5: Shows the design of the dual patch ACMSA with a circular aperture and its dimensions.

The other two kind of design were made with triangular shaped patches. The base of the triangular patch was chosen to be 50 micrometers and the height of the patch was 20 micrometers.

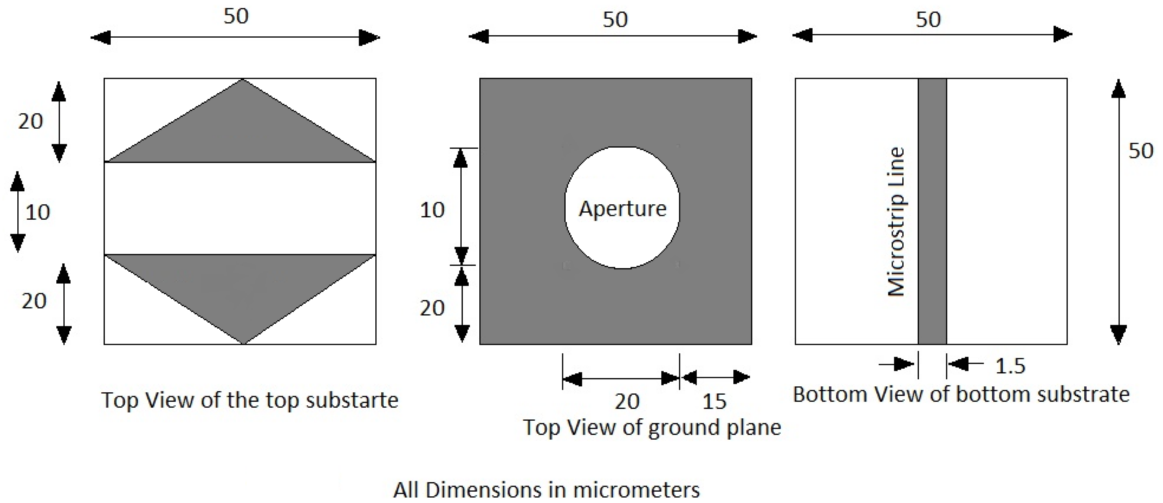

Figure 4.6: Shows the design of the dual triangular patch ACMSA with a circular aperture and its dimensions.

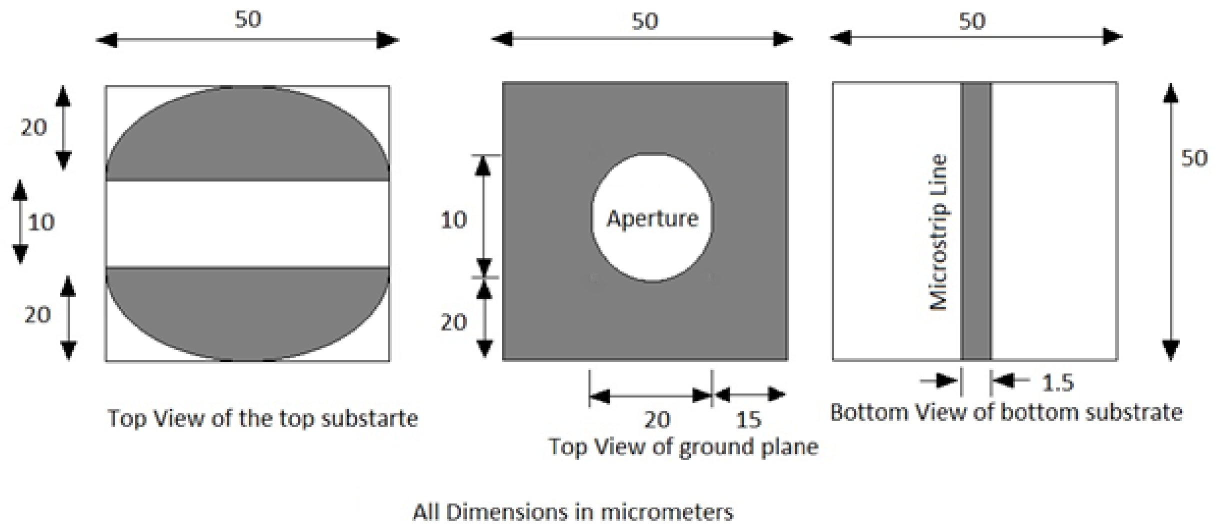

Figure 4.7: Shows the design of the dual semicircular patch ACMSA with a circular aperture and its dimensions.

The Background Properties and the Boundary conditions that are being applied for the simulation experiments are given hereby:

- Set the units to time to picoseconds, Temperature to Kelvin, Frequency to Terahertz, and Dimensions to micrometers.

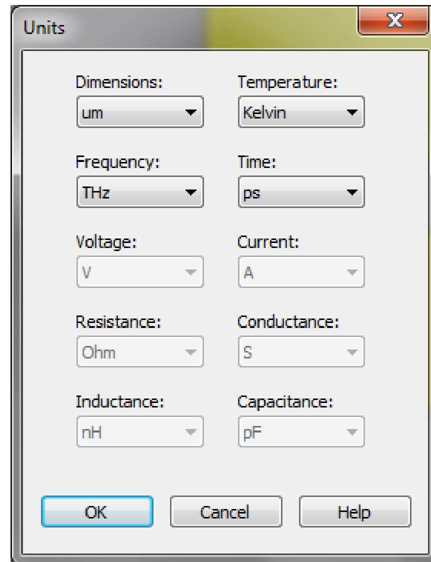

Figure 4.8: Shows the units fixed for the simulation experiments.

- The Background properties i.e. the conditions and the medium in which the switch/antenna will be operating. Choose free space as the boundary conditions. The permittivity and permeability are set to 1 for both the cases signifying it as a free space.

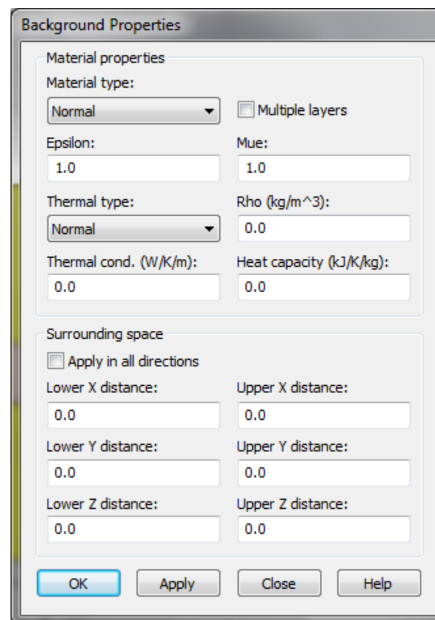

Figure 4.9: Showing the units chosen for the simulations.

- In case of boundary condition we have chosen Open Add space in all three axes. The open add space operates like a free space where waves can pass this boundary with minimal reflections. It also adds some extra space for farfield calculations.

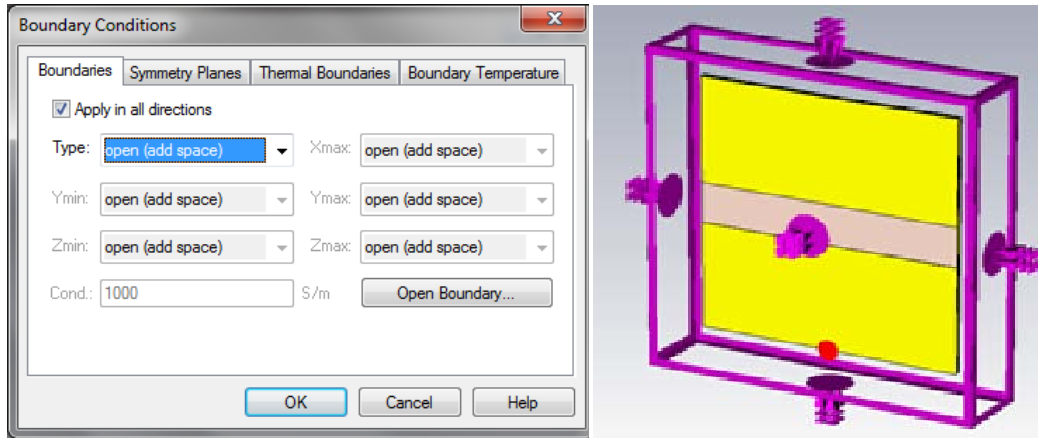

Figure 4.10: Showing the Background conditions used for the simulation of the antenna.

- We will be simulating the from a frequency range of 0.11 THz to 22 THz.

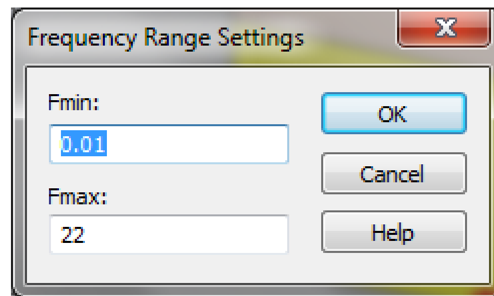

Figure 4.11: Showing the Frequency Range Settings.

- The input excitation signal is given as the same as the photoconductive pulse generated when the emitter was subjected to 0.78 micrometers wavelength laser beam under 1100 V bias.

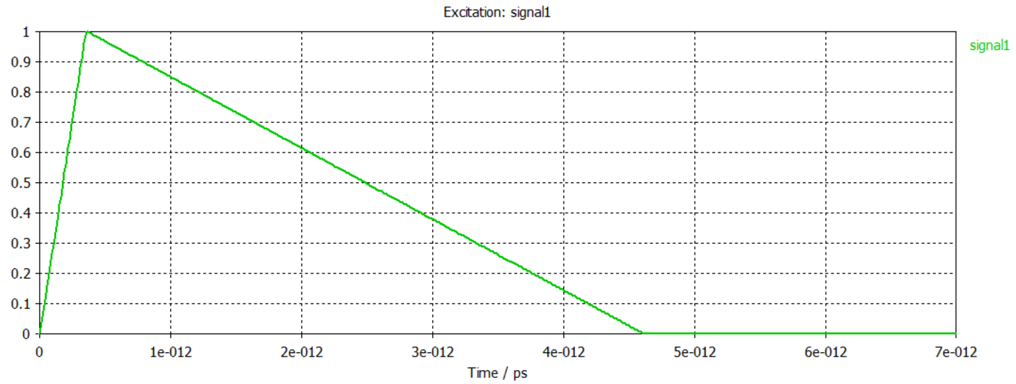

Figure 4.12: The input pulse fed to the antenna.

The photocurrent that is being generated in the photoconductive emitter that current sis being captured at the electrode which in turn will be radiated through the patches or electrodes.

- Proceed to simulate the antennas. While simulating the antennas have -30dB as the accuracy for the ease of numerical analysis.

CHAPTER 5
Results and Discussion:

Generating a Current Source Antenna and Radiation Analysis

Simulations were run based on the setup for the PCSS and its antenna (contacts) described in Chapter 4. The sequence of operation is as follows; SILVACO simulations for the GaAs PCSS is expected to provide the pulse shape that will be used as input to the antenna (the PCSS contact) simulation software (MICROWAVE STUDIO), where the characteristics of the antenna parameters, like directivity, gain will be analyzed. Besides the pulse shape, the semiconductor simulation is expected to provide insight into the conditions inside the PCSS during the transient.

5.1 CURRENT SOURCE FOR ANTENNA: SILVACO PCSS SIMULATIONS

The pulse generated in the substrate travels to the contacts of the PCSS, which act as dipole antenna producing electromagnetic radiation. SILVACO based simulations were done to study the pulse shape while the E-field, current density and other parameters in the substrate monitored. To study the pulse generated in the PCSS substrate through photoconductivity, a two step-simulation was carried out. First, the bias across the structure was incremented in steps to determine the maximum possible voltage at which the device can be operated. This is prior to device breakdown voltage, also known as the hold-off voltage where there is very small or no conduction current. Then, at the

hold-off voltage, the device was made to conduct through laser illumination to generate a pulse that travels to the contacts.

To determine the breakdown voltage, the bias across the device was increased in steps, as shown below.

- zero to 250 Volts with 1 Volt as step bias,
- 250 Volts to 500 Volts with 5 Volts as step bias,
- 500 Volts to 1100 Volts
- 1100 Volts to 1750 Volts with 10 Volts as step bias.

The breakdown voltage was about 1300 V and the device was operated at 1100 V for the PCSS on-state pulse generation.

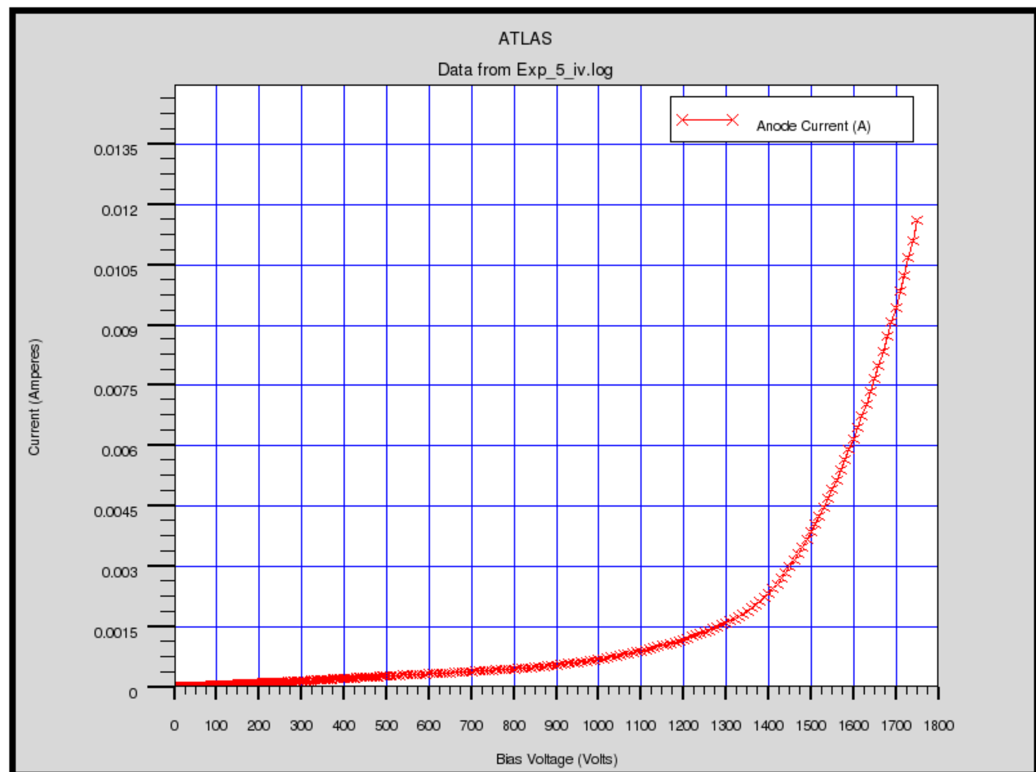

Figure 5.1 shows the I-V characteristics generated through bias increments (250 Volts, 500 Volts, 1100 Volts, and then finally to 1750 Volts).

Snapshots of several device parameters at the bias points were saved for analysis. The I-V characteristics of the PCSS material behaved as a trap filled, semi-insulating as has been reported earlier [8]. Since the structure was made semi-insulting through the compensation mechanism of the n-type EL2 traps and the p-type dopants, in the initial voltage increase, most of the carriers generated are captured by the traps and do not take part in the conduction process. Once the traps are filled, current increase is first due to double injection (both carriers taking part in conduction without getting captured by trap site) and, at very high bias, due to high field induced impact ionization. A rapid increase in current leads to avalanche breakdown. Thus, it is advisable to bias the device at the onset of double injection. The onset of double injection can be determined from the substrate conditions of the PCSS at every voltage levels. In the simulation study of the PCSS using SILVACO a number of voltage incremental point were monitored and the ones of interest are shown in Figures 5.2 to 5.8.

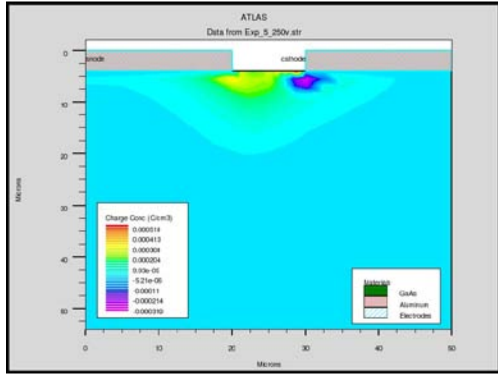

(a)

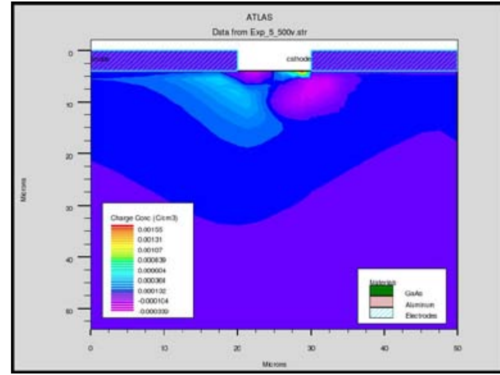

(b)

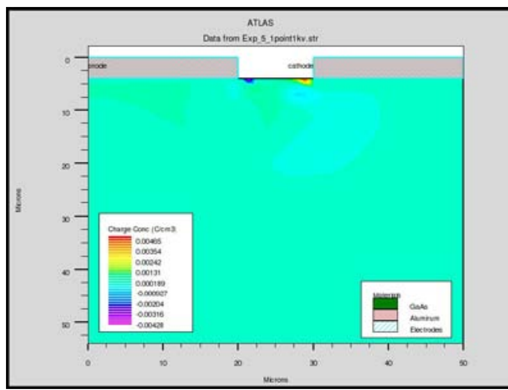

(c)

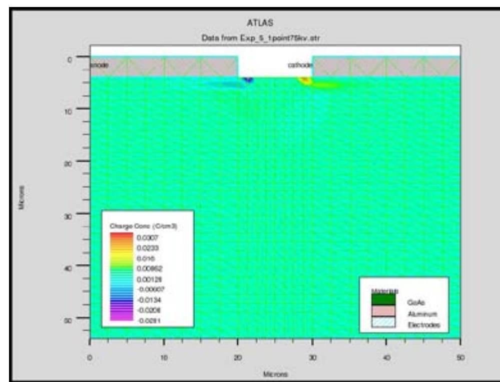

(d)

Figure 5.2: Shows the charge concentration in the LT PCSS at (a) 250 V, (b) 500 V, (c) 1100 V and (d) 1750V.

From the Figure 5.2 we can see that the charge concentration begins to build up as the bias voltage is increased. This is because there is an initial increase in the capture of charges injected into the substrate, and the phenomenon of trap filled transport is initiated.

Figure 5.3 essentially mirrors the observation made earlier. That is once the trap levels are filled due to initial capture, the conduction current density also increases. .

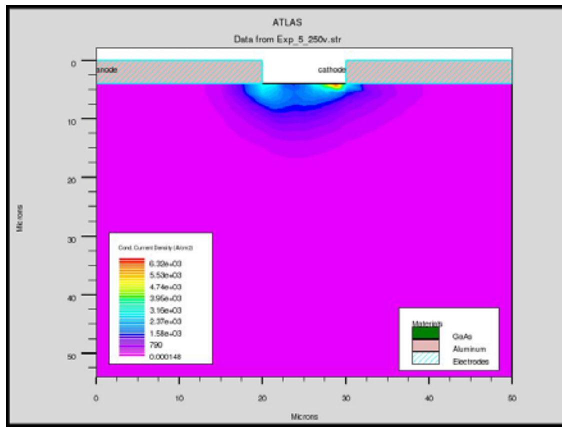

(a)

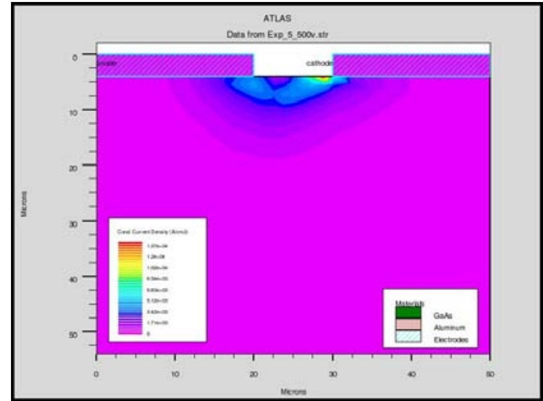

(b)

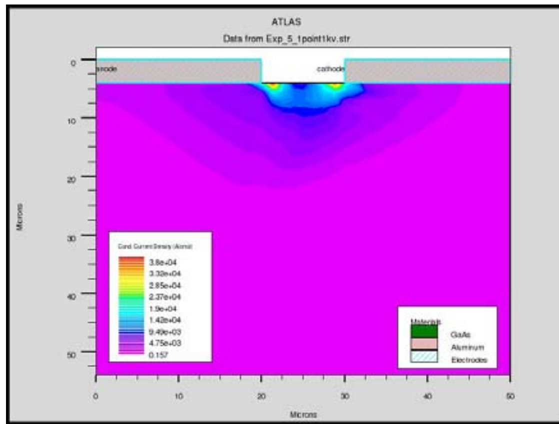

(c)

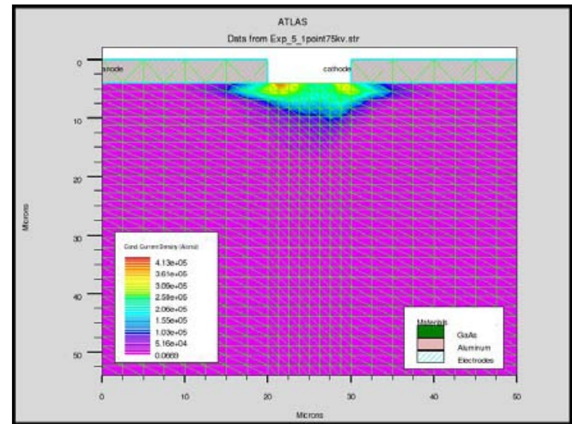

(d)

Figure 5.3: Showing the conduction current density at (a) 250 V, (b) 500V, (c) 1100 V and (d) 1750 V respectively throughout the LT GaAs PCSS.

This is evident from Figure 5.3, where the conduction current is very low at the contacts at 250 V and there is practically no conduction current. At 1300 V the conduction current density increases. As the bias voltage is increased the conduction density increases abruptly and reaches its highest 1750 Volts.

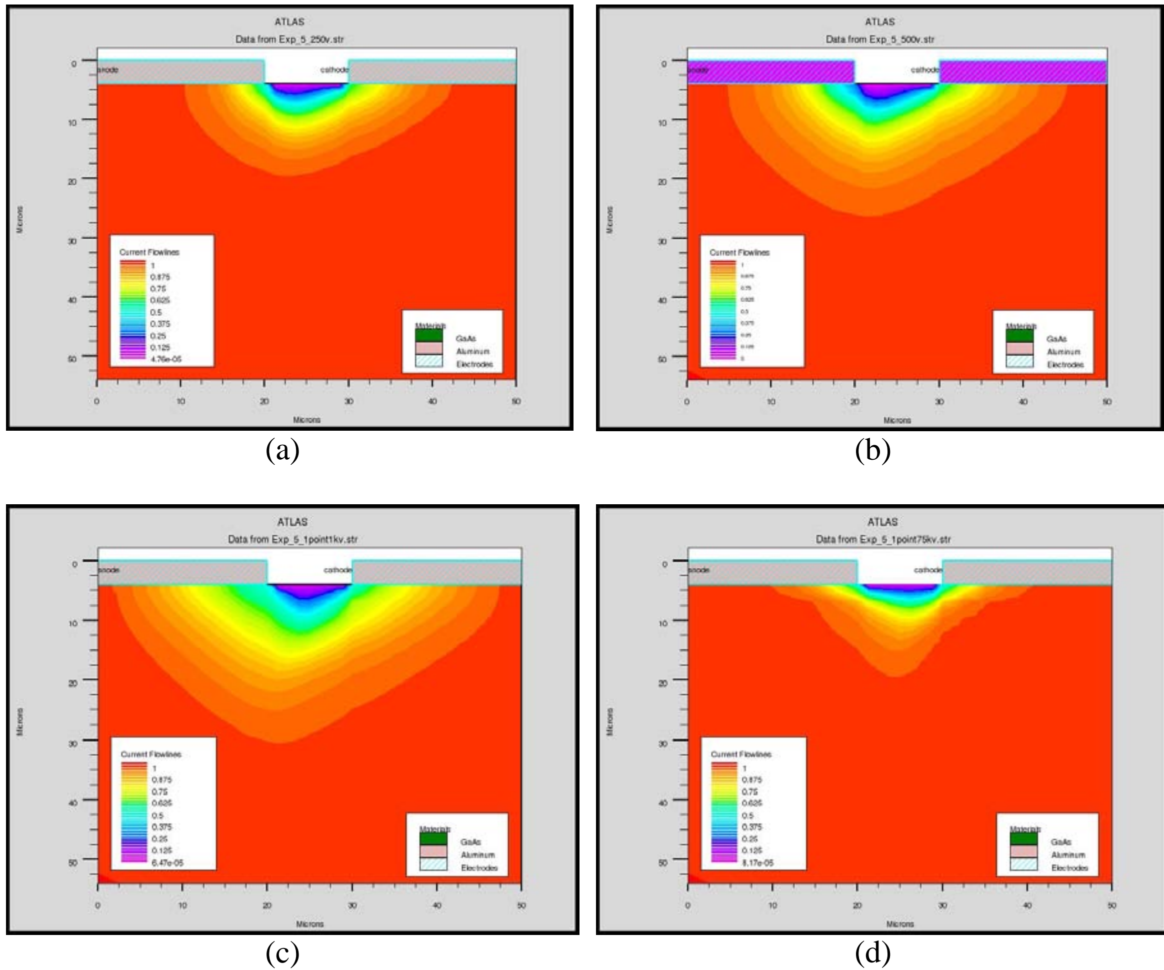

Figure 5.4: Showing the current flow lines at (a) 250 V, (b) 500V, (c) 1100 V and (d) 1750 V respectively throughout the LT GaAs PCSS.

In Figure 5.4 shows the differences in the current flow lines at various bias voltages. Figures 5.4 (c) and 5.4 (d) are of interest here. The PCSS reached trap filled saturation voltage at around 1300 Volts, the flow lines expands signaling the onset of double injection. Following this maximum conduction process at 1100 V, a decrease in flow occur at higher bias due to current crowding at the anode.

The orientation of the electric field at different voltages throughout the PCSS is studied and shown in Figure 5.5.

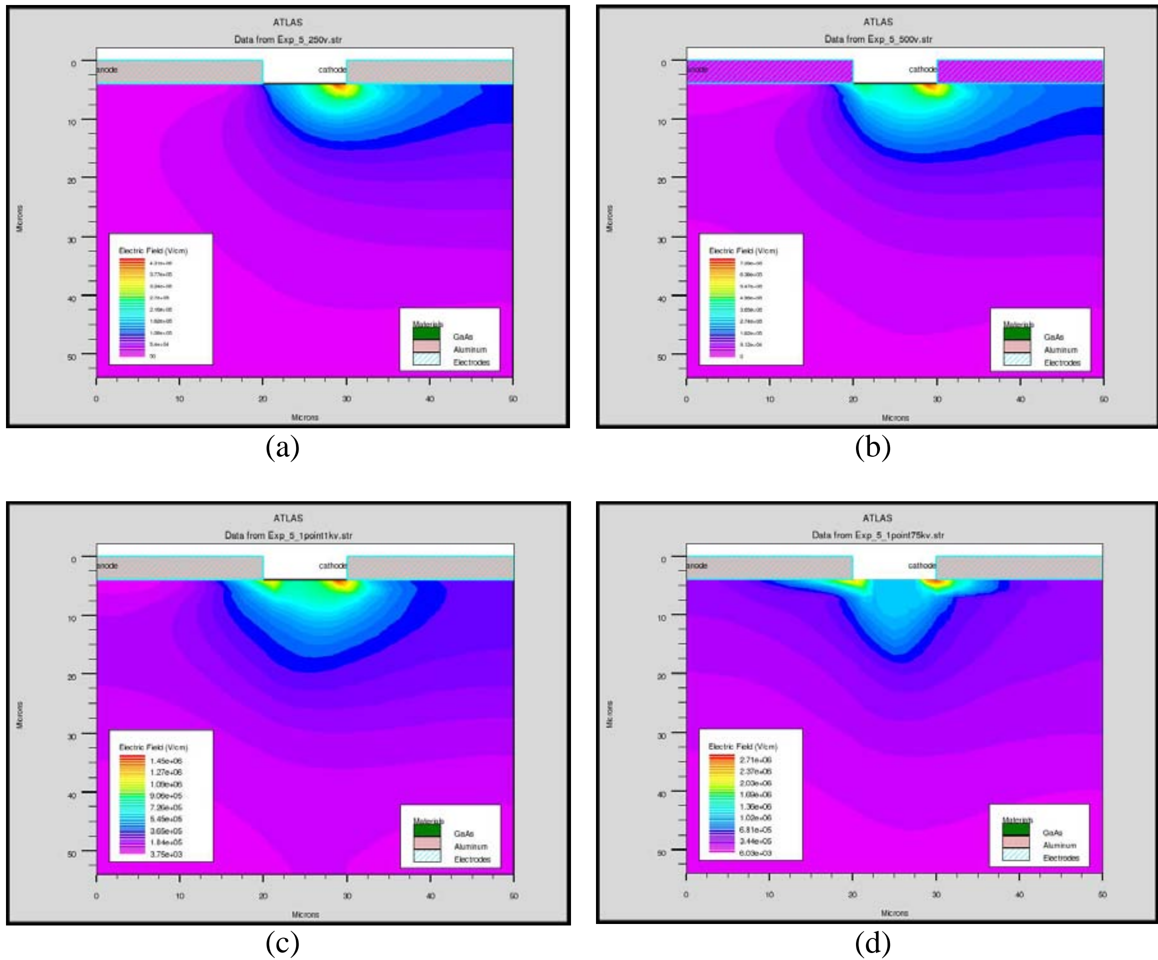

Figure 5.5: Showing the Electric field across the LT-GaAs PCSS at (a) 250 V, (b) 500V, (c) 1100 V and (d) 1750 V respectively.

As expected, increase in bias voltage results in an increase in the electric field across the electrodes. Charge accumulations at breakdown results in a change in the electric field profile as shown in Figure 5.5 (d), which is in contrast to 5.5 (c) which shows very high electric field at the surface between the electrodes and also the electric field extends deep into the device regions rather being concentrated at the edges which can be seen in low bias conditions.

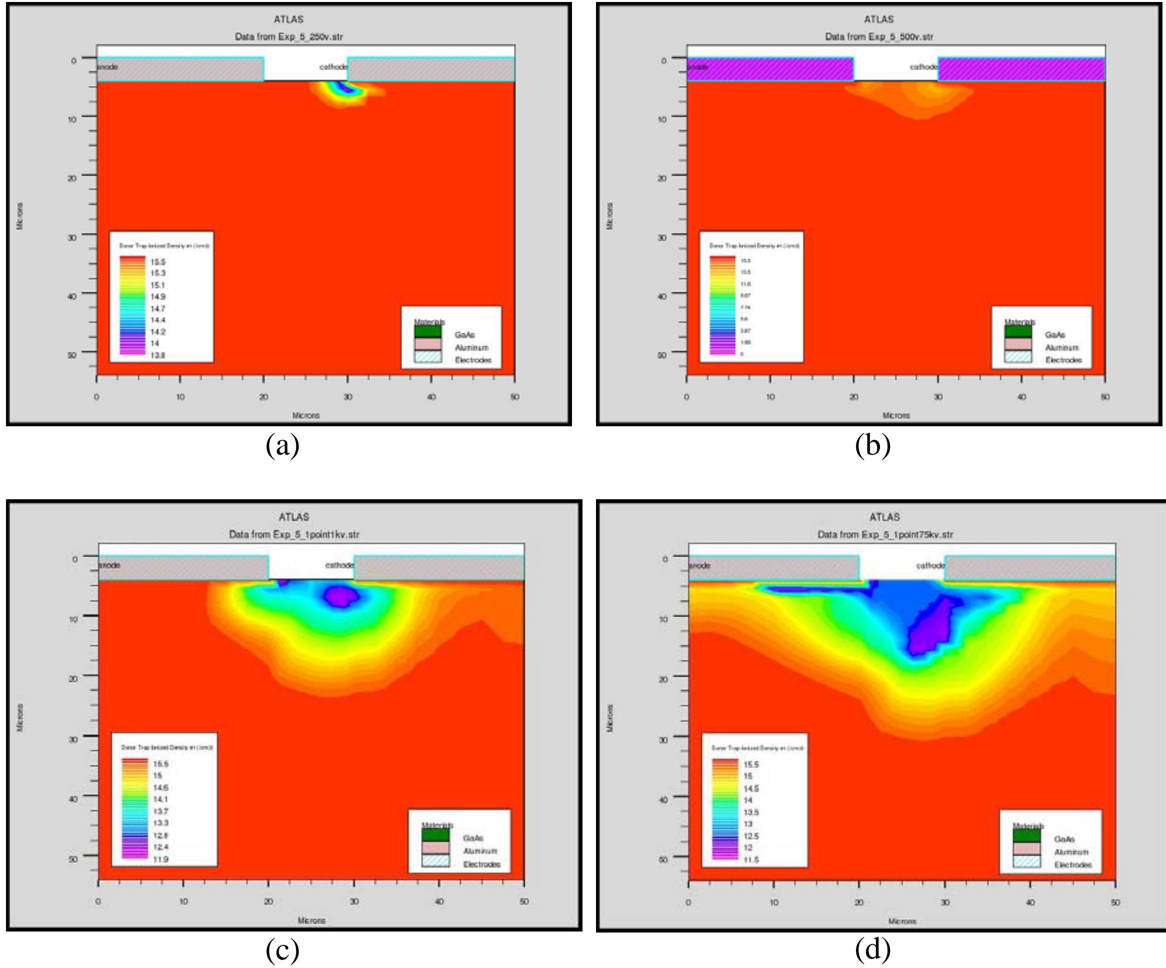

Figure 5.6: Showing the Donor Trap Ionized Density along the LT-GaAs PCSS at (a) 250 V, (b) 500V, (c) 1100 V and (d) 1750 V respectively.

Form the above Figure 5.6 the donor traps is all across the PCSS and there is a very little presence of the acceptor traps at lower bias voltages. As the bias voltage is increased the acceptor traps start forming on the surface and space between the electrodes. The heavy formation of acceptor traps between and the electrodes at higher bias voltages is being observed. In fact the formation acceptor traps can be seen right below electrodes when the PCSS is subjected to 1750 Volts. This formation of acceptor traps means that most of the recombination is taking place at those particular sites.

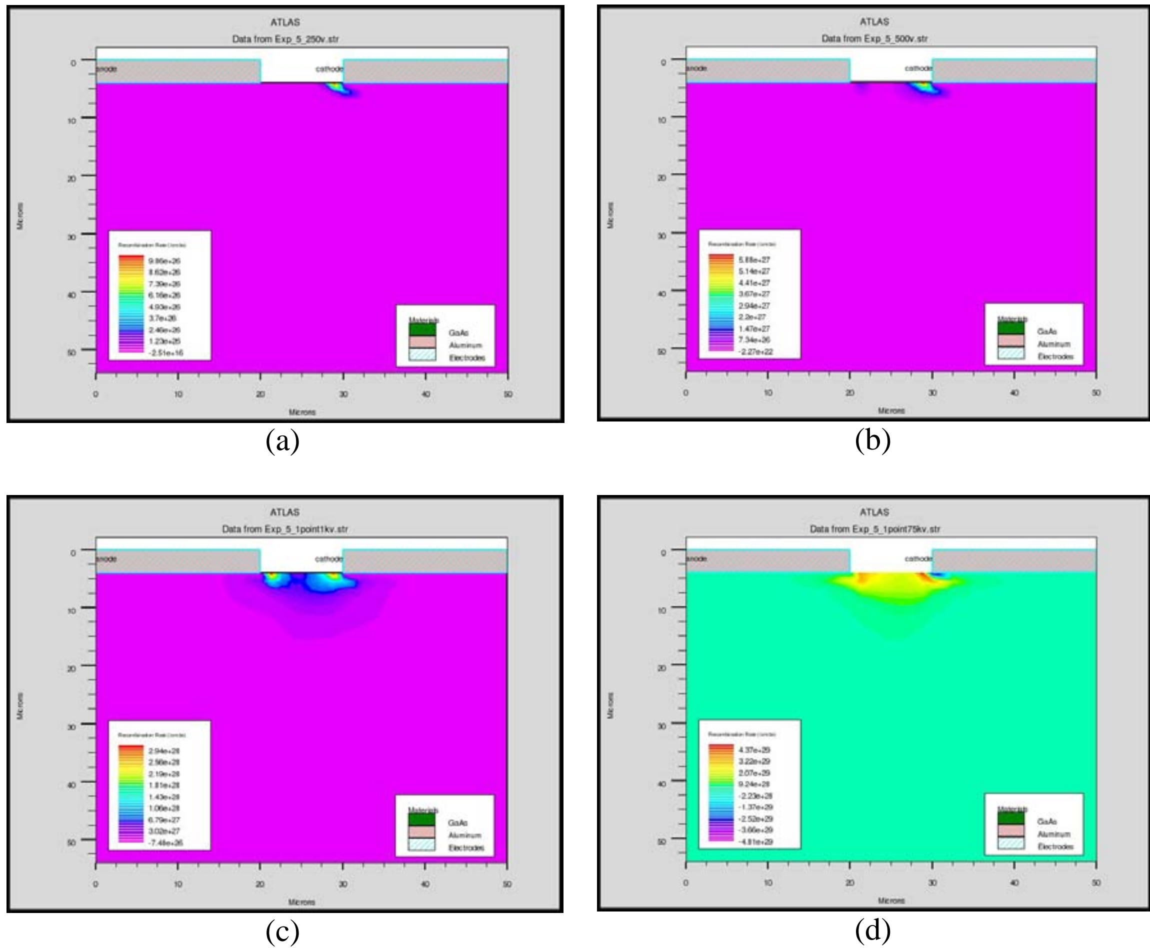

Figure 5.7: Shows the recombination rate at (a) 250 V, (b) 500V, (c) 1100 V and (d) 1750 V respectively throughout the LT-GaAs PCSS.

From Figure 5.7 it can be seen that the recombination rate is the highest at 1100 V which is also the onset of two carriers transport process in the device. The rate is now slightly higher at the cathode because of the increase in carriers following the onset of double injection. At breakdown i.e. at 1750 Volts the recombination is slightly lower at the cathode as a result of self-shielding. Thus it can be inferred that the PCSS has the breakdown voltage at 1300 V and at 1100 V the double injection phenomenon starts. As mentioned in section 5.1 it would give optimum results to operate the PCSS at 1100 V. The PCSS was calculated for its initial condition and then was subjected to bias voltage

which was ramped up to 1100 volts. Then the PCSS was illuminated with a laser beam. The chosen wavelength of the beam was 0.78 micrometers and the peak beam intensity was 50 M-Watt/ square cm. The source of the laser is directly perpendicular above the PCSS and was illuminated across the whole of PCSS. The laser was incident on the PCSS for 100 femtoseconds with zero intensity. Then the laser was made to illuminate on the PCSS with a beam intensity of 50 MW/sq cm for a period of 350 femtoseconds and then again the PCSS was again illuminated with zero intensity laser beam for a period of 300000 femtoseconds. The beam that was illuminated on top of the PCSS is given hereby:

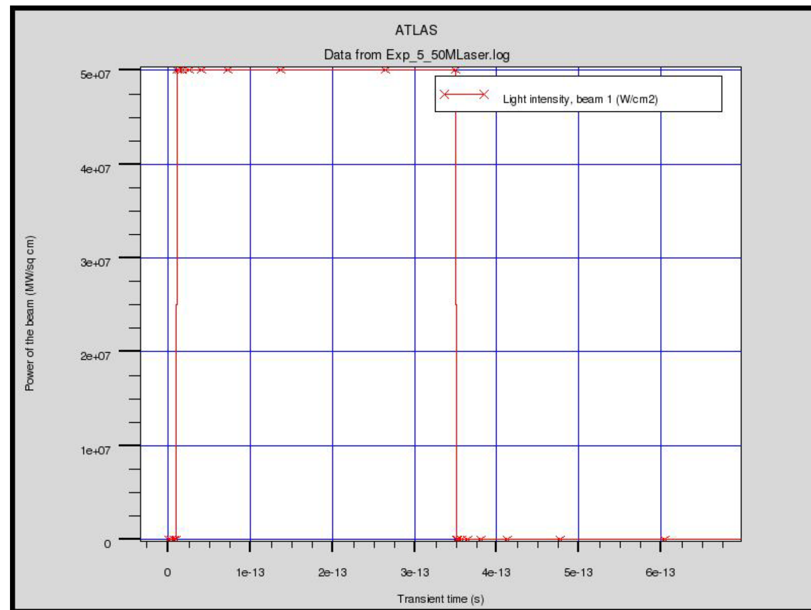

Figure 5.8: The beam illuminated on the PCSS.

From the figure 5.9 it can be seen that the conduction current density is the highest near the cathode since with the onset of two carrier injection at the given bias voltage, the excess generated carriers are accelerated towards electrodes. The Electric filed is also very high at the active region which enables a very high conduction current.

The majority of the conduction is happening on the surface of the active region which is between the cathode and the anode.

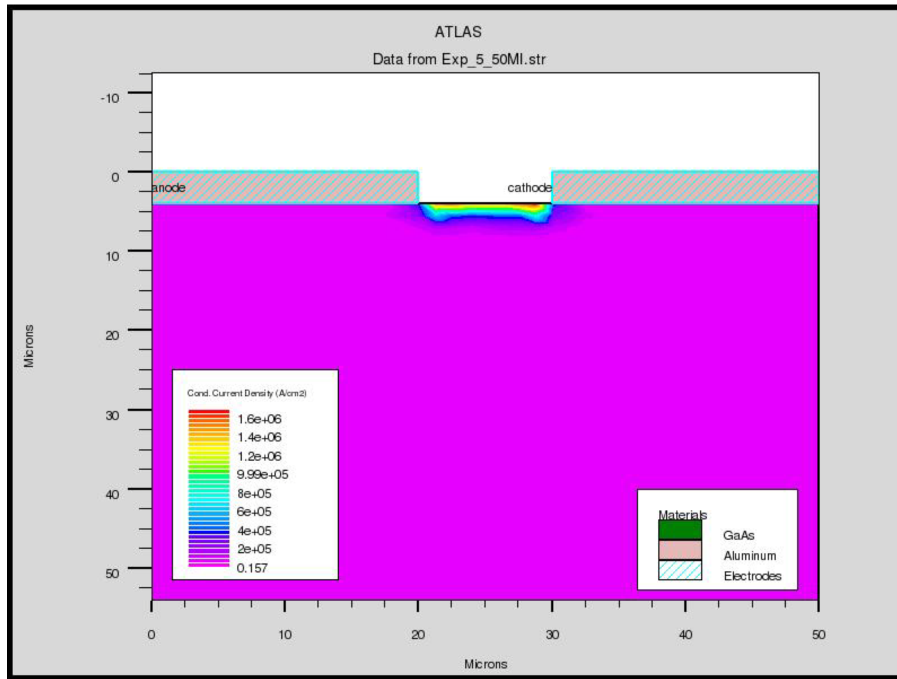

Figure 5.9: The conduction current density of the LT-GaAs PCSS while the same is illuminated with a 50 MW/sq cm beam of wavelength 0.78 micrometers.

From the Figure 5.10 it can be observed that during the photo generation of excess carriers at 1100 V also produces a high concentration of acceptor traps near the cathode. Thus the recombination phenomenon is also very high in the vicinity of the cathode but not as high as during or above the breakdown voltage. In fact the formation of the acceptor traps is the highest just below the cathode. It can be also seen that the concentration of the acceptor traps is significantly lower near the anode. Thus the anode captures most of the generated carriers which in turn gives required photocurrent. From Figure 5.11 it can be seen that the Electric field is also very high near the electrodes. The Electric field is the highest near the cathode edge facing the active region. The Electric

field is the highest at the surface and slowly diminishes along the depth of the PCSS. The Electric field is also spread more towards the cathode than towards the anode.

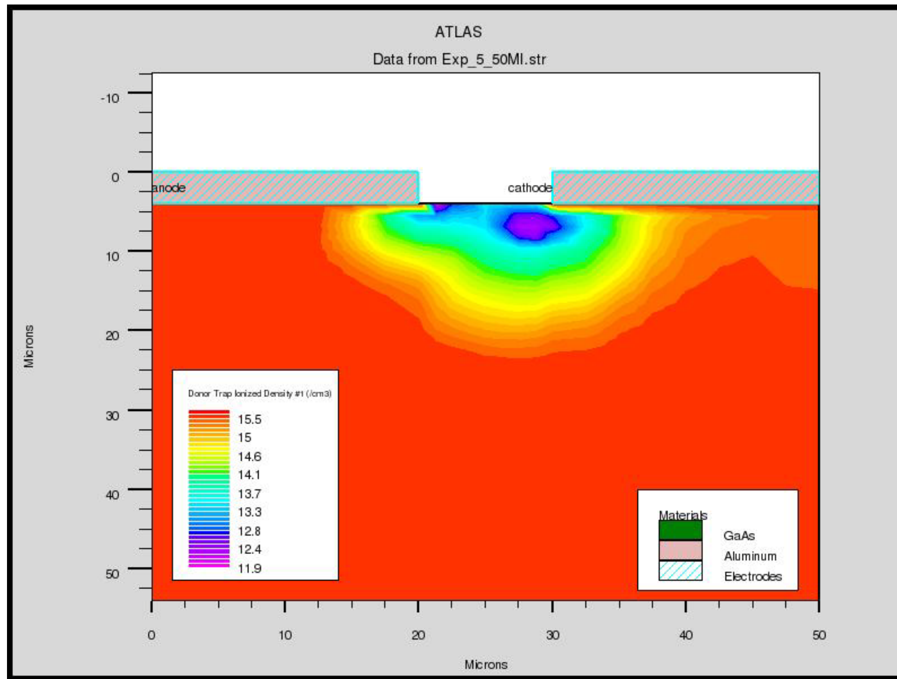

Figure 5.10: Shows the donor trap density of the LT-GaAs PCSS while the same is illuminated with a 50 MW/sq cm beam of wavelength 0.78 micrometers.

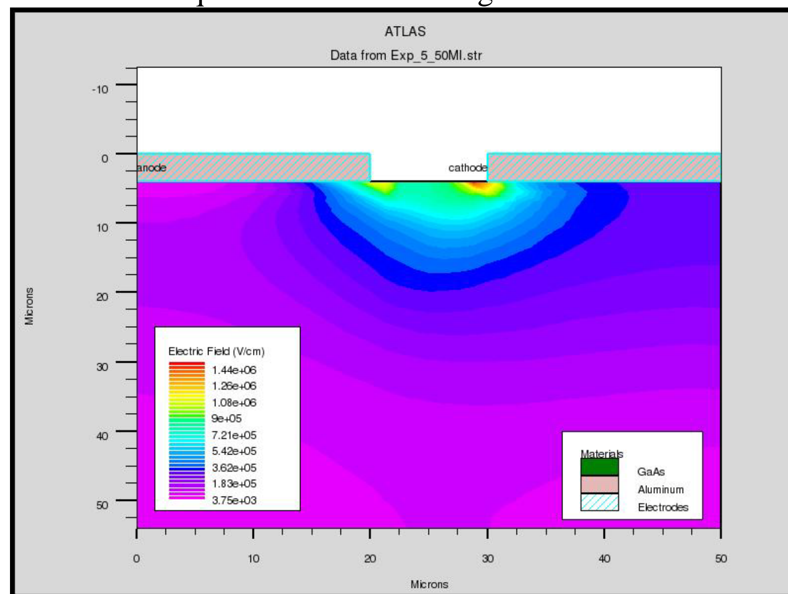

Figure 5.11: Shows the electric field across the LT-GaAs PCSS while the same is illuminated with a 50 MW/sq cm beam of wavelength 0.78 micrometers.

From the Figure 5.12 it can be observed that current flow lines are the highest near the cathode. During photo generation of excess carriers the formation of the acceptor traps near the cathode is the highest and the majority of the recombination happens at this site.

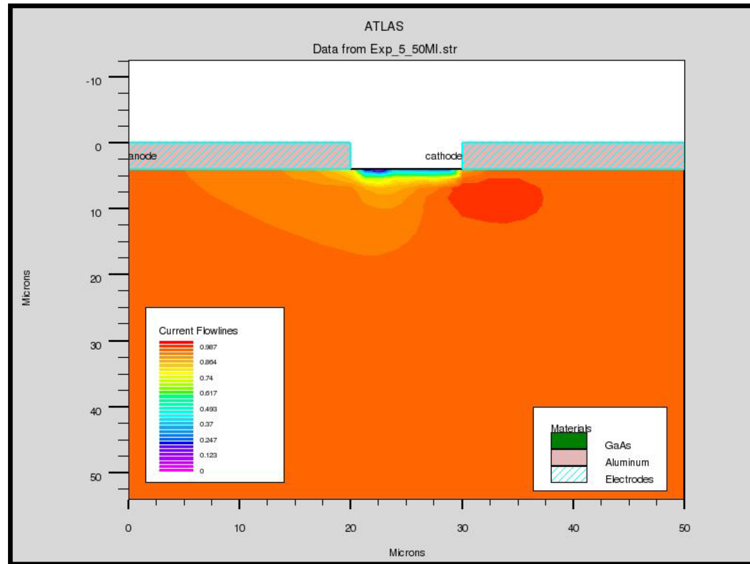

Figure 5.12: Shows the current flow lines across the LT-GaAs PCSS while the same is illuminated with a 50 MW/sq cm beam of wavelength 0.78 micrometers.

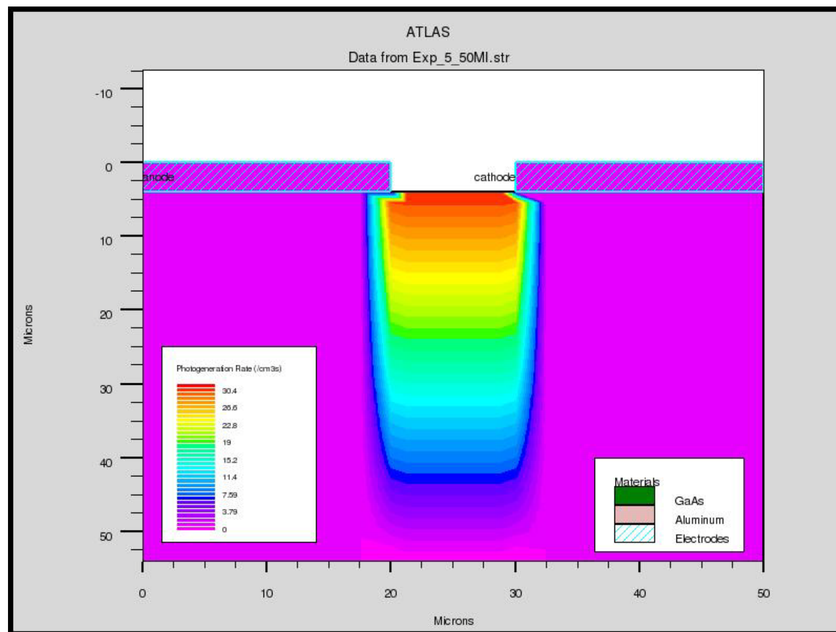

Figure 5.13: Showing the Photo generation rate across the LT-GaAs PCSS while the same is illuminated with a 50 MW/sq cm beam of wavelength 0.78 micrometers.

From Figure 5.13 it can be observed that the photo generation of electrons is maximum at the surface which is in the range of 30.4 /cm^3. The minimum is seen at the depth of 40 to 45 micrometers. Thus it can be inferred that the optical absorption depth of the LT-GaAs material is approximately about 45 micrometers.

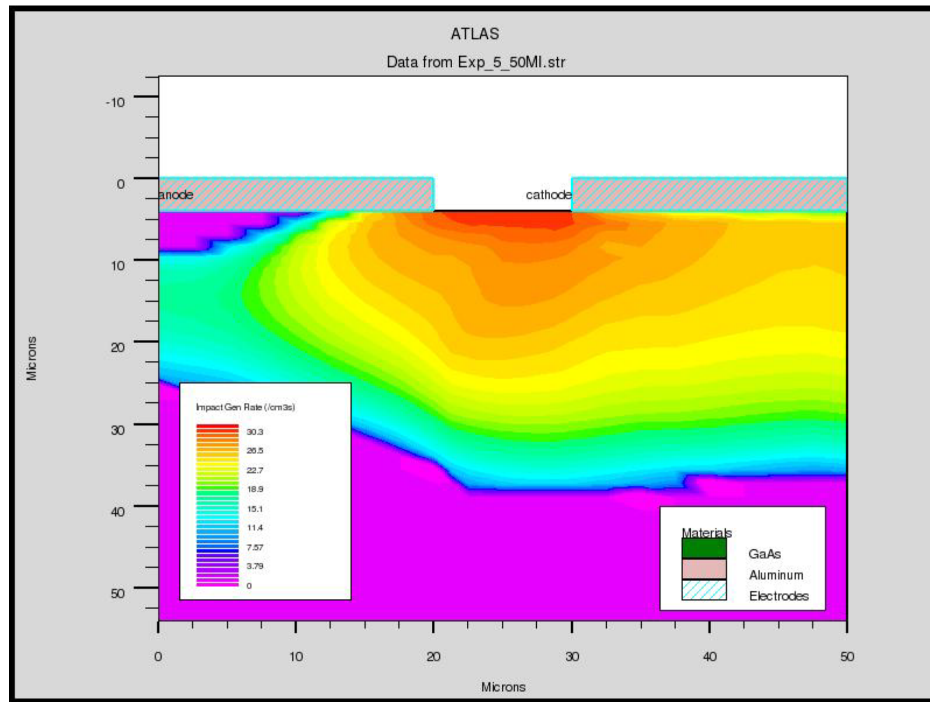

Figure 5.14: Showing the Impact generation rate across the LT-GaAs PCSS while the same is illuminated with a 50 MW/sq cm beam of wavelength 0.78 micrometers.

Thus from the above Figures 5.9 to 5.13 it can be observed that when the laser light is directly incident of the substrate of the LT GaAs PCSS, the photo generation rate is highest at the center of the switch on the substrate between the electrodes. The electric field is also highest between the contacts of the LT GaAs PCSS. The conduction current density is concentrated between the electrode edges. From Figure 5.14, it can be seen that the impact generation rate is the highest between the electrodes and the rate diminishes as the beam passes across the optical absorption depth.

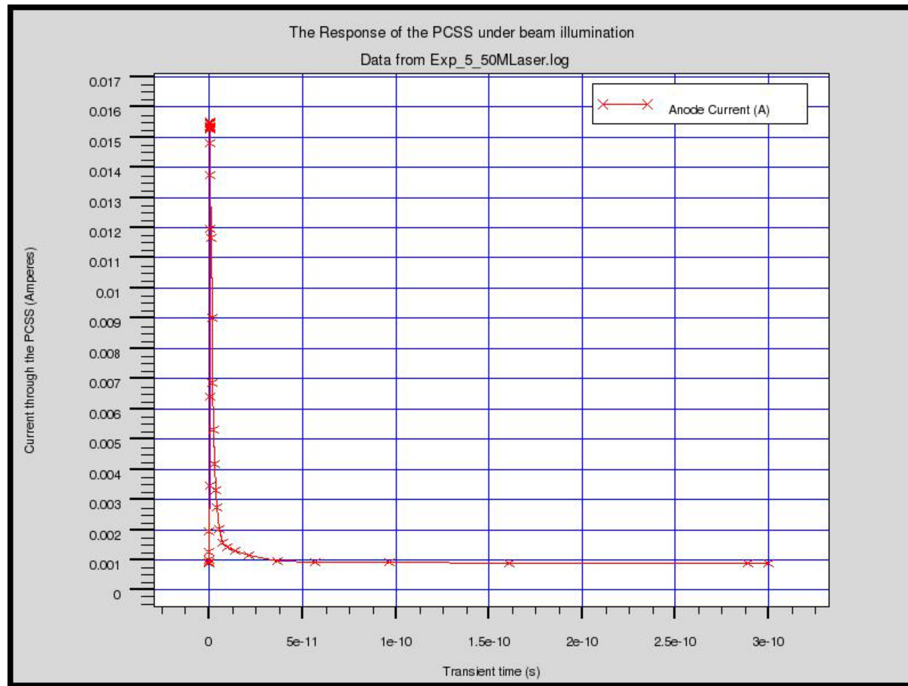

Figure 5.15: The current through the PCSS Vs the Transient time when the LT GaAs PCSS is subjected to 350 femtoseconds laser pulse.

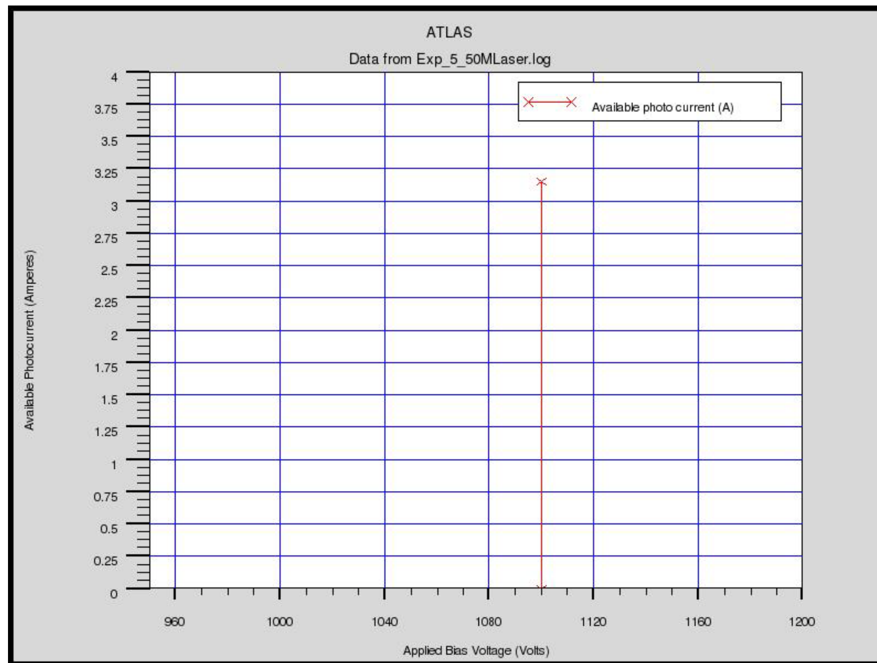

Figure 5.16: Available photocurrent generated throughout the experiment.

From Figure 5.15 and Figure 5.16 it is observed that an electrical pulse is being generated when the PCSS is subjected to the 350 femtoseconds laser pulse. The generated

electrical pulse has a width in the order of 10^{-12} seconds. The rise time of the electrical pulse was used to calculate the frequency of the generated electrical pulse. In general the time required by the electrical pulse to go from 10 % to 90% of the maximum signal amplitude is considered to calculate the rise time.

From the Figure 5.24 below we see that the electrical pulse start rising linearly from 0.25 X 10^{-13} seconds where the signal amplitude is 10 % of the maximum amplitude (= 0.0015 Amps) to 3X10^{-13} seconds where the signal amplitude is 90 % of the maximum current (=0.0139 Amps). Thus the rise time is calculated as:

$$3\ X\ 10^{-13} - 0.25\ X\ 10^{-13} = 2.75\ X\ 10^{-13}\ seconds \tag{5.1}$$

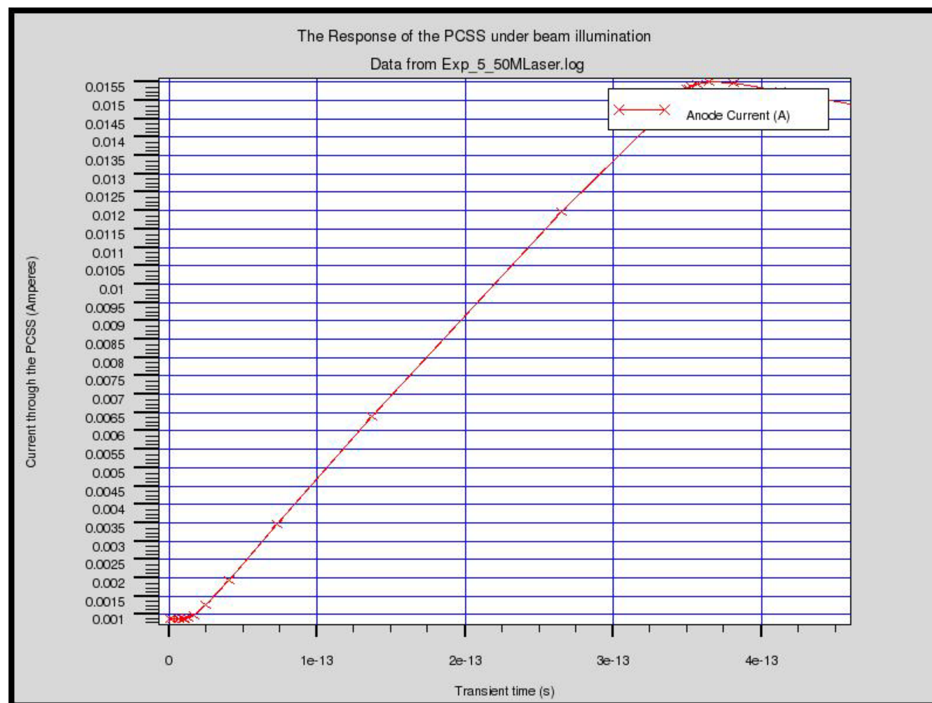

Figure 5.17: The rise time of the electrical pulse generated from the LT GaAs when subjected to 350 femtoseconds laser beam.

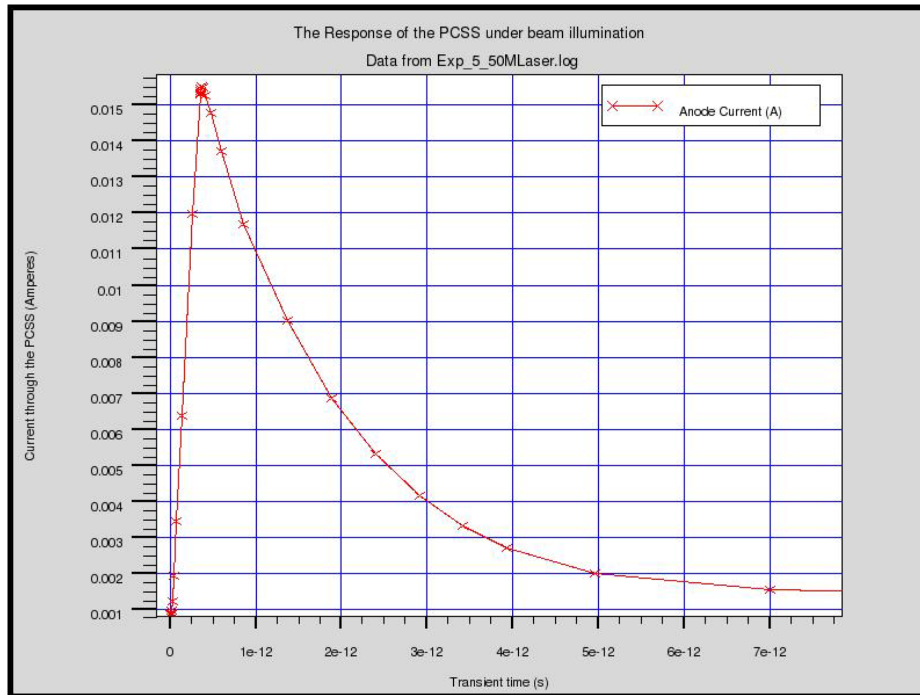

Figure 5.18a: The pulse width of the generated pulse from the Photoconductive emitter when subjected to 0.78 micrometers wavelength laser beam under the bias voltage of 1100 V.

Figure 5.18a shows the photoconductive current generated by the switch when a 0.78 micrometers laser pulse, of duration 350 femtoseconds, is incident on the active region. Here the total pulse length can be considered as 7 picoseconds and the rise time is about 2.75 femto seconds, with a hold off time is nearly 0.01 picoseconds and the fall time is 4.5 picoseconds.

The frequency was determined by converting the time domain signal to frequency domain signal, shown in Figure 5.18b.

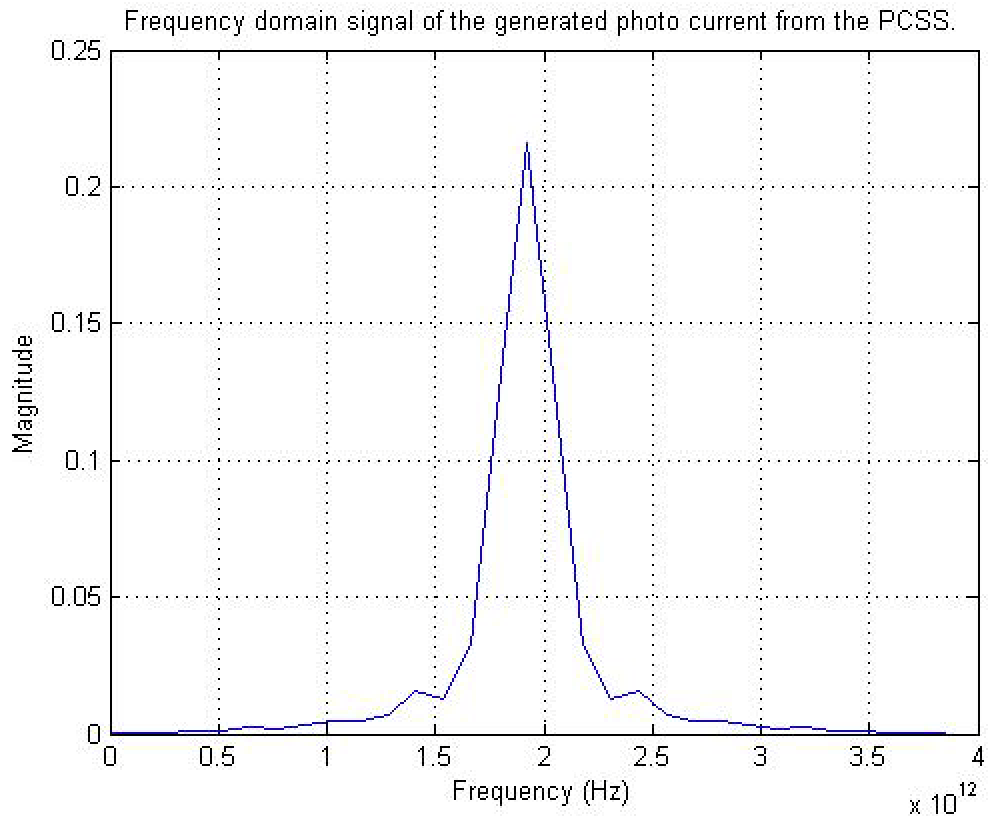

Figure 5.18b: The Frequency domain signal of the generated photo current from PCSS.

As can be seen, the maximum frequency is attained at approximately 1.75 THz with the peak magnitude of nearly 0.22. These pulse parameters were chosen to generate the excitation signal for the photoconductive emitter or antenna.

MICROWAVE STUDIO SIMULATIONS: Antenna Analysis

5.2 The Results for the Antenna Simulation

After that the THz pulse was generated and analysis was done for the shape of the generated electric pulse, the same pulse width, rise time, hold time and fall time was used as the excitation signal for the antenna.

As mentioned in the previous chapter ACMSA have been simulated with different kind of slots. The S11 parameter for the Antenna was studied which signifies the Return

Loss of the antenna. The Return Loss is the measure of how close the actual input impedance of the network is to the nominal system impedance value. It actually calculates the power that is being reflected back from the antenna. The results for different ACMSA designs were also compared. The results from the simulation were analyzed using the following parameters:

- Farfield Pattern and Power radiated.
- The Directivity
- The Gain
- The Electric field.

The below given Figure 5.19 shows the frequency response of the basic dipole antenna. The antenna has a rectangular patch whose orientation is parallel to the microstrip line. The dimension of the patch is 50 μm by 20 μm.

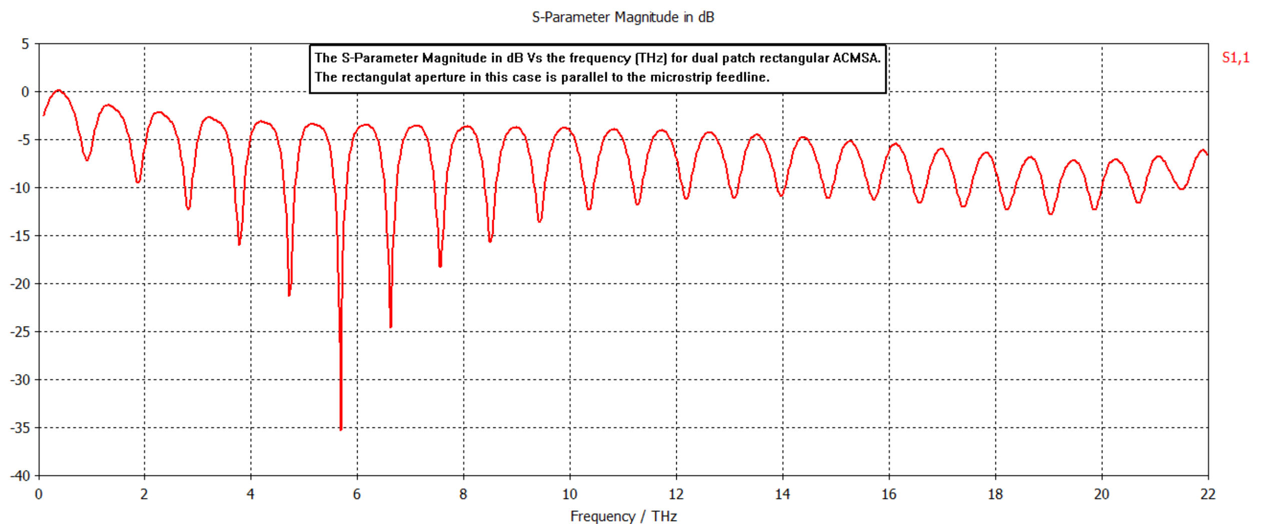

Figure 5.19: The S11 magnitude (dB) Vs the frequency (THz) for a dual patch rectangular ACMSA.

From Figure 5.19 it can be observed that the antenna has multiple resonant frequencies in which it can operate. Only the resonant frequencies which are below -10

dB were considered. The resonant frequency was chosen to be at 5.6845 THz. Thus we can see that this antenna has multiband property. But the bandwidth of the antenna is low.

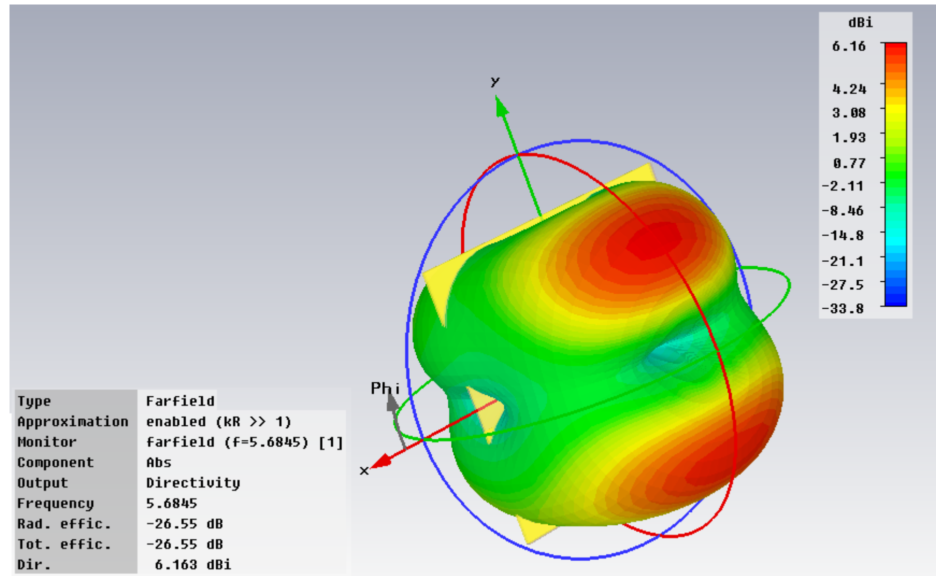

Figure 5.20: The Farfield Pattern for the rectangular dipole MSA.

Figure 5.26 and Figure 5.27 shows the Farfield radiation pattern at 5.6845 THz, and from the figures can be seen that the there is very high back radiation from the antenna. The main lobe is being divided into two lobes, thus making the other lobe to be treated as noise. The goal is to incorporate the side lobe into the main lobe and eliminate the back lobes, which in turn it can increase the directivity and gain of the antenna. The Farfield directivity was found out to be 6.16 dB in the Z direction. The 3 dB angular width for the lobe was found to be 36.9 degrees. The back lobe and the side lobes are as high as -15 dB.

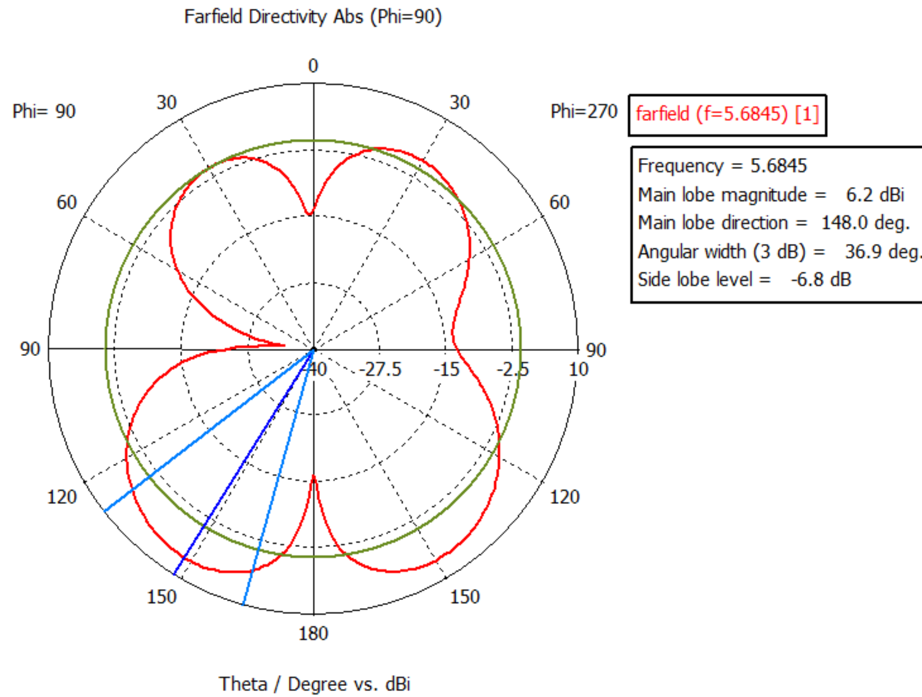

Figure 5.21: The Farfield directivity of the antenna.

The Gain and E-field of the dipole antenna is shown in the Figure 5.22 and 5.23 respectively. Gain is the product of the directivity and the efficiency factor. The efficiency factor is very low in this case since the total area subtended by the main lobe is significantly lower than combined area of the side lobe and the back lobes. Thus the stray factor for this dipole antenna is very high. The E-field for the dipole antenna is -5.6 dB-V/m, which is significantly low for any practical use.

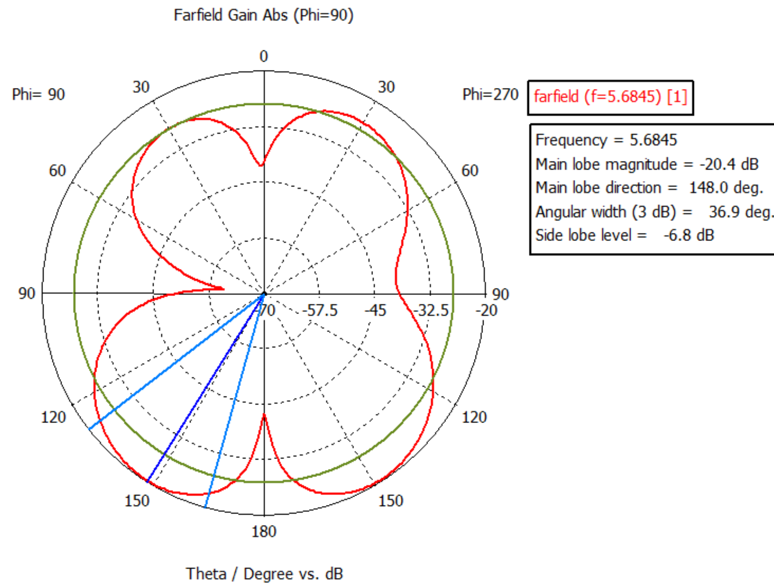

Figure 5.22: Farfield Gain for the antenna.

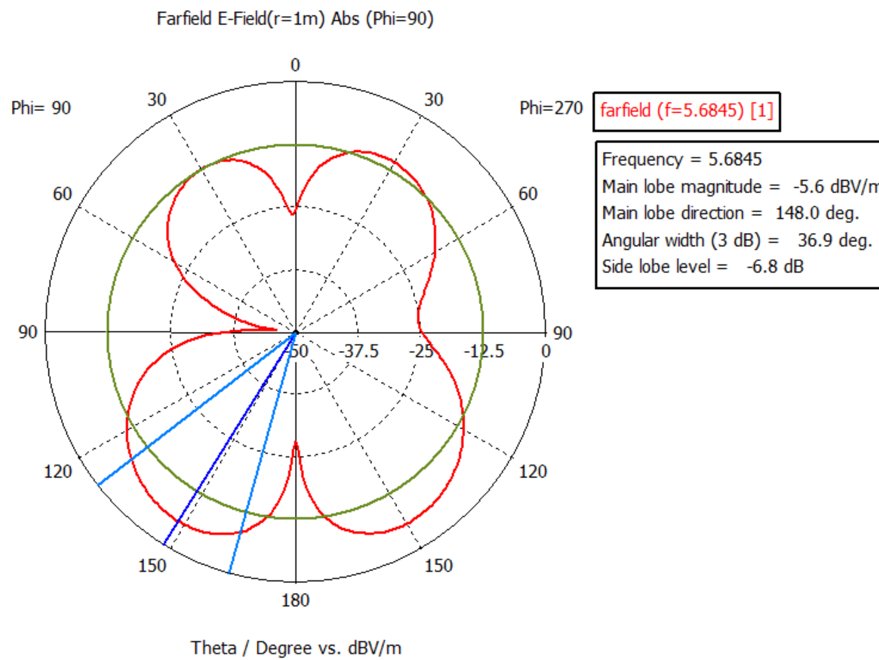

Figure 5.23: The Farfield Electric field for the antenna.

Figure 5.24 shows the S11 parameter for a dipole antenna with a rectangular aperture of 10 µm X 20 µm which is oriented perpendicular to the microstrip line on the bottom substrate.

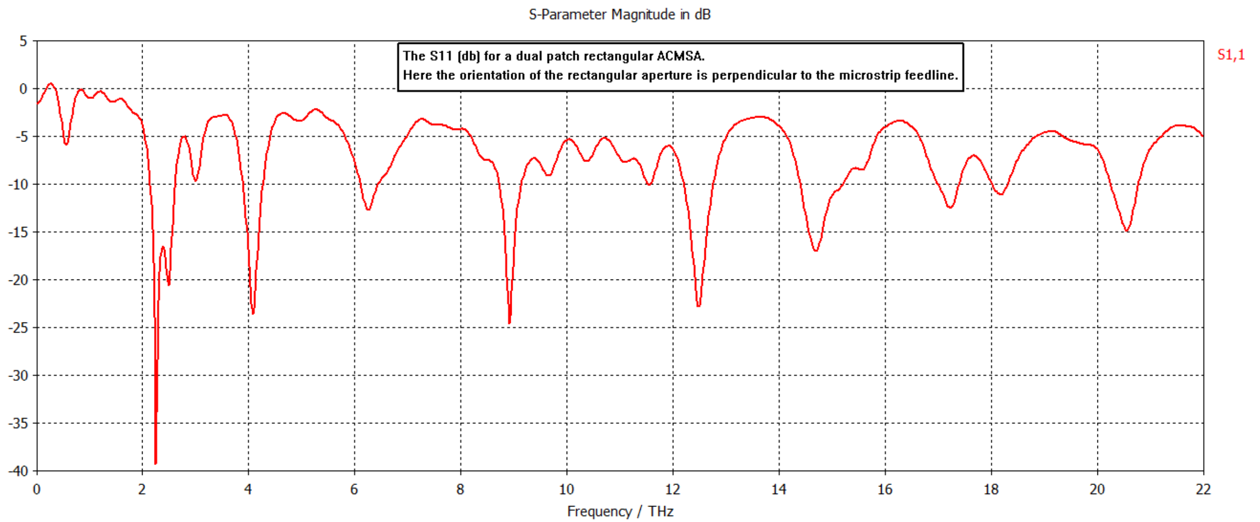

Figure 5.24: The S11 magnitude (dB) Vs the Frequency (THz) response of the dual rectangular patch rectangular ACMS.

From the Figure 5.24 it can be observed that there are multiple resonant frequencies that this antenna can operate. The return loss is the highest at 2.53 THz which is approximately -40 dB in magnitude. Thus it is eminent that the farfield should be studied for this antenna at 2.53 THz.

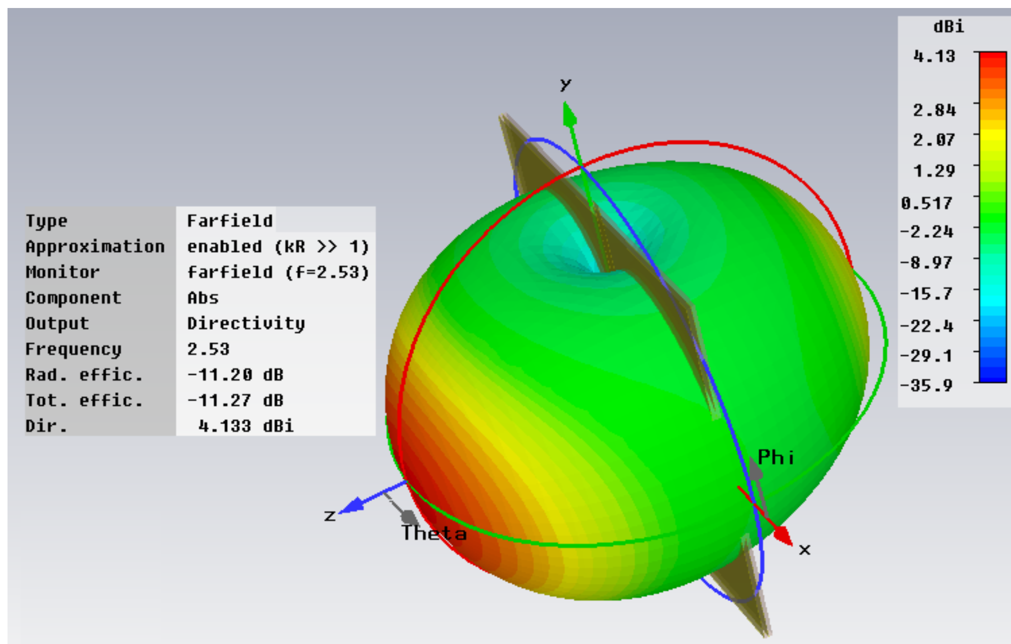

Figure 5.25: Farfield plot for a rectangular Dipole Rectangular Aperture Coupled MSA.

From the farfield Figure 5.25 it can be inferred that there is a slight improvement of the radiation pattern for this antenna over the previous one. The side lobes are incorporated in the main lobe. But the efficiency is very low for this antenna since the back radiation is substantially high and it is nearly equal to main lobe radiation. The radiation efficiency was -11.20 dB compared to the previous case which was -26.55 dB. The directivity is found out to be 4.133 dBi compared to the previous case of 6.163 dBi.

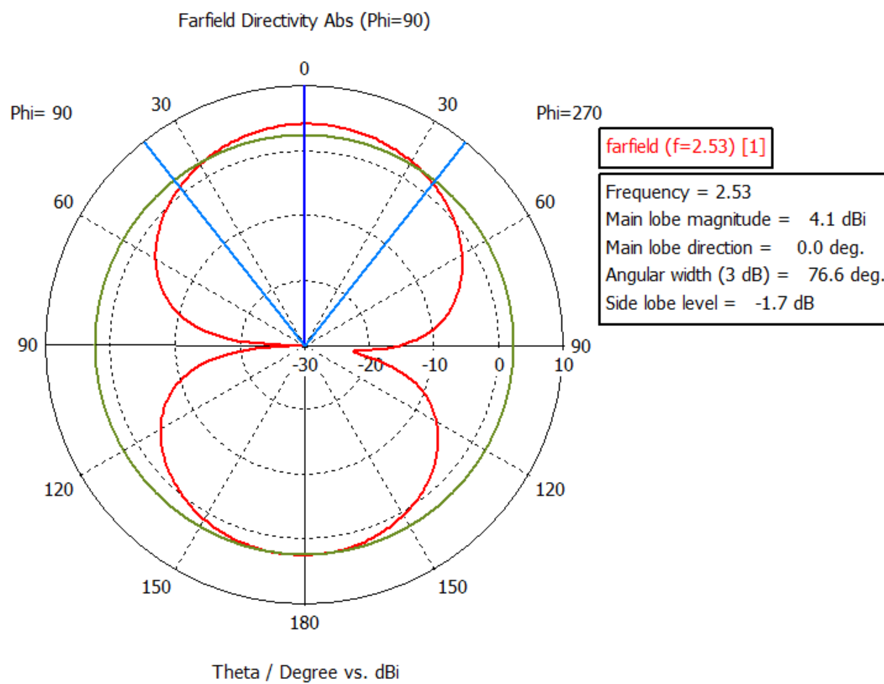

Figure 5.26: The Farfield directivity of the beam radiated from the ACMSA.

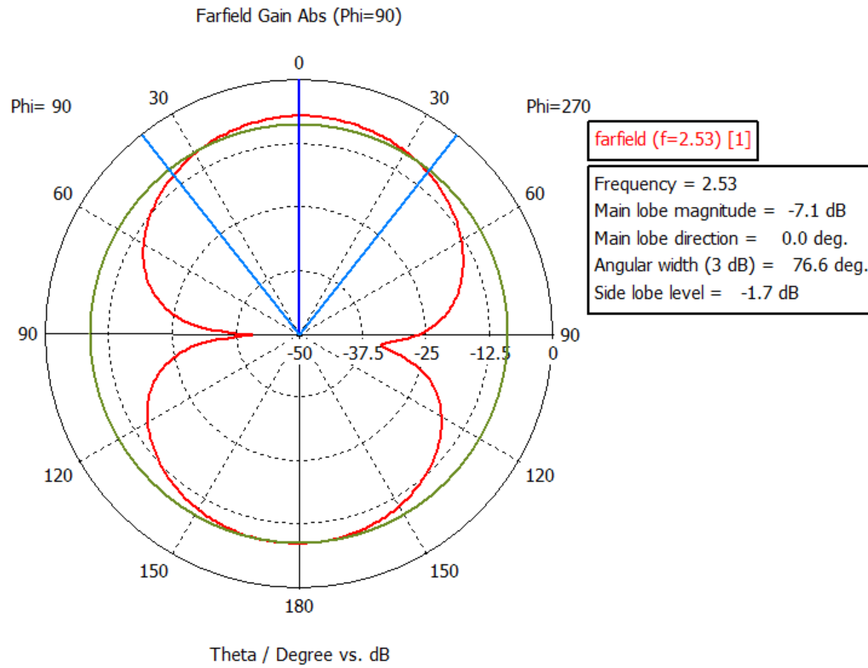

Figure 5.27: The Farfield Gain for the ACMSA at 2.53 THz.

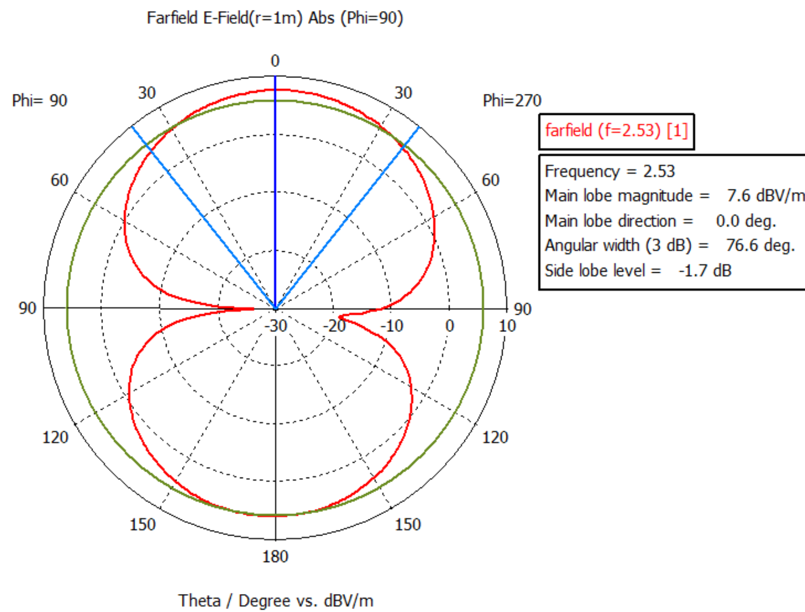

Figure 5.28: The Electric field of the ACMSA at 2.53 THz.

From the above two Figures 5.26 and 5.27 it can be seen that the rectangular ACMSA has a maximum gain of -12.5 dB. The maximum Electric field achieved for this type of antenna is approximately 7 dB-V/m. From the Figure 5.26 it can be seen that the

maximum directivity is in 0 ° and has a peak magnitude of nearly 4 dBi. Thus it can be said that though the antenna with a rectangular aperture showed marked improvement over the previous one but it has a very high the back to front radiation ratio. Thus the aperture of the previous antenna was changed to circular aperture to see the S11 response and the farfield pattern of the new a rectangular patch circular aperture coupled microstrip antenna.

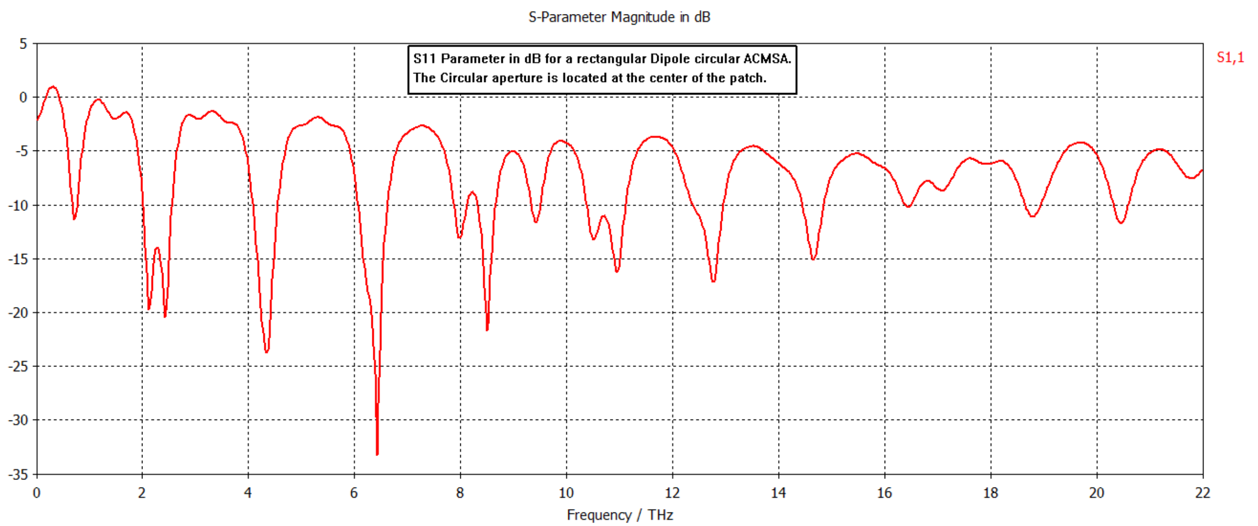

Figure 5.29: S11 Parameter in dB Vs the Frequency for a rectangular Dipole Circular Aperture Coupled MSA.

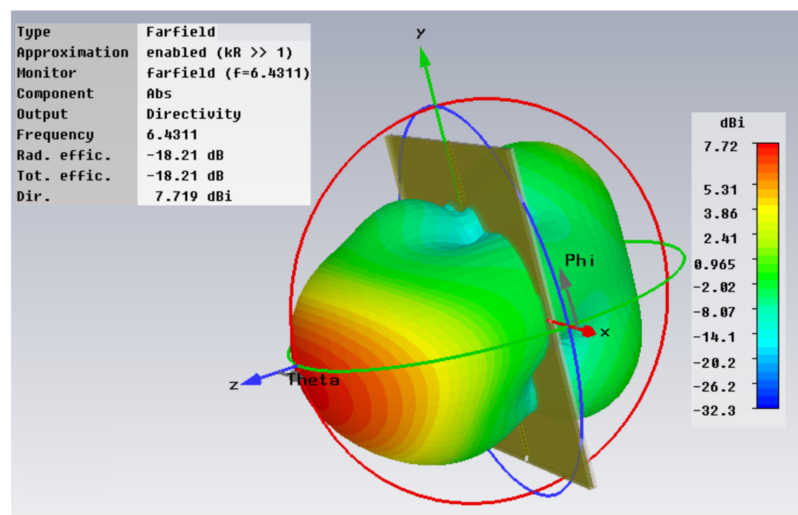

Figure 5.30: Farfield plot for a rectangular Dipole Circular Aperture Coupled MSA.

From the Figure 5.29 it can be observed that there are multiple resonant frequencies that this antenna can operate. The return loss is the highest at 6.43 THz which is approximately -35 dB in magnitude. From the Figure 5.30 it can be observed that there is presence of no side lobes, but the back radiation is significantly high as -2.5 dBi for 6.43 THz. From the Figure 5.31, Figure 5.32 and Figure 5.33 it can be seen that the peak directivity is 7.719 dBi, the peak gain is -10.5 dB and the peak electric field 4.3 dB-V/m respectively for the frequency of 6.43 THz.

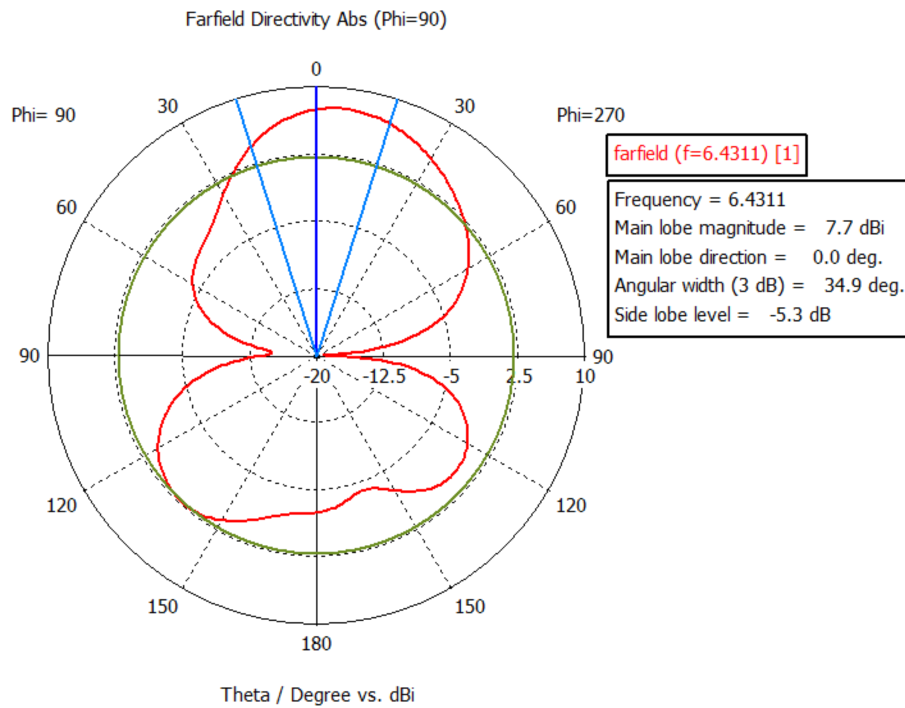

Figure 5.31: Directivity plot for a rectangular Dipole Circular Aperture Coupled MSA.

Thus it can be inferred that the though there is an improvement in the radiation pattern for the circular aperture MSA over the rectangular aperture MSA over the back radiation. But still the back radiation is too high to be considered to be viable for practical use. Thus having a circular aperture gave better results initially, but there is no significant improvement considering the directivity and the gain of the antenna. Thus the patch is

now changed to triangular shape, and the aperture was kept circular same as before and the antenna parameters were investigated.

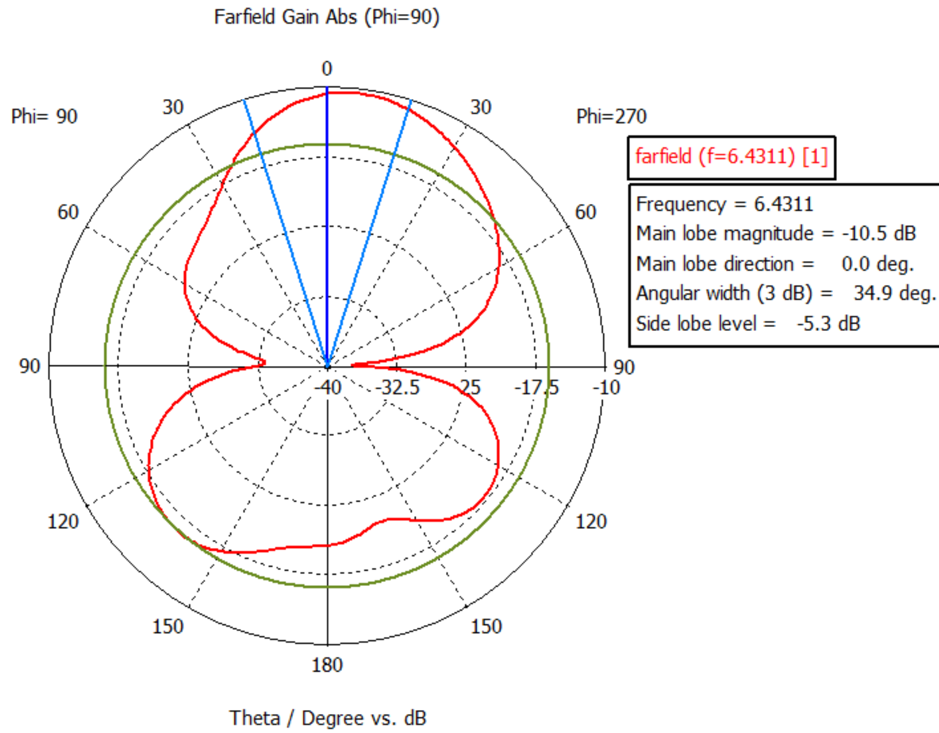

Figure 5.32: Gain plot for a rectangular Dipole Circular Aperture Coupled MSA.

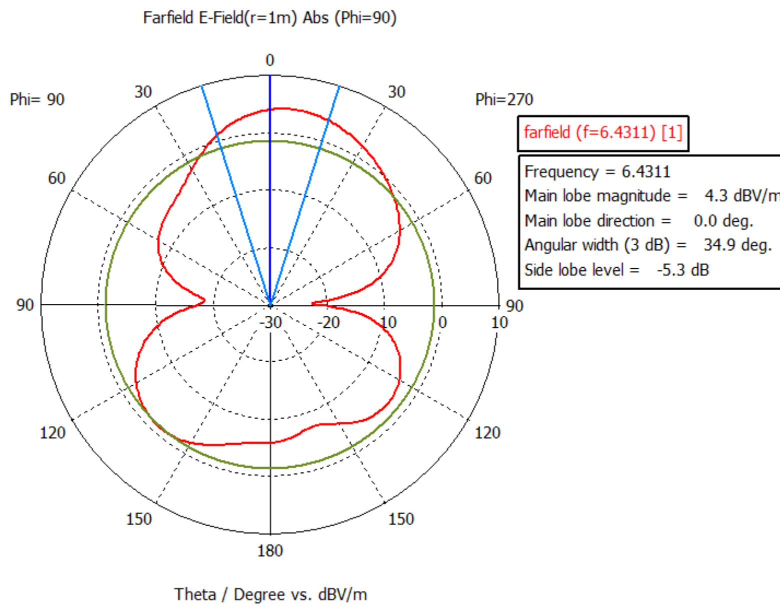

Figure 5.33: E-field plot for a rectangular Dipole Circular Aperture Coupled MSA.

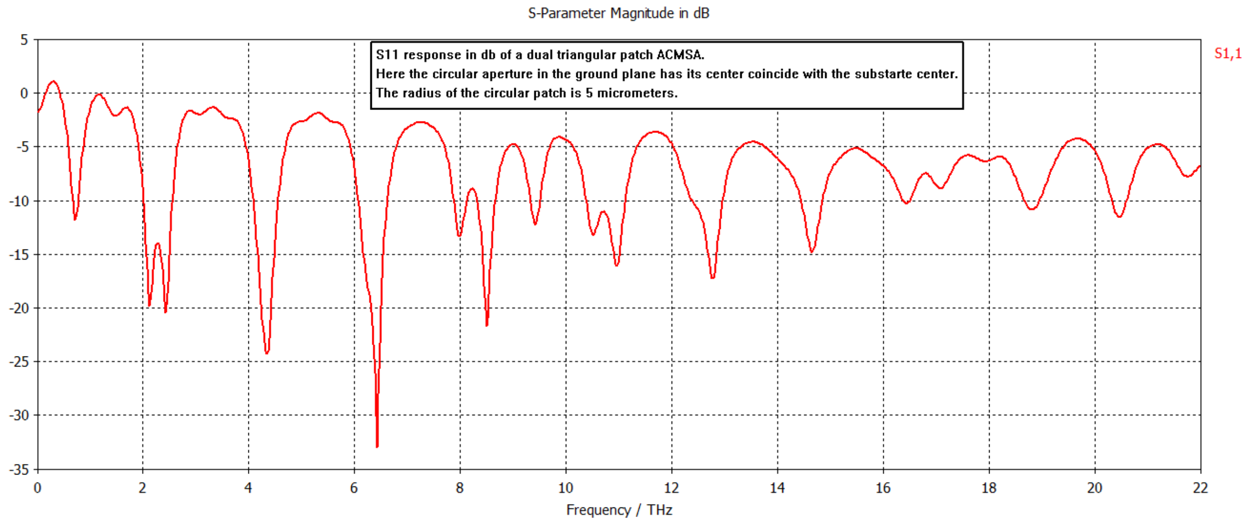

Figure 5.34: The S11 parameter in dB for dual triangular patch circular ACMSA

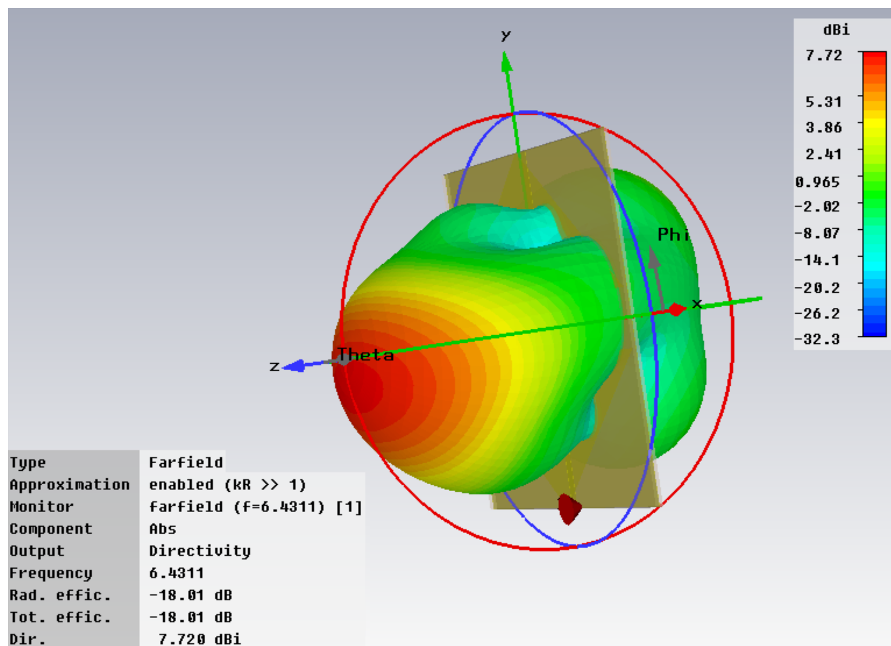

Figure 5.35: The Farfield Pattern for the triangular patch dipole circular ACMSA at 6.4311 THz.

From the Figure 5.34 it can be said that the antenna also can operate in multiple frequency windows. The peak return loss was approximately -35 dB and was found to be at 6.43 THz. Figure 5.35 shows the farfield pattern it can be seen that the there is no presence of side lobes unlike the previous case. But the back lobes for this antenna are

also significantly large. The directivity is 7.72 dBi with a radiation efficiency and total efficiency of -18.01 dB.

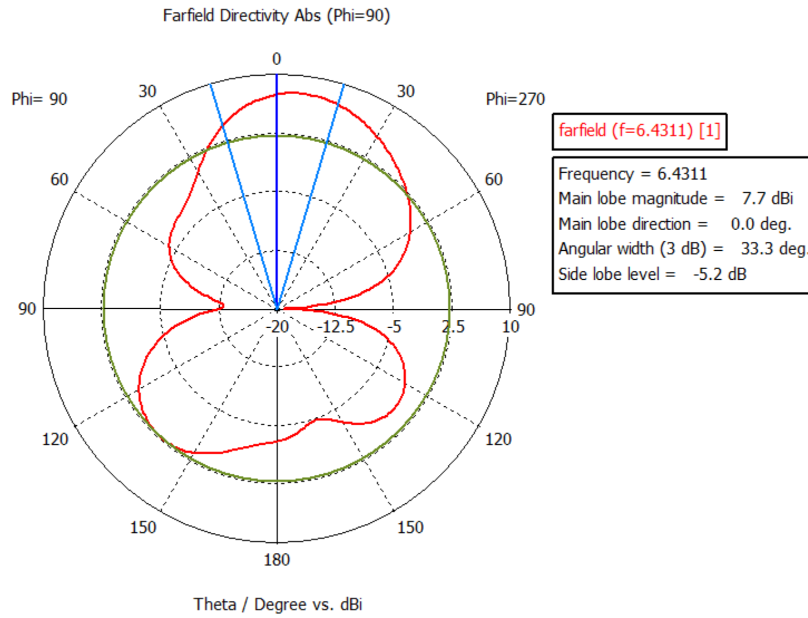

Figure 5.36: The directivity of triangular patch circular ACMSA at 6.4311 THz

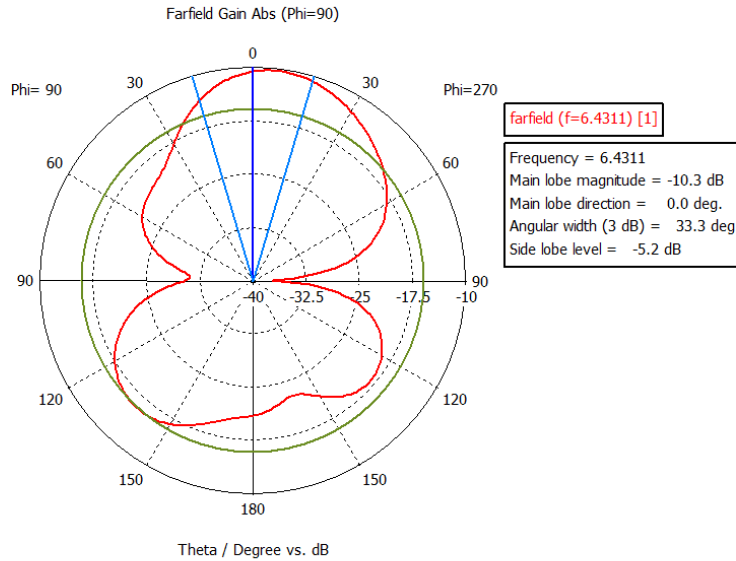

Figure 5.37: The farfield gain of the triangular patch circular ACMSA at 6.4311 THz

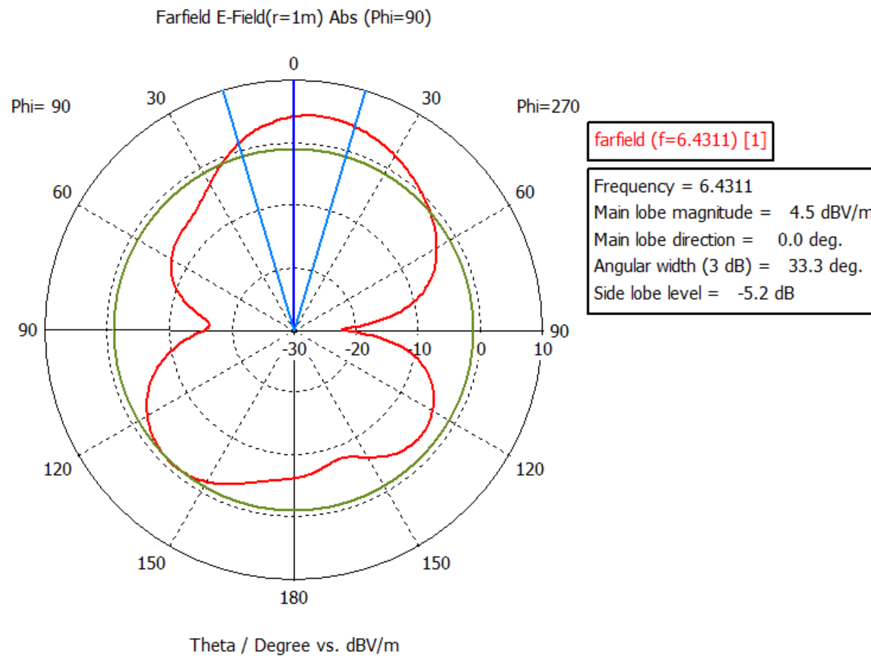

Figure 5.38: The Electric field for the triangular patch circular ACMSA at 6.4311 THz

Thus from the above Figure 5.36, Figure 5.37 and Figure 5.38, it can be seen that the farfield directivity of the dual triangular patch circular ACMSA at 6.4311 THz is better than the other designed ACMSAs. The maximum magnitude for the directivity is 7.72 dBi which is better than the previous case. The gain and the Electric field for this antenna are -10.3 dB and 4.5 dB-V/m respectively which have not changed significantly over the previous values. The next antenna that had been simulated had semicircular patches with circular aperture. The semicircular shaped patches have the diameter of 50 µm and were aligned centrally with the center of the substrate.

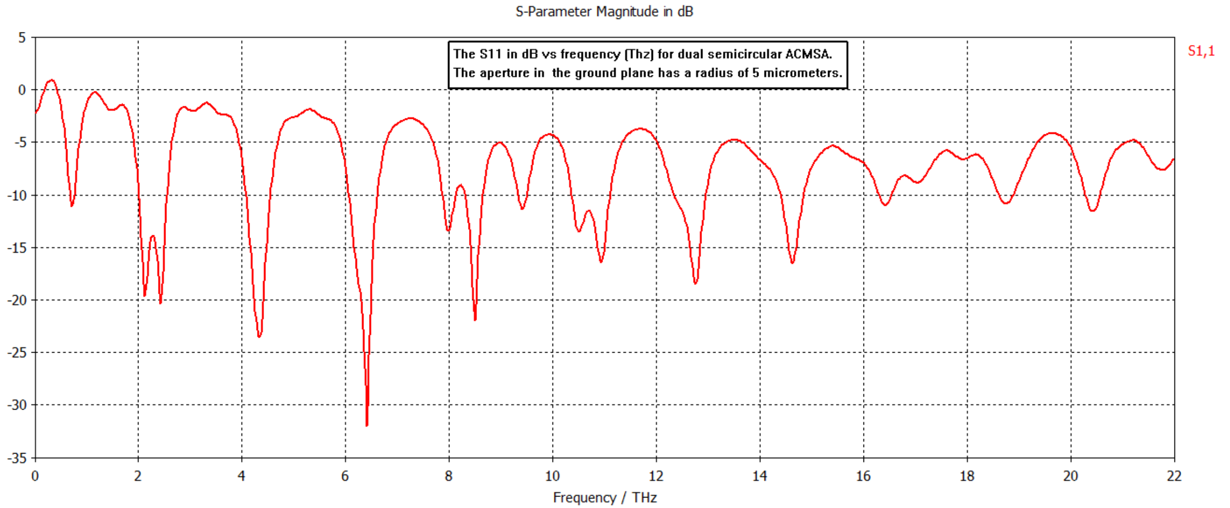

Figure 5.39: The S11 (dB) vs. frequency (THz) for the semicircular patch circular ACMSA

From Figure 5.39 we see that the dual semicircular patch circular ACMSA multiple frequency windows to operate. But comparing the S11 parameter for this semicircular patch circular ACMSA with the triangular patch circular ACMSA we see no significant difference in their frequency response. Though it is possible to get multiband response but the best response is being achieved at 6.43 THz and has a return loss of approximately -35 dB. This is same with the dual triangular patch antenna circular ACMSA where we consider 6.43 THz also as the resonant frequency.

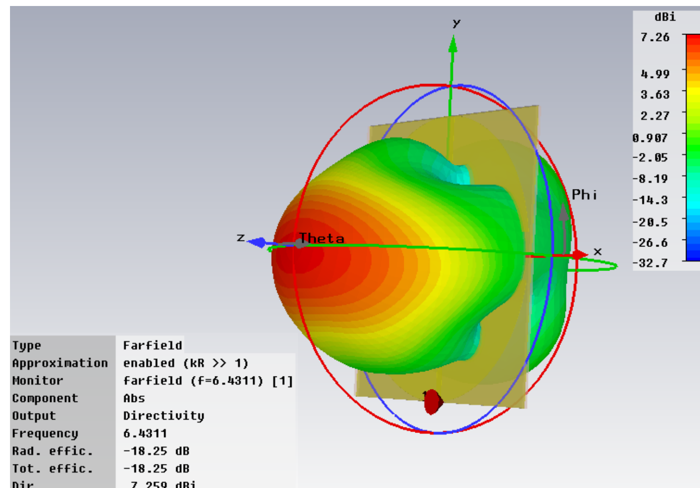

Figure 5.40: The farfield pattern of the semicircular patch circular ACMSA at 6.4311 THz

From the Figure 5.40, it can be seen that the farfield directivity pattern has the peak magnitude of 7.259 dBi, which is worse than the dual triangular patch circular ACMSA at 6.4311 THz. The back lobe associated with main lobe is significantly high. From Figure 5.41, Figure 5.42 and Figure 5.43 it can be seen that the main lobe peak magnitude for directivity is 7.3 dBi, the gain for the main lobe is -11 dB and the E-field is -3.8 db-V/m respectively. For these parameters the triangular patch circular ACMSA is better than the semicircular patch circular ACMSA.

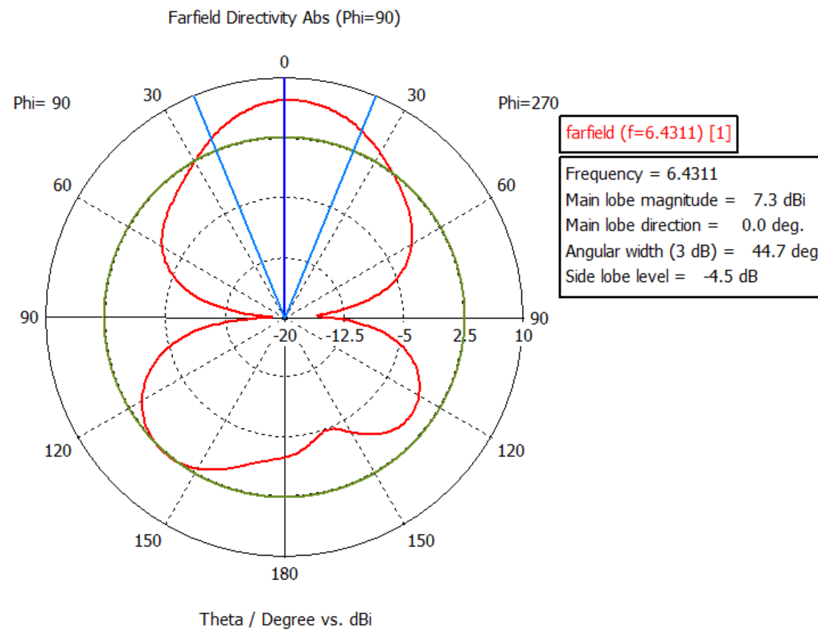

Figure 5.41: The farfield directivity for the semicircular patch circular ACMSA at 6.4311 THz

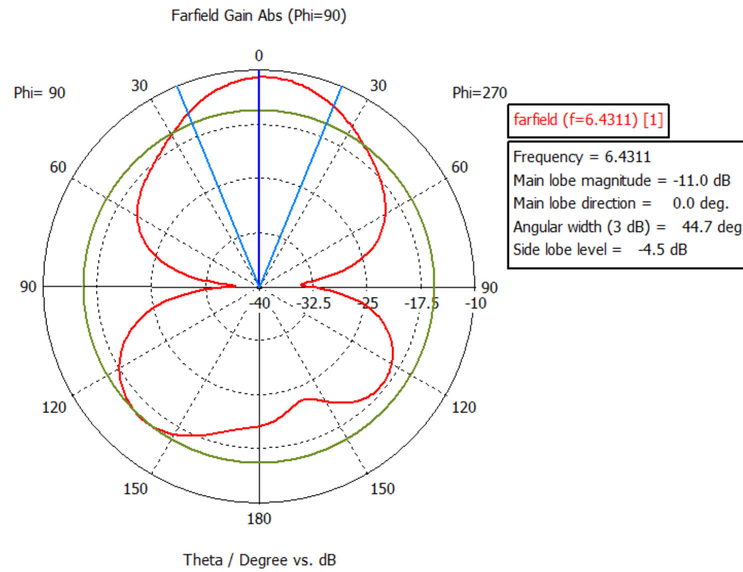

Figure 5.42: The farfield gain for the semicircular patch circular ACMSA at 6.4311 THz

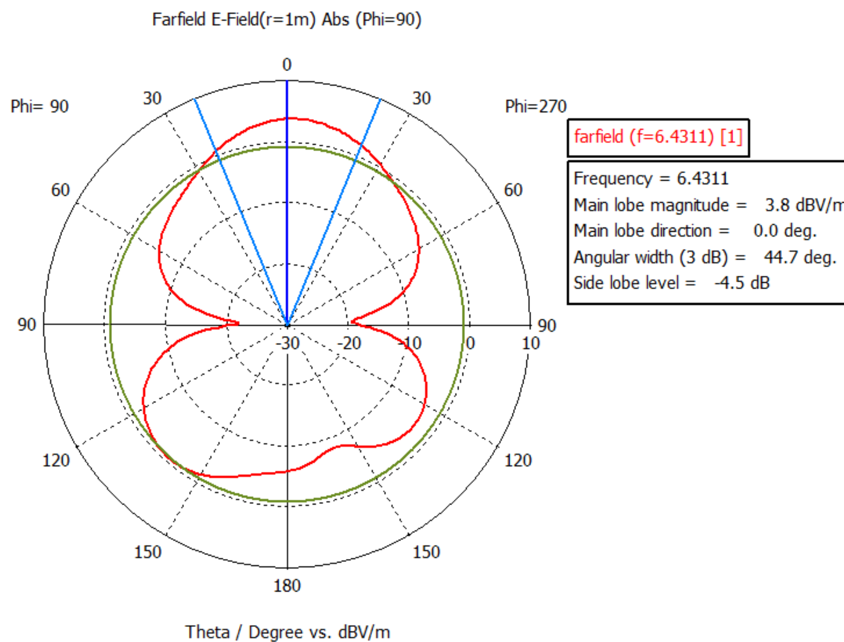

Figure 5.43: Electric field for the semicircular patch circular ACMSA at 6.4311 THz

Thus it can be inferred from the above results that the triangular patch circular ACMSA gives the best result. It has a main lobe peak magnitude directivity of 7.7 dBi. The antenna can operate at the 6.43 THz with a return loss of -35 db. The antenna can also operate in any of the multiple resonant frequencies with in 22 THz.

CHAPTER 6

6.1 Conclusion:

Antenna radiation involves a pulse source from a generator to travel through a medium (transmission line) to an antenna where radiations occur. In the analysis of THz radiation from LT-GaAs PCSS one can consider the substrate as the generator as well as the transmitting medium for the generated pulse. The generated current through the contacts lead to radiation. The pulse generated in the substrate determines the radiating frequency. Therefore it is of interest to study the pulse formation, specifically in the trap dominated semiconductor such as the LT-GaAs substrate.

Current transport in trap dominated semiconductor has been studied before. Simple put the mechanism is as follows. As the bias across the material is increased, injected charge begins to flow from the contacts. One of the carriers gets captured because of the presence of traps in the bulk and it is a single charge collection process. As the bias increases, and all trap sites gets filled and the increased field helps in the conduction of both the carriers. This is the onset of high current, after which breakdown occur due to avalanche multiplication. For best possible conduction process in trap filled PCSS, the device needs to be charged to a bias level where double injection is set to occur.

In our analysis of the PCSS structure it was determined that the bias voltage of 1100 V would produce the optimum pulse for transmission to the electrodes. The bias voltage was determined by monitoring the substrate conditions during the charging state

of the PCSS. The photo r response of the switch was in picoseconds when illuminated with 0.78 micrometer wavelength for duration of 350 femtoseconds. The peak photo current was in the order of 10^{-3} Amperes. The rise time for the electrical pulse was shown to be in the order of 10^{-12} seconds, thus generating Terahertz range frequency. We have also shown the substrate conditions are important in determining the bias at which the PCSS needs to operate.

In the analysis of the antenna, the generated pulse shape was fed to the antenna through aperture coupling. The antenna analysis showed that the triangular patch circular aperture coupled microstrip antenna has the best response. The resonant frequency was found to be at 6.43 THz and the peak return loss of approximately -35 dB. The farfield directivity was calculated to 7.72 dBi. No side lobes were associated with the main radiation lobe for this antenna. However, the back radiation was found out to be significantly high. The back radiation can be controlled by adjusting the aperture dimensions. The antenna has multiple frequency windows in which the antenna can operate. Moreover the bandwidth for this antenna is in the range of 0.5 THz or 500 GHz. The semicircular patch circular ACMSA also had the same kind of radiation pattern as triangular patch circular ACMSA, it also had the same resonant frequency as the previous one. But the directivity for the semicircular patch circular ACMSA was not as good as the triangular patch circular ACMSA. The gain for the triangular patch circular ACMSA was better than other one.

6.2 Discussion and Future work:

The SiC has a much better voltage hold off characteristics than the LT-GaAs material. As future work we can study a different material like Silicon Carbide (SiC) or Silicon Nitride (Si_xN_y) which can handle higher breakdown voltage and at the same time capable for generating electrical pulses with a lower time period. Thus it can enable us to produce higher frequency in THz regime. For the second part of the research we see that he antennas we have designed, in all the case the back radiation is significantly high. Also the bandwidth of the antenna is too low. We can overcome these drawbacks by using array of such antenna. The array of such antenna would give a better bandwidth and higher power could be radiated form the same. As mentioned in Chapter 3, the aperture size is responsible for back radiation. Thus dimensions of the aperture can be manipulated to get a better main lobe radiation pattern and minimal back lobe radiation. The gain and the directivity can be improved by adjusting the width and the length of the microstrip line. The ground plane also plays an important role in determining the back radiation. It has to be studied if it is feasible to have these kinds of antennas with partial ground. The placement of the aperture also affects the radiation pattern of the ACMSAs. Thus position of the aperture needs to be studied for achieving better gain and optimum coupling with of the patches with the ground plane. As future work we also have to have better designs of the ACMSAs to reduce the back lobes and achieving higher directivity and gain.

REFERENCES:

[1] C. A. Balanis, *Antenna Theory: Analysis and Design, 3rd Edition,* vol. Wiley-Interscience, Decmber, 2000.

[2] G. M. Loubriel*, et al.*, "Longevity of optically activated, high gain GaAs photoconductive semiconductor switches," in *Pulsed Power Conference, 1997. Digest of Technical Papers. 1997 11th IEEE International*, 1997, pp. 405-413 vol.1.

[3] F. J. Zutavern*, et al.*, "PCSS Triggered Pulsed Power Switches," in *Plasma Science, 2007. ICOPS 2007. IEEE 34th International Conference on*, 2007, pp. 249-249.

[4] H. P. Hjalmarson*, et al.*, "A collective impact ionization theory of lock-on [in pulsed power switches]," in *Pulsed Power Conference, 1999. Digest of Technical Papers. 12th IEEE International*, 1999, pp. 299-302 vol.1.

[5] F. J. Gregor Segschneider, Torsten Lo¨ffler, and Hartmut G. Roskos, "Free-carrier dynamics in low-temperature-grown GaAs at high excitation densities investigated by time-domain terahertz spectroscopy," *PHYSICAL REVIEW B,* vol. 65, March 2002.

[6] A. P. H. Ne˘mec, and P. Kuz˘el, "Carrier dynamics in low-temperature grown GaAs studied by terahertz emission spectroscopy," *Journal fo Applied Physics,* vol. 90, pp. 1303-1308, August 2001.

[7] N. E. Islam*, et al.*, "Characterization of a semi-insulating GaAs photoconductive semiconductor switch for ultrawide band high power microwave applications," *Applied Physics Letters,* vol. 73, pp. 1988-1990, 1998.

[8] E. S. N. E. Islam, C. B. Fleddermann, J. S. H. Schoenberg, and R. P. Joshi, "Analysis of high voltage operation of gallium arsenide photoconductive switches used in high power applications," *J. Appl. Lett.,* vol. 86, p. 1754, 1999.

[9] R. B. Darling, "Electrostatic and current transport properties of n+ /semi-insulating GaAs junctions,," *J. Appl. Phys.,* vol. 74, p. 4571, 1993.

[10] N. E. Yu*, et al.*, "Tunable terahertz generation at quasi-phase matching structures using femtoscond laser pulses," in *Infrared and Millimeter Waves, 2007 and the 2007 15th International Conference on Terahertz Electronics. IRMMW-THz. Joint 32nd International Conference on*, 2007, pp. 897-898.

[11] X. Ming and S. Wei, "Electrics Characteristic of Terahertz Generation with GaAs Photoconductive Dipole Antenna," in *Infrared Millimeter Waves and 14th International Conference on Teraherz Electronics, 2006. IRMMW-THz 2006. Joint 31st International Conference on*, 2006, pp. 115-115.

[12] N. E. Yu*, et al.*, "Tunable terahertz generation in periodically poled structures using femtosecond laser pulses," in *Infrared, Millimeter and*

Terahertz Waves, 2008. IRMMW-THz 2008. 33rd International Conference on, 2008, pp. 1-1.

[13] X. Jingzhou*, et al.*, "Terahertz generation from multiple transparent dielectric coated GaAs antenna," in *Infrared and Millimeter Waves, 2004 and 12th International Conference on Terahertz Electronics, 2004. Conference Digest of the 2004 Joint 29th International Conference on*, 2004, pp. 315-316.

[14] R. A. Lewis, "Terahertz generation by optical rectification in GaAs and related materials," in *Lasers & Electro Optics & The Pacific Rim Conference on Lasers and Electro-Optics, 2009. CLEO/PACIFIC RIM '09. Conference on*, 2009, pp. 1-1.

[15] Bic*, et al.*, "Terahertz generation by photoconductors made from low-temperature-grown GaAs annealed at moderate temperatures," *Electronics Letters,* vol. 47, pp. 130-132, 2011.

[16] M. Jarrahi and T. H. Lee, "High-power tunable terahertz generation based on photoconductive antenna arrays," in *Microwave Symposium Digest, 2008 IEEE MTT-S International*, 2008, pp. 391-394.

[17] T. Q. Tran and S. K. Sharma, "Performance of single layer multimode microstrip patch antenna with reconfigurable radiation patterns," in *Antennas and Propagation Society International Symposium, 2009. APSURSI '09. IEEE*, 2009, pp. 1-4.

[18] A. Kishk and L. Shafai, "The effect of various parameters of circular microstrip antennas on their radiation efficiency and the mode excitation," *Antennas and Propagation, IEEE Transactions on,* vol. 34, pp. 969-976, 1986.

[19] K. R. Jha and G. Singh, "Dual-frequency terahertz rectangular microstrip patch antenna on photonic crystal substrate," in *Applied Electromagnetics Conference (AEMC), 2009*, 2009, pp. 1-3.

[20] K. R. Jha and G. Singh, "Microstrip patch antenna on photonic crystal substrate at terahertz frequency," in *Applied Electromagnetics Conference (AEMC), 2009*, 2009, pp. 1-4.

[21] J. Cunningham*, et al.*, "On-chip terahertz systems for spectroscopy and imaging," *Electronics Letters,* vol. 46, pp. s34-s37, 2010.

[22] S. G. Kong and D. H. Wu, "TeraHertz Time-Domain Spectroscopy for Explosive Trace Detection," in *Computational Intelligence for Homeland Security and Personal Safety, Proceedings of the 2006 IEEE International Conference on*, 2006, pp. 47-50.

[23] E. Pickwell-MacPherson*, et al.*, "Application of Finite Difference Time Domain methods to Terahertz Spectroscopy Measurements of Breast Cancer," in *Microwave Symposium, 2007. IEEE/MTT-S International*, 2007, pp. 1379-1381.

[24] L. Zhang*, et al.*, "Polarization sensitive terahertz time-domain spectroscopy for birefringent materials," *Applied Physics Letters,* vol. 94, pp. 211106-211106-3, 2009.

[25] M. Naftaly and R. E. Miles, "Terahertz Time-Domain Spectroscopy for Material Characterization," *Proceedings of the IEEE,* vol. 95, pp. 1658-1665, 2007.
[26] V. N. Truchin*, et al.*, "Generation of terahertz radiation by large-aperture photoconductive antennas," in *Infrared, Millimeter and Terahertz Waves, 2008. IRMMW-THz 2008. 33rd International Conference on*, 2008, pp. 1-2.
[27] S. Inc., "Atlas Manual " vol. Silvaco Inc. , 2010.
[28] M. A. L. a. P. Mark, "Current injection is solids " *Academic Press, New York.,* 1970.
[29] F. Z. Arye Rosen, M. Buttram, "Introduction: Potential Applications in the Government and Industry," *High-Power Optically Activated Solid-State Switches,* vol. Artech House Inc., 1993.
[30] Y. C. Shen*, et al.*, *Ultrabroadband terahertz radiation from low-temperature-grown GaAs photoconductive emitters* vol. 83: AIP, 2003.
[31] R. F. Samir Rihani, Harvey Beere , Hideaki Page , Ian Gregory , Mike Evans, David Ritchie and Michael Pepper, "Effect of defect saturation on terahertz emission and detection Properties of LT-GaAs photoconductive switches," *Applied Physics Letters.,* vol. 95, 2009.
[32] J. D. K. a. R. J. Marhefka, "Antennas for all Applications, 2nd Edition," *Tata McGrawhill,* 2000.
[33] S. M. Sze, "Physics of Semiconductor Devices, 2nd edition," *Wiley, New York,* 1981.
[34] R. B. Hammond, "In:P:Fe Photoconductors as Photodetectors," *IEEE Transactions on Electronic Devices,* vol. ED-30, pp. 412-415, 1983.
[35] D. H. Auston, "Picosecond optoelectronic switching and gating in Silicon," *Applied Physics Letters,* vol. 26, pp. 101-103, 1 Februay, 1975.
[36] G. e. a. Mourou, "High Power switcing with picosecond precession," *Applied Physics Letters,* vol. 35, pp. 492-495, October, 1979.
[37] N. E. Islam*, et al.*, "Characteristics of Trap-Filled Gallium Arsenide Photoconductive Switches Used in High Gain Pulsed Power Applications.," May 2000.
[38] E. S. N. E. Islam, and C. B. Fleddermann, "Characterization of semiinsulating GaAs photoconductive semiconductor switches for ultra-wideband high power applications," *Appl. Phys. Lett. ,* vol. 73, p. 1988, 1998.

Appendix:

Code for simulation of the photoconductive emitter

```
#DevEdit version=2.8.7.R # file written Sun Apr 10 2011 15:15:31
GMT-5 (CDT)
go devedit
work.area x1=0 y1=-2 x2=60 y2=60
# devedit 2.8.7.R (Fri Apr  4 17:46:09 PDT 2008)
# libMeshBuild 1.24.5 (Fri Apr  4 17:38:34 PDT 2008)
# libSSS 2.6.3 (Fri Apr  4 17:26:34 PDT 2008)
# libSVC_Misc 1.28.3 (Thu Mar  6 15:35:06 PST 2008)
# libsflm 7.4.16 (Mon Mar 10 16:31:43 PDT 2008)
# libSDB 1.10.10 (Fri Mar 28 17:23:21 PDT 2008)
# libGeometry 1.28.4 (Thu Mar  6 15:34:57 PST 2008)
# libCardDeck 1.30.4 (Thu Mar  6 15:32:16 PST 2008)
# libDW_Set 1.28.3 (Mon Mar  3 19:39:47 PST 2008)
# libSvcFile 1.12.4 (Thu Mar  6 15:37:02 PST 2008)
# libsstl 1.8.7 (Thu Mar  6 15:37:39 PST 2008)
# libDW_Misc 1.38.5 (Thu Mar  6 15:27:39 PST 2008)
# libQSilCore 1.2.2 (Wed Aug 30 19:34:57 PDT 2006)
# liberror 1.0.6 (Wed Aug 30 19:34:52 PDT 2006)
# libDW_Version 3.2.0 (Wed Aug 30 19:34:31 PDT 2006)
region reg=1 name=GaAs_Substrate mat=GaAs color=0x7f00
pattern=0x9 \
     polygon="0,4 20,4 30,4 50,4 50,54 0,54"
#
constr.mesh region=1 default

region reg=2 name=anode mat=Aluminum elec.id=1 work.func=0
color=0xffc8c8 pattern=0x7 \
     polygon="0,0 20,0 20,4 0,4"
#
constr.mesh region=2 default

region reg=3 name=cathode mat=Aluminum elec.id=2 work.func=0
color=0xffc8c8 pattern=0x7 \
     polygon="50,4 30,4 30,0 50,0"
#
constr.mesh region=3 default


# Set Meshing Parameters
#
base.mesh height=10 width=10
#
bound.cond !apply max.slope=30 max.ratio=100 rnd.unit=0.001
line.straightening=1 align.points when=automatic
#
imp.refine min.spacing=0.02
#
```

```
constr.mesh max.angle=90 max.ratio=300 max.height=1000 \
      max.width=1000 min.height=0.0001 min.width=0.0001
#
constr.mesh type=Semiconductor default
#
constr.mesh type=Insulator default
#
constr.mesh type=Metal default
#
constr.mesh type=Other default
#
constr.mesh region=1 default
#
constr.mesh region=2 default
#
constr.mesh region=3 default

Mesh Mode=MeshBuild

# Refining the mesh for the whole structure

refine mode=both x1=0 y1=4.00 x2=49.98 y2=54.00
refine mode=both x1=0 y1=4.00 x2=49.91 y2=54.00

# Refining the mesh at the contact region

#refine mode=both x1=0 y1=4.00 x2=50.12 y2=54.00


base.mesh height=10 width=10

bound.cond !apply max.slope=30 max.ratio=100 rnd.unit=0.001
line.straightening=1 align.Points when=automatic

structure outfile=Exp_5.str

go atlas

# Doping the whole structure with P-Type

doping uniform p.type conc=2.98e+15 direction=y x.min=0 x.max=50
\
                                             y.min=4 y.max=54

# Definig Trap at the energy Level of 0.732 eV and the density of
the traps
# Defning the electron and hole capture cross section

trap donor e.level=0.730 density=3.01e+15 degen=2 \
     sign=6e-16 sigp=1.5e-18 region=1
```

```
# Defining the beam and its parameters which will hit the switch
normally and the beam is originating from 10 micrometers above
the center of the active region.

beam num=1 x.origin=25 y.origin= -10 angle= 90 wavelength=0.780 \
     min.window= -25 max.window=50



# Definig the models that would be used to simulate the device

models material=GaAs conmob fldmob srh auger numcarr=2 bbt.kl \
       print


material region = 1 name = GaAs_Substrate taun0=1e-13 taup0=4e-13


# Defining the material of the device and the impact ionization
coeffs

impact material = GaAs selb length.rel



# Defining the Mobility parameters and the power dessipation
paramteres

mobility ymaxn.watt = 0.06 xminn.watt = 30 xmaxn.watt = 50 \
         ymaxp.watt = 0.06 xminp.watt = 30 xmaxp.watt = 50


contact name = cathode resistance = 45
contact name = anode resistance = 45

method newton carriers = 2 maxtraps = 5 climit = 1e+04 cx.toler =
1e-3 \ px.toler = 1e-3 dvmax = 1e+3 autonr tol.relax=1e+05 trap
atrap = 0.8

# Declaring the log file where all the data will be stored.

log outfile=Exp_5_iv.log


# Solving the initial condition for the device without any
voltage applied to the device

solve init

save outf=Exp_5.str
tonyplot Exp_5.str
```

```
output e.field j.electron j.hole j.conduc j.total \
       ex.field ey.field \
       flowlines charge recomb j.disp impact \
       tot.doping e.mobility h.mobility \
       e.velocity h.velocity permittivity
# Applying Anode voltage to the Anode terminal of the device and
ramping up the value to 250 Volts with 1 volt as the step value.

solve vanode = 0.0 vstep = 1 vfinal = 250 name = anode

# Saving the Structure file after it is applied with Anode
Voltage

save outf = Exp_5_250v.str master

output e.field j.electron j.hole j.conduc j.total \
       ex.field ey.field \
       flowlines charge recomb j.disp impact \
       tot.doping e.mobility h.mobility \
       e.velocity h.velocity permittivity


# Applying Anode voltage to the Anode terminal of the device and
ramping up the value to 500 Volts from 250 V with 5 volt as the
step value. We use the word previous to continue the simulation
from the above statement, and append the value in the log file.

solve previous vanode = 250 vstep = 5 vfinal = 500 name = anode

# Saving the Structure file after it is applied with Anode
Voltage

save outf = Exp_5_500v.str master


output e.field j.electron j.hole j.conduc j.total \
       ex.field ey.field \
       flowlines charge recomb j.disp impact \
       tot.doping e.mobility h.mobility \
       e.velocity h.velocity permittivity


# Applying Anode voltage to the Anode terminal of the device and
ramping up the value to 1100 Volts from 500 Volts with 10 volts
as the step value.

solve previous vanode = 500 vstep = 10 vfinal = 1100 name = anode

# Saving the Structure file after it is applied with Anode
Voltage

save outf = Exp_5_1point1kv.str master
```

```
output e.field j.electron j.hole j.conduc j.total \
       ex.field ey.field \
       flowlines charge recomb j.disp impact \
       tot.doping e.mobility h.mobility \
       e.velocity h.velocity

# Applying Anode voltage to the Anode terminal of the device and
ramping up the value to 1750 Volts from 1100 Volts with 10 volts
as the step value.

solve previous vanode = 1100 vstep = 10 vfinal=1750 name = anode

# Saving the Structure file after it is applied with Anode
Voltage

save outf = Exp_5_1point75kv.str master


# Resetting the device to initial voltage and again simulating
the same to 1100 Volts which is the operational voltage for the
photoconductive emitter.

solve init


#Applying voltage to the device for the simulation with laser
beam

solve vanode=0.0 vstep=10 vfinal=1100 name= anode

output e.field j.electron j.hole j.conduc j.total \
       ex.field ey.field \
       flowlines charge recomb j.disp impact \
       tot.doping e.mobility h.mobility \
       e.velocity h.velocity permittivity


structure outfile = Exp_5_LT_GaAs.str

tonyplot Exp_5_LT_GaAs.str
tonyplot Exp_5_iv.log


log outfile = Exp_5_50MLaser.log

output e.field j.electron j.hole j.conduc j.total \
       ex.field ey.field \
       flowlines charge recomb j.disp impact \
       tot.doping e.mobility h.mobility \
       e.velocity h.velocity permittivity
```

```
# Solving for the device when hit with laser from 0 intensity to
max intensity and back to zero intensity. The pulse width of the
laser is defined by the ramp time, stop time and the step time.


# This simulation runs from 0 fs to 10 fs with a ramptime of 3 fs
and step size of 1 fs.
solve B1 = 0.0 ramptime = 3e-15 tstop = 10e-15 tstep = 1e-15
output e.field j.electron j.hole j.conduc j.total \
       ex.field ey.field \
       flowlines charge recomb j.disp impact \
       tot.doping e.mobility h.mobility \
       e.velocity h.velocity permittivity

save outfile=Exp_5_0I.str

# solving for the device when hit with a laser with intensity 50
MW/sq cm
# the duartion of the pulse is 350 fs and starts from 100 fs with
ramptime of 1 fs

solve B1 = 5e+7 ramptime = 100e-15 tstop = 350e-15 tstep = 1e-15

save outfile=Exp_5_50MI.str

# Solving for the device when hit with laser from 0 intensity to
max intensity
# This simulation runs form 350 fs adn stops at 300000 fs with a
ramptime of 1 fs

solve B1 = 0.0 ramptime = 350e-15 tstop = 300000e-15 tstep = 1e-
15

save outfile=Exp_5_0I_end.str

output e.field j.electron j.hole j.conduc j.total \
       ex.field ey.field \
       flowlines charge recomb j.disp impact \
       tot.doping e.mobility h.mobility \
       e.velocity h.velocity permittivity

# We plot the log file to analyze the results.

tonyplot  Exp_5_50MLaser.log

quit
```